

**POLYDIMETHYLSILOXANE-EMBEDDED CONDUCTIVE FABRIC  
FOR REALISATION OF ROBUST FLEXIBLE  
PASSIVE AND ACTIVE WEARABLE ANTENNAS**

by

Roy Bachtiar Van Basten Simorangkir



**MACQUARIE**  
University

Dissertation submitted in fulfilment of the requirements

for the degree of

**DOCTOR OF PHILOSOPHY**

School of Engineering  
Faculty of Science and Engineering  
Macquarie University  
Sydney, Australia

February 2018



Copyright © 2018 Roy Bachtiar Van Basten Simorangkir

All Rights Reserved





---

# Abstract

This thesis presents polydimethylsiloxane (PDMS)-embedded conductive fabric as a new approach to realise robust flexible wearable antennas. The approach combines the use of conductive fabric as the antenna radiator and ground plane, with PDMS which acts as the antenna substrate and a protective encapsulation. This allows for a simple yet effective approach to achieve robust flexible wearable antennas.

Initially, a thorough characterisation of the mechanical and electrical properties of the PDMS-embedded conductive fabric was demonstrated with four potential combinations of PDMS-conductive fabric considered in this thesis. This characterisation provides valuable insight into the mechanical robustness of the proposed approach, the constraints associated with selection of the conductive fabric for various parts of the antenna, and the effective modelling of the antenna. Upon gathering the characterisation results, several wearable antenna designs were developed as concept demonstrations. To verify the designs, their performance was then investigated experimentally, including RF performance tests both in free space and on fabricated ultra-wideband (UWB) human-muscle equivalent phantoms, and mechanical stability tests e.g. bending tests on the aforementioned phantoms and machine-washing tests.

As the first concept demonstration, four simple inset-fed rectangular patches were designed using the four combinations of PDMS-conductive fabric characterised before,

thus verifying the properties obtained from the characterisation process. Next, a new dual-band dual-mode antenna design suitable for off- and on-body communication was developed as the second demonstration. Different from previously reported works, the dual-band dual-mode operation was achieved by utilising inherently generated higher-order modes of a patch antenna, allowing for a much simpler design that only used a single patch fed by a simple probe feed.

Further, a novel planar UWB antenna design was developed to demonstrate the applicability of the PDMS-embedded conductive fabric technique for UWB and high-frequency applications. In contrast to previously reported flexible UWB antennas, the design maintains a full ground plane which provides a high isolation between the antenna and the human body when worn. The antenna time-domain analysis in both free-space and on-body environments was also conducted, demonstrating its suitability for UWB pulse transmission.

Lastly, the application of PDMS-embedded conductive-fabric technology was expanded further to cover, for the first time, the realisation of robust flexible electronically tunable wearable antennas. A frequency-reconfigurable patch antenna that can stand physical deformation and even machine-washing has been successfully developed. Its miniaturised version, incorporating a PDMS-ceramic composite substrate, was also investigated to show the versatility of the proposed PDMS-embedded conductive fabric.

In all four concept demonstrations, a good agreement between simulated and measured results is shown. Consistent performance including reconfigurability was obtained even after the antennas were exposed to harsh environments, e.g. extreme bending and machine-washing. This validates the applicability of the proposed approach for realisation of robust flexible antennas for wearable applications.

## STATEMENT OF CANDIDATE

I certify that the work in this thesis entitled **Polydimethylsiloxane-Embedded Conductive Fabric for Realisation of Robust Flexible Passive and Active Wearable Antennas** has not previously been submitted for a degree nor has it been submitted as part of the requirements for a degree to any other university or institution other than Macquarie University.

I also certify that the thesis is an original piece of research and it has been written by me. Any help and assistance that I have received in my research work and the preparation of the thesis itself have been appropriately acknowledged.

In addition, I certify that all information sources and literature used are indicated in the thesis.

.....

Roy Bachtiar Van Basten Simorangkir



*To my amazing parents, my loving sister and brother, and my dearest wife.*



---

# Acknowledgements

While my name may be alone on the front cover of this thesis, I am by no means its sole contributor. Rather, there are a number of people behind this piece of work who deserve to be both acknowledged and thanked here.

First and foremost I wish to thank my supervisor, Professor Karu P. Esselle, the director of Centre for Collaboration in Electromagnetic and Antenna Engineering (C4CELANE), for giving me the opportunity to work as a PhD student under his supervision. Thank you for the freedom and trust you gave to me to develop my own PhD research project and work on it. This journey with you, has helped me to acquire the qualities necessary to mature into an independent researcher.

Especially I would like to thank Dr. Yang Yang, whose enthusiasm for research, patience, and diligence have motivated me to complete this long journey regardless of all the obstacles. Thank you for being a good friend, a very supportive research collaborator, and often filling up the role of supervisor that I need. I am indebted to you for sparing your time to discuss the direction of this project and to assist me with a lot of measurements in the anechoic chamber.

I am also very grateful and would like to acknowledge the Commonwealth of Australia and Macquarie University for honouring me with the prestigious International Macquarie Research Excellence Scholarship (iMQRES). Without this financial support, this PhD

research would not have been possible. On top of that, I thank Macquarie University for granting a Postgraduate Research Funding (PGRF) and WiMed Research Centre Travel Grants which enabled me to present the outcomes of my research in several international conferences.

I express gratitude to Dr. Asimina Kiourti, Professor Ladislau Matekovits, Dr. Toni Bjorninen, Dr. Basit A. Zeb, and Dr. Raheel M. Hashmi for the active research collaborations we had for the last three years. Thank you for the technical supports, thoughtful suggestions, critical comments, patience, and promptness during countless revisions of research manuscripts. I am looking forward to working with you again in the future.

My acknowledgement also goes to C4CELANE members (Affan Azis Baba, Arslan Kiyani, Ali Lalbakhsh, Dr. Budhaditya Majumdar, Dr. Debabrata Karmokar, Khaled Mahbub Morshed, Maria Kovaleva, Dr. Muhammad Usman Afzal, and Rajas Prakash Khokle) and all HDR students and staffs from School of Engineering (Amit Shrestha, Anindya Nag, Abdullah-al Nahid, Chenshuo Ma, Dr. David Inglis, I Putu Edy Suardiyana Putra, Ken Yuen, Dr. Nicholas Tse, Rachel Kyung, Saad Ul Hasan, Sheley Kurniawan, Shilun Feng, Dr. Sudipta Chakraborty, Prof. Yves De Deene, Yuba Raj Kafle, Yi Du, and Yuxiang Zhu) with whom I have ever had the honour of meeting and working with. Thank you for the technical and non-technical supports, collaborations, friendship and unforgettable moments we spent over the last three years. Special thanks to Dr. Keith Imrie who has been so kind to spare his time helping me proofreading all the manuscripts that I prepared throughout this candidature including this thesis. Your invaluable feedback has helped to improve the quality of my writings.

I am also thankful to have my families in Christ, Indonesian Christian Macquarie Fellowship (Christopher and Kaitlin Anthonny, Cynthia Wongkar, Eddy Sitepu, Ellen Paulin Hutagaol, Elsa Natalina Sembiring, Fransiskus Purwanto, Harry Christianto Tjondro, Hendry Yonaga, Inggrika Remalia Kaban, Jessica Levina Halim, Kian Holik, Linda



Walandow, Liza Mihardja, Lyndle Hardstaff, Pauline Djojo, Rafael Alvin, and Raniwidia Basileia), Fellowship of Overseas Christian University Students (Ingrid Wei, Min Yee Ong, Phil Snelling, Vonnice Ho Ching Yee, and Wang Yue), Macquarie Trinity Chapel (particularly David and Sue Steele-Smith, and Tim Mildenhall), Macquarie Chapel Indonesian Church (Ari and Sophia Supala, Gita Ernestine, Irene Marius, Irene Tedjasaputra, Pudi Muliawan, Robert Supala, Steven Lee, Tirta and Lina Hadinata) and Macquarie Chapel Presbyterian Chapel Choir (especially Ravi and Rema Gnanadickam, and Bruce Goudge). Thank you for your love, supports, and most importantly prayers.

Special thanks are also for my parents (Pegang Simorangkir and Ratna Siahaan), my sister (Verawaty Simorangkir), and my brother (David Simorangkir). Thank you for all your love, supports, and prayers. For mom and dad who raised me with love, I hope I have made you proud. Also, I would like to express my huge appreciation to my wife, Elizabeth Valentin, who has been faithfully standing beside me throughout this long journey. Thank you for believing in me and my dreams, and for never letting me settle for anything less than my best. Thank you for your constant support, patience, encouragements, reminders, and prayers. Without you, I would not have sustained thus far. I love you.

Above all, I thank Jesus Christ for being my rock and my fortress. Soli Deo Gloria.



---

# List of Publications

During the candidature, the author has published several peer-reviewed scientific publications, derived from the results of this thesis work and other related research projects. Below, the references to the published contributions are listed.

## A. Main Thesis Work

### I. Journal Articles

1. R. B. V. B. Simorangkir, Y. Yang, R. M. Hashmi, T. Bjorninen, and K. P. Esselle, "Polydimethylsiloxane-embedded conductive fabric for realization of robust passive and active flexible wearable antennas," *IEEE Access (Under review, submitted on March 15, 2018)*.
2. R. B. V. B. Simorangkir, A. Kiourti, and K. P. Esselle, "UWB wearable antenna with full ground plane based on PDMS-embedded conductive fabric," *IEEE Antennas and Wireless Propagation Letters*, vol. 17, no. 3, pp. 493–496, 2018.
3. R. B. V. B. Simorangkir, Y. Yang, K. P. Esselle, and B. A. Zeb, "A method to realize robust flexible electronically tunable antennas using polymer-embedded conductive fabric," *IEEE Transactions on Antennas and Propagation*, vol. 66, no. 1, pp. 50–58, Jan. 2018.
4. R. B. V. B. Simorangkir, Y. Yang, L. Matekovits, and K. P. Esselle, "Dual-band

dual-mode textile antenna on PDMS substrate for body-centric communications,”  
*IEEE Antennas and Wireless Propagation Letters*, vol. 16, pp. 677–680, 2017.

## II. Invited/Convened Articles

1. R. B. V. B. Simorangkir, Y. Yang, and K. P. Esselle, ”Robust implementation of flexible wearable antennas with PDMS-embedded conductive fabric,” *12<sup>th</sup> European Conference on Antennas and Propagation (EuCAP)*, Apr. 2018 (*Accepted*).
2. R. B. V. B. Simorangkir, S. Feng, A. S. Md. Sayem, K. P. Esselle, and Y. Yang, ”PDMS-embedded conductive fabric: a simple solution for fabricating PDMS-based wearable antennas with robust performance,” *12<sup>th</sup> International Symposium on Medical Information and Communication Technology (ISMICT)*, Mar. 2018 (*Accepted*).
3. R. B. V. B. Simorangkir, Y. Yang, K. P. Esselle, L. Matekovits, and S. M. Abbas, ”A simple dual-band dual-mode antenna for off-/on-body centric communications,” in *Proc. 10<sup>th</sup> European Conference on Antennas and Propagation (EuCAP)*, Apr. 2016, pp. 1–3.
4. R. B. V. B. Simorangkir, S. M. Abbas, and K. P. Esselle, ”A printed UWB antenna with full ground plane for WBAN applications,” in *Proc. 2016 International Workshop on Antenna Technology (iWAT)*, Feb. 2016, pp. 127–130.
5. R. B. V. B. Simorangkir, S. M. Abbas, and K. P. Esselle, ”Robust wideband printed antennas for body-centric communications,” in *Proc. 10<sup>th</sup> International Conference on Body Area Networks (BodyNets)*, Sept. 2015, pp. 107–109.

## III. Conference Articles

1. R. B. V. B. Simorangkir, Y. Yang, K. P. Esselle, and Y. Diao, ”A varactor-tuned frequency reconfigurable fabric antenna embedded in polymer: Assessment of

suitability for wearable applications,” in *Proc. 2017 IEEE MTT-S International Microwave Symposium (IMS)*, Jun. 2017, pp. 204–207.

## **B. Other Related Projects**

### **I. Journal Articles**

1. Y. Yang, R. B. V. B. Simorangkir, X. Zhu, Q. Xue, and K. P. Esselle, ”A novel boresight and conical pattern reconfigurable antenna with the diversity of 360° polarization scanning,” *IEEE Transactions on Antennas and Propagation*, vol. 65, no. 11, pp. 5747–5756, Nov. 2017.
2. Y. Yang, X. Zhu, K. Ma, R. B. V. B. Simorangkir, N. C. Karmakar, and K. P. Esselle, ”Development of wireless transducer for real-time remote patient monitoring,” *IEEE Sensors Journal*, vol. 16, no. 12, pp. 4669–4670, June 2016.

### **II. Invited Articles**

1. R. B. V. B. Simorangkir, Y. Yang, and K. P. Esselle, ”Double-layer embroidery strategy for fabrication of textile antennas with improved efficiency,” in *Proc. 17<sup>th</sup> International Symposium on Antenna Technology and Applied Electromagnetics (ANTEM)*, Jul. 2016, pp. 1–2.

### **III. Conference Articles**

1. R. B. V. B. Simorangkir, M. Li, Y. Yang, K. Xu, K. P. Esselle, and E. Dutkiewicz, ”360-degree polarization scanning with the diversity of boresight and conical patterns switching,” *12<sup>th</sup> European Conference on Antennas and Propagation (EuCAP)*, Apr. 2018 (*Accepted*).
2. R. B. V. B. Simorangkir, Y. Yang, and K. P. Esselle, ”Performance of embroidered higher-order mode antennas with different stitching patterns,” in *Proc.*

- 11<sup>th</sup> European Conference on Antennas and Propagation (EuCAP)*, Mar. 2017, pp. 177–180.
3. A. Kiourti, J. L. Volakis, R. B. V. B. Simorangkir, S. M. Abbas, and K. P. Esselle, "UWB antennas on conductive textiles," in *Proc. 2016 IEEE International Symposium on Antennas and Propagation (APSURSI)*, Jun. 2016, pp. 1941–1942.

---

# Contents

<b>Abstract</b>	<b>v</b>
<b>Acknowledgements</b>	<b>xi</b>
<b>List of Publications</b>	<b>xv</b>
<b>Table of Contents</b>	<b>xix</b>
<b>List of Figures</b>	<b>xxiii</b>
<b>List of Tables</b>	<b>xxxi</b>
<b>List of Abbreviations</b>	<b>xxxiii</b>
<b>1 Introduction</b>	<b>1</b>
1.1 Motivation, Challenges, and State of the Art . . . . .	1
1.2 Research Framework and Objectives . . . . .	7
1.3 Organisation of the Thesis . . . . .	8
1.4 Thesis Contribution . . . . .	10
<b>2 PDMS-Embedded Conductive Fabric</b>	<b>15</b>
2.1 Introduction . . . . .	15

2.2	Materials and Method . . . . .	16
2.2.1	Conductive Fabric and Poydimethylsiloxane (PDMS) . . . . .	16
2.2.2	Embedding Conductive Fabric inside PDMS . . . . .	20
2.3	Characteristics of PDMS-Embedded Conductive Fabric . . . . .	22
2.3.1	Mechanical Characterisation . . . . .	22
2.3.2	Stability due to Structural Characteristics . . . . .	25
2.3.3	Electrical Properties . . . . .	27
2.4	PDMS-Embedded Conductive Fabric in Realisation of Flexible Antennas .	31
2.5	Measurements and Results . . . . .	35
2.5.1	Input Matching . . . . .	36
2.5.2	Far-Field Characteristics . . . . .	36
2.6	Summary . . . . .	39
<b>3</b>	<b>Simple Dual-Band Dual-Mode Wearable Antenna based on PDMS-Embedded Conductive Fabric</b>	<b>41</b>
3.1	Introduction and State of the Art . . . . .	41
3.2	Design of Dual-Band Dual-Mode Antenna . . . . .	43
3.3	Dual-Band Dual-Mode Antenna Performance . . . . .	48
3.3.1	Experimental Setup . . . . .	48
3.3.2	Input Matching . . . . .	52
3.3.3	Dual-Mode Radiation . . . . .	54
3.3.4	SAR . . . . .	60
3.4	Summary . . . . .	61
<b>4</b>	<b>UWB Wearable Antenna with Full Ground Plane based on PDMS-Embedded Conductive Fabric</b>	<b>63</b>
4.1	Introduction and State of the Art . . . . .	63



---

4.2	UWB Antenna Topology and Prototype . . . . .	66
4.3	UWB Antenna Performance . . . . .	71
4.3.1	Voltage Standing Wave Ratio (VSWR) . . . . .	71
4.3.2	Far-Field Characteristics . . . . .	74
4.3.3	SAR . . . . .	78
4.3.4	Time-Domain Performance . . . . .	80
4.4	Summary . . . . .	85
<b>5</b>	<b>Realising Robust Flexible Electronically Tunable Antennas using PDMS- Embedded Conductive Fabric</b>	<b>87</b>
5.1	Introduction and State of the Art . . . . .	87
5.2	Realisation of Flexible Electronically Tunable Antennas . . . . .	90
5.2.1	Antenna Configuration . . . . .	90
5.2.2	Fabrication . . . . .	95
5.3	Performance of Fabricated Prototype . . . . .	100
5.3.1	Input Matching . . . . .	100
5.3.2	Far-Field Characteristics . . . . .	103
5.3.3	SAR . . . . .	108
5.4	Tests of Physical Robustness . . . . .	110
5.4.1	Effect of Bending . . . . .	110
5.4.2	Effect of Washing . . . . .	112
5.5	Summary . . . . .	115
<b>6</b>	<b>Conclusions and Future Work</b>	<b>117</b>
6.1	Summary and Findings . . . . .	117
6.2	Future Work . . . . .	120

6.2.1 Flexible Metasurface-Enabled Wideband Circularly Polarised Antenna . . . . . 120

6.2.2 Flexible Semi-Transparent Antennas for Unobtrusive Wearable Applications . . . . . 122

6.2.3 Flexible Pattern Reconfigurable Antenna . . . . . 122

6.2.4 Improving the Efficiency of PDMS-Embedded Conductive Fabric based Antennas . . . . . 123

6.2.5 Feeding Connection for Testing of PDMS-Embedded Conductive-Fabric Wearable Antennas . . . . . 124

**Bibliography** . . . . . **126**

---

## List of Figures

2.1	Regular pattern of woven conductive fabric. . . . .	17
2.2	Measured electrical properties of PDMS at different volume ratio of SrTiO <sub>3</sub> loading. (a) Relative permittivity. (b) Loss tangent. . . . .	19
2.3	Schematic illustration of the fabrication process of the PDMS-embedded conductive-fabric based antennas. The numbers represent the order of the process. . . . .	21
2.4	Illustration of the samples, when: (a) the conductive fabric is embedded inside the PDMS, (b) the conductive fabric is simply attached on the PDMS surface. All dimensions are in millimetres. . . . .	23
2.5	(a) Illustration of mechanical testing scenarios which consist of two cycles of repetitive deformations. Photograph of the samples before and after tests, when: (b) the conductive fabric is embedded inside the PDMS layer; (c) the conductive fabric is simply attached on top of the PDMS layer. . .	24
2.6	SEM image view of a PDMS-embedded conductive fabric sample. . . . .	26
2.7	Photograph of the conductive fabric under a fluorescence microscope. (a) CF I. (b) CF II. (c) CF III. (d) CF IV. . . . .	26

2.8	PDMS-embedded conductive fabric transmission lines. (a) Design (All dimensions are in millimetres). (b) Photograph of prototypes fabricated with four different conductive fabrics. . . . .	27
2.9	PDMS-embedded conductive fabric T-resonators. (a) Design (All dimensions are in millimetres). (b) Photograph of prototypes fabricated with four different conductive fabrics. . . . .	28
2.10	Simulated (solid lines) and measured (dotted lines) $ S $ -parameters of PDMS-embedded conductive fabric T-resonators with (a) CF I, (b) CF II, (c) CF III, and (d) CF IV. . . . .	28
2.11	Simulated (solid lines) and measured (dotted lines) (a) transmission coefficient ( $ S_{21} $ ) and (b) input reflection coefficient ( $ S_{11} $ ) of the PDMS-embedded conductive fabric transmission lines. . . . .	29
2.12	Patch antenna design for concept demonstration. . . . .	31
2.13	Patch antennas fabricated with four different conductive fabrics. . . . .	31
2.14	The effect of encapsulation layers to the performance of the antenna: (a) $S_{11}$ . (b) Peak gain and total efficiency. Simulated results of CF I patch antenna are used as an example. . . . .	34
2.15	Illustration of bending the antenna around the plastic tube. . . . .	35
2.16	Simulated and measured $ S_{11} $ of the prototype with: (a) CF I, (b) CF II, (c) CF III, and (d) CF IV. . . . .	37
2.17	Normalised simulated and measured radiation patterns of the prototype with: (a) CF I, (b) CF II, (c) CF III, and (d) CF IV. . . . .	38
3.1	Previously reported dual-band dual-mode antenna designs. (a) [60]. (b) [61]. (c) [62]. (d) [63]. . . . .	42
3.2	Detailed geometry of the proposed dual-band dual-mode antenna. . . . .	43

3.3	Simulated input impedance for (a) various positions of the pin ( $o_p$ ) when $\alpha = 40^\circ$ and $s_l = 1.5$ mm; (b) various widths of the slots ( $s_l$ ) when $\alpha = 40^\circ$ and $o_p = 3.9$ mm; (c) various lengths of the slots ( $\alpha$ ) when $s_l = 1.5$ mm and $o_p = 3.9$ mm. . . . .	45
3.4	(a) Current and (b) electric-field distribution of the proposed antenna at 2.45 and 5.8 GHz. . . . .	47
3.5	Photographs of the fabricated dual-band dual-mode antenna. . . . .	47
3.6	On-phantom $ S_{11} $ measurement setup. (a) The antenna mounted on top of the flat UWB phantom. (b) The antenna wrapped around the wrist of the human-shaped UWB phantom in two different bending configurations. . . . .	49
3.7	Electrical properties of the UWB phantoms. . . . .	50
3.8	(a) The proposed antenna on top of the multi-layer phantom. (b) Performance ( $ S_{11} $ and peak gains) of the antenna when placed 5 mm above the multi-layer and one-layer phantoms. . . . .	51
3.9	(a) Simulated and measured $ S_{11} $ of the unbent antenna in free space and when placed on the flat phantom. (b) Measured $ S_{11} $ of the antenna when bent on the wrist of the human-shaped phantom. . . . .	53
3.10	Photographs of dual-band dual-mode antenna before and after 50 times bendings: (a) Prototype fabricated without encapsulation. (b) Prototype fabricated with encapsulation. . . . .	54
3.11	Normalised simulated and measured radiation patterns at 2.45 and 5.8 GHz. (a) In free space. (b) On the flat phantom. . . . .	55
3.12	Simulated and measured peak gains of the antenna in free space and on the flat phantom. . . . .	57
3.13	Illustration of the antenna bending setup on the cylindrical-shaped phantom in simulation. . . . .	57

3.14	Normalised simulated on-phantom radiation patterns at 2.45 and 5.8 GHz. (a) Flat vs. bent along the $x$ -axis. (b) Flat vs. bent along the $y$ -axis. . . .	58
3.15	Simulated peak gains of the antenna when placed on the flat phantom compared to when bent around the cylindrical phantom. . . . .	59
3.16	Computed 10-g averaged SAR distribution of the antenna at (a) 2.45 GHz and (b) 5.8 GHz when operating 5 mm above a human muscle phantom with an input power of 0.5 W. . . . .	60
4.1	Some examples of previously reported flexible planar UWB antennas. (a) [30]. (b) [75]. (c) [76]. (d) [77]. (e) [78]. . . . .	65
4.2	Detailed geometry of the proposed UWB antenna. . . . .	66
4.3	Simulated VSWR with varying (a) radius of big arc-shaped patch ( $r_{a1}$ ), (b) radius of small arc-shaped patch ( $r_{a4}$ ), and (c) position of T-shaped slot ( $\beta_s$ ). . . . .	68
4.4	Simulated VSWR with varying (a) length of feeding line of big arc-shaped patch ( $t_{l1}$ ), (b) length of feeding line of small arc-shaped patch ( $t_{l2}$ ) patch, (c) curvature angle of big arc-shaped patch ( $\alpha_{a1}$ ). . . . .	69
4.5	Photographs of the fabricated UWB antenna. . . . .	70
4.6	(a) Simulated and measured VSWR of the unbent antenna in free space and when placed on the flat UWB phantom. (b) Measured VSWR of the antenna when bent on the head and wrist of the human-shaped UWB phantom. . . . .	72
4.7	Photograph of the fabric patch layer obtained through laser cutting. . . . .	73
4.8	On-phantom VSWR measurement setup. (a) The antenna wrapped on the head of the human-shaped phantom. (b) The antenna wrapped around the wrist of the human-shaped phantom. . . . .	73
4.9	Normalised radiation patterns of the antenna at 5, 7, and 9 GHz. (a) In free space. (b) On the flat phantom. . . . .	75

4.10	Simulated and measured peak gains and total efficiencies of the antenna when in free space and on the flat phantom . . . . .	76
4.11	Normalised simulated radiation patterns of the antenna at 5, 7, and 9 GHz. (a) On the flat phantom. (b) Bent around the cylindrical phantom. . . . .	77
4.12	Simulated peak gains and total efficiencies of the antenna when placed on the flat phantom and bent around the cylindrical phantom . . . . .	78
4.13	Simulated 10-g averaged SAR distribution of the antenna at 5, 7, and 9 GHz. (a) On the flat phantom. (b) On the cylindrical phantom. The input power of the antenna is 0.5 W and the distance between the antenna and the phantom is maintained 5 mm. . . . .	79
4.14	Simulation setup for time-domain analysis. (a) Free-space case. (b) On-phantom case. . . . .	80
4.15	Different excitation pulses used in the system fidelity analysis. (a) Time domain waveforms. (b) Power spectral density. . . . .	82
4.16	Simulated Tx and Rx pulses. (a) In free space. (b) With the flat phantom. . . . .	83
4.17	System fidelity patterns of the proposed UWB antenna in free space (solid lines) and on the flat phantom (dashed lines), at the (a) horizontal ( $y$ - $z$ ) plane and (b) vertical ( $x$ - $z$ ) plane. . . . .	84
5.1	Some examples of previously reported flexible electronically tunable antennas. (a) [8, 97]. (b) [42]. (c) [95]. (d) [96]. . . . .	89
5.2	Configuration of proposed frequency-reconfigurable antennas. (a) RFPA 1. (b) RFPA 2. . . . .	91
5.3	Current distribution of the antenna at its resonance frequency corresponding to the given reverse-bias voltages. (a) RFPA 1. (b) RFPA 2. . . . .	94
5.4	The effects of the number of varactors on the resonance frequency and total efficiency of the antenna. (a) RFPA 1. (b) RFPA 2. . . . .	96

5.5	Schematic illustration of the fabrication process of the PDMS-embedded conductive-fabric based reconfigurable antennas. The numbers represent the order of the process. . . . .	98
5.6	Fabricated reconfigurable antenna prototypes. (a) RFPA 1. (b) RFPA 2. . . . .	99
5.7	Experimental setup for $ S_{11} $ measurements of the antenna on the flat phantom. (a) RFPA 1. (b) RFPA 2. . . . .	99
5.8	Simulated and measured $ S_{11} $ of RFPA 1 with various reverse-bias voltages. (a) In free space. (b) On the flat phantom. . . . .	101
5.9	Simulated and measured $ S_{11} $ of RFPA 2 with various reverse-bias voltages. (a) In free space. (b) On the flat phantom. . . . .	102
5.10	Normalised radiation patterns for RFPA 1 at states I and VI. (a) In free space. (b) On the flat phantom. . . . .	105
5.11	Normalised radiation patterns RFPA 2 at states I and VI. (a) In free space. (b) On the flat phantom. . . . .	106
5.12	SAR measurement setup with APREL ALSAS-10U system. . . . .	109
5.13	Simulated 10-g averaged SAR distribution of the antenna at 2.45 GHz when operating 5 mm above the human phantom with an input power of 100 mW. (a) RFPA 1. (b) RFPA 2. . . . .	109
5.14	The antenna wrapped around the wrist of the UWB phantom in two different bending configurations. . . . .	110
5.15	Measured $ S_{11} $ of the antenna with various reverse-bias voltages under bending on the phantom's wrist. (a) RFPA 1. (b) RFPA 2. . . . .	111
5.16	The antenna inside the washing machine. . . . .	113
5.17	Measured $ S_{11} $ of the antennas with different reverse-bias voltages before and after machine washing. (a) RFPA 1. (b) RFPA 2. . . . .	114



---

6.1	Illustration of metasurface-enabled wideband circularly polarised antenna on PDMS-embedded conductive fabric . . . . .	121
6.2	Veilshield from Less EMF Inc.: woven-mesh polyester fibre coated with nickel/zinc blackened copper (thickness = 0.057 mm, sheet resistance = 0.1 $\Omega/\text{sq}$ ). . . . .	123
6.3	Feeding point on PDMS-embedded conductive-fabric patch antenna. . . .	124



---

## List of Tables

1.1	Examples of Non-Conductive Fabric Used for Wearable Antenna Realisation	3
1.2	Examples of Conductive Fabric Used for Wearable Antenna Realisation . .	4
1.3	Examples of Conductive Thread Used for Wearable Antenna Realisation . .	5
1.4	Examples of Flexible Polymers Used for Wearable Antenna Realisation . .	6
2.1	Conductive Fabrics Investigated in this Work . . . . .	17
2.2	Adjusted Effective Conductivity Used to Model the Conductive Fabrics Embedded in PDMS . . . . .	30
2.3	Detailed Dimensions of Patch Antennas Designed with Four Different Con- ductive Fabrics . . . . .	32
2.4	Summary of the Antenna Prototypes' Peak Gains and Total Efficiencies in Free Space . . . . .	39
3.1	Dimensions of the Proposed Dual-Band Dual-Mode Antenna . . . . .	46
4.1	Dimensions of the Proposed UWB Antenna . . . . .	67
4.2	System Fidelity Factor of the Antenna at $\phi = \theta = 0^\circ$ with Three Different Pulses . . . . .	84
5.1	Detailed Dimensions of RFPA 1 and 2 . . . . .	93

5.2	Reverse-Bias Voltage and Corresponding Varactor Junction Capacitance	. 93
5.3	Summary of the Peak Gains and Total Efficiencies of the Fabricated Pro- totypes over the Entire Tuning Range (0 to 20 V Reverse-Bias Voltages)	. 107

---

# List of Abbreviations

AusAMF	Australian Antenna Measurement Facility
CST	Computer Simulation Technology
DC	Direct Current
FCC	Federal Communications Commission
ISM	Industrial, Scientific, and Medical
LCP	Liquid Crystal Polymer
PCB	Printed Circuit Board
PDMS	Polydimethylsiloxane
PEN	Polyethylene Naphthalate
PEP	Polyethylene Powder
PET	Polyethylene Terephthalate
PTFE	Polytetrafluoroethylene
RF	Radio Frequency
Rx	Receiver
SAR	Specific Absorption Rate
SEM	Scanning Electron Microscope
SFF	System Fidelity Factor

SMA	SubMiniature Version A
TCO	Transparent Conducting Oxide
TM	Transverse Magnetic
Tx	Transmitter
UWB	Ultra-wideband
VSWR	Voltage Standing Wave Ratio
WBAN	Wireless Body Area Network

## 1.1 Motivation, Challenges, and State of the Art

With the growing needs in ubiquitous communications, significant interest in the development and application of Wireless Body Area Networks (WBANs) has emerged. WBAN refers to a network of wireless communication devices and sensor systems which is located in, on, or around the human body to collect and analyse data from various activities. WBAN applications span a wide area which can be categorised into whether they are used in a medical field or a non-medical field. WBAN non-medical applications include cognitive and emotional recognition for driving assistance or social interactions, motion and gestures detection for fitness and interactive gaming, medical assistance in disaster events, such as earthquakes, building fires, and terrorist attacks, and secure authentication through physiological and behavioural biometrics [1,2]. On the other hand, WBAN utilisation in the medical field comprises healthcare solutions for ageing and diseased population, examples of which include the early detection, prevention and monitoring of diseases, assistance to the elderly at home, rehabilitation after surgery, and ambient assisted living applications [1–3].

With this wide range of applicability, it is inevitable to witness a growth in the wireless wearable devices market, which has consequently also brought a huge demand for flexible

and reversibly deformable wearable antennas as the key component in the Radio Frequency (RF) front end of a wireless system. Particularly, a human body is such a unique operating environment for an antenna. It consists of different layers of high permittivity and lossy tissue, which means that the characteristics of the antenna such as impedance bandwidth, gain, efficiency, and radiation pattern will be significantly affected by the vicinity of the human body unless properly designed [4]. Furthermore, considering the necessity of comfort for prolonged use, conventional antennas fabricated using printed circuit board (PCB) technology are not suitable for this application. This is due to their poor flexibility, thus making them unable to cope with the dynamic nature of the human body and to withstand mechanical deformations in the human body environment, such as bending, twisting, and stretching.

To address these challenges, in addition to the development of new antenna designs suitable for wearable applications, in recent years significant efforts have been focused on the realisation of flexible wearable antennas using unconventional materials, such as textiles. Besides being flexible and commercially available, textiles make possible the integration of the antenna into cloth, thus allowing for the realisation of less-obtrusive wearable electronics. In addition to that, textiles are very porous materials, with air filling the spaces in between the fibres, thus allowing textiles to have a very low relative permittivity ( $<2$ ) and quite an acceptable loss. All of these advantages currently place textiles as the most studied and popular option of the unconventional materials for realisation of wearable antennas.

There are a few types of textiles used for antenna realisation: ordinary fabrics, conductive fabrics, and conductive threads. The ordinary fabrics are usually used as the dielectric substrate of the antenna, while the conductive ones are normally utilised for the conductive parts of the antenna, i.e. radiator and ground plane. For the latter, its electrical behaviour is normally quantified by the sheet resistance or effective conductivity,



which varies depending on the properties of the constituent fibres (the metal coatings/fillings, the diameter, the density and direction when composing the fabric) [5,6]. Table 1.1, 1.2 and 1.3 summarise some textile materials that have been utilised to develop wearable antennas, along with their electrical properties.

**Table 1.1:** Examples of Non-Conductive Fabric Used for Wearable Antenna Realisation

Ref	Fabric	$\varepsilon$	$\tan\delta$	Freq. (MHz)
[6]	Quartzel	1.95	0.0004	2600
[6]	Cordura-Lycra	1.5	0.0093	2600
[7]	Cotton-Polyester	1.6	0.02	2450
[8]	Cotton	1.92	0.023	400
[9]	Felt	1.2	0.02	2450
[10]	Cordura	1.9	0.0098	900 & 1800

Note:  $\varepsilon$  = relative permittivity,  $\tan\delta$  = loss tangent, Freq. = application frequency

**Table 1.2:** Examples of Conductive Fabric Used for Wearable Antenna Realisation

Ref	Fabric	Thickness (mm)	$R_s$ ( $\Omega/\text{sq}$ )	Freq. (MHz)
[11]	Zelt (copper-tin coated nylon)	0.06	0.01	2450 & 5800
[12]	Shieldt super (nickel-copper coated polyester ripstop)	0.17	<0.5	2400
[13]	Copper-coated polyester taffeta	0.08	0.05	900
[13]	Silver-coated ripstop	0.05	0.25	900
[13]	Silver-coated elastic nylon	0.4	1	900
[13]	ArgenMesh (silver mesh)	0.3	1	900
[14]	NCS95R-CR (nickel-copper-silver coated nylon ripstop)	0.13	0.01	4500
[15]	Flectron (copper-coated nylon ripstop)	0.127	0.07	2450

Note:  $R_s$  = sheet resistance, Freq. = application frequency

**Table 1.3:** Examples of Conductive Thread Used for Wearable Antenna Realisation

Ref	Thread	Composition	Diam. (mm)	R ( $\Omega/\text{m}$ )	Freq. (MHz)
[16]	Shieldex	34 braided silver-coated polyamide fibre	NA	500	900
[17]	Amberstrand-332	332 braided silver-coated Zylon fibre	0.34	0.75	900, 1900 & 2450
[18]	Amberstrand-664	664 braided silver-coated Zylon fibre	0.53	0.53	up to 4000
[18]	Liberator-20	20 braided silver-copper coated Vectran fibre	0.22	0.22	up to 4000
[18]	Liberator-40	40 braided silver-copper coated Vectran fibre	0.27	0.27	up to 4000
[19]	Elektrisola	7 braided silver-coated copper fibre	0.12	1.9	1000–5000
[20]	Aracon	178 braided silver-coated Kevlar fibre	0.76	3.3	up to 5000

Note: Diam. = total diameter of thread, R = resistance, Freq. = application frequency

The material compositions and mechanical properties of textiles, nevertheless, make them prone to extreme temperature, wetness, or even severe repetitive deformation. This has, therefore, challenged the utilisation of textiles for wearable antenna realisation because wearable antennas are inevitably exposed to such harsh operating environments. Another material which has been receiving significant interest in the development of flexible wearable antennas is flexible polymers. Some examples that have been used in the development of flexible wearable antennas are shown in Table 1.4. In general, they have low permittivity with acceptable loss, making them appealing for high-frequency designs. Further, unlike textiles, these polymers possess low water absorption together with high flexibility and stretchability, which make them stable across a wide range of environments. Polymers are normally utilised as the substrate or non-conductive parts of the antenna whereas, acting as the conductive parts, other classes of materials are used, such as perforated copper sheet [21], conductive tape [22], conductive polymers [23], copper paste [24], conductive textiles [25–27], embroidered layers [28, 29], liquid-metal alloy [30–33], and nanomaterials (e.g. carbon nanotube [34], graphene [35], and silver nanowire [36–38]).

**Table 1.4:** Examples of Flexible Polymers Used for Wearable Antenna Realisation

Ref	Polymer	$\varepsilon$	$\tan\delta$	Freq. (GHz)
[21, 28]	Polydimethylsiloxane (PDMS)	2.7	0.001–0.05	0.1–7
[39]	Liquid Crystal Polymer (LCP)	3.16	0.003–0.005	30–97
[40]	Polyethylene naphthalate (PEN)	3.2	0.005	7.5
[41]	Kapton polyimide	3.4	0.002	0.87–3.6
[42]	Polyethylene terephthalate (PET)	3	0.008	2.4 & 3.6

Note:  $\varepsilon$  = relative permittivity,  $\tan\delta$  = loss tangent, Freq. = application frequency

With such benefits, the inherently weak metal-polymer adhesion [25, 43], however, challenges the development of flexible antennas with polymers, as the integration of the antenna conductive parts is problematic. This poor adhesion can lead to frequent detachment of the metal layers under deformation and stress. In the last decade, some solutions to this issue have been proposed, which include embedding carbon nanotube sheets [34], embedding perforated copper sheet [21], embedding silver nanowires (AgNWs) [37, 38], injecting liquid metal [30–33], and oxygen plasma treatment on the polymer surface prior to metal deposition [23, 36, 43]. Generally, the primary issue with these approaches is the complexity of the fabrication process, whereas the properties of materials, such as the low conductivity of the carbon nanotube [44], the possibility of liquid metal leakage [37], the less flexibility and durability of copper sheet [32], and the high material cost of silver [45] are some of the several secondary challenges. On the other hand, the method of embedding embroidered conductive threads has also been proposed in [46, 47]. However, the application has only been demonstrated for wire type antenna where the surface contact between the conductive part and the PDMS is very minimum.

## 1.2 Research Framework and Objectives

Given the aforementioned challenges, it is, therefore, clear that further research on the development of new techniques or material combinations for wearable antenna realisation is still needed. This thesis focuses on developing a novel, simple yet effective approach to realise robust flexible wearable antennas, namely PDMS-embedded conductive fabric. This method combines the mechanical and electrical advantages of textile and polymer to solve the problems faced when each material is used separately. Specifically, woven conductive fabric and PDMS polymer are used in this work for their unique characteristics that will be elaborated in the next chapter. The conductive fabric is used as the conductive

parts of the antenna, e.g. radiator and ground plane, whereas the PDMS is utilised as the non-conductive parts of the antenna, e.g. substrate and encapsulation layers. Unlike previous studies in [25–27] that utilise similar combinations of materials by merely attaching the conductive fabric to the surface of the PDMS, the conductive fabric is embedded inside the PDMS. This approach solves the challenge of inherently weak metal-polymer adhesion in a relatively simple way, leading to a significantly stronger integration between the two. Further, the full encapsulation by PDMS protects all the antenna parts from harsh environments, providing the physical robustness needed by wearable applications.

Another important objective of this thesis is to develop various novel wearable antennas, from passive to active type, based on the proposed PDMS-embedded conductive fabric. Each proposed design is accompanied by thorough investigations on the performance of the antennas in both free space and real operating environments. The latter includes operation in close proximity to the human body and in harsh conditions such as repetitive deformations and machine washing. The aims are not only to demonstrate the applicability of the proposed fabrication method for realisation of robust flexible wearable antennas but also to validate the suitability of the antenna designs for wearable applications.

### 1.3 Organisation of the Thesis

This thesis consists of six chapters starting with this introductory chapter (Chapter 1), which covers the background, framework, and objectives of this work. The remainder of this thesis is organised as follows.

In Chapter 2, the details on the proposed realisation approach, PDMS-embedded conductive fabric, are given. It begins with a description of the materials and equipment required during the preparation and the fabrication of the antenna. A bottom-up multi-

layer fabrication approach is introduced for an easy integration of the antenna components and accurate fabrication. Further, the chapter also contains the characterisation of the mechanical and electrical properties of the PDMS-embedded conductive fabric, followed by a first concept demonstration of the proposed approach using four simple inset-fed rectangular patch antennas. The numerical results are presented in comparison with the measured results.

In Chapter 3, a novel dual-band dual-mode antenna realised using the PDMS-embedded conductive fabric technology is presented as the next concept demonstration. Firstly, a state-of-the-art dual-band dual-mode antenna is briefly described to highlight the novelty of the proposed design. Then, the new technique of achieving dual-band dual-mode operation is discussed clearly. In the rest of the chapter, the numerical and experimental investigations of the antenna performance, both in free-space and on-body environments, are presented. The experimental investigations include the repetitive severe bending tests of the fabricated prototype using PDMS-embedded conductive fabric technology in comparison with its counterpart where the conductive fabric is simply adhered on the surface of the PDMS substrate. This chapter also contains the fabrication and characterisation of two UWB human-muscle equivalent phantoms used for the on-body performance evaluation of all the wearable antennas developed in this thesis.

In Chapter 4, a new flexible planar UWB wearable antenna is proposed. The design was fabricated via PDMS-embedded conductive-fabric technology to demonstrate the applicability of this fabrication technique for UWB and high-frequency applications. The chapter starts with a state-of-the-art flexible planar UWB antenna, highlighting their common characteristic of having high back radiation which is undesirable for wearable applications. Following that, the proposed design which has a full ground plane on the back of the radiator is presented in detail as the solution to the aforementioned problem. The approach utilised to achieve an ultra-wide bandwidth out of an inherently narrow-band

microstrip type antenna is also discussed. The rest of the chapter studies the antenna performance numerically and experimentally, in both free-space and on-body environments. The experimental evaluations include bending tests on the fabricated UWB phantom. This chapter also contains a numerical evaluation of the antenna System Fidelity Factor (SFF) to justify its capability for UWB-pulse transmission.

In Chapter 5, a method to realise robust flexible electronically tunable antennas using PDMS-embedded conductive fabric is proposed. This chapter expands further the application of the PDMS-embedded conductive fabric in wearable antennas realisations. Before presenting the design of a new frequency-reconfigurable antenna which was developed to demonstrate the proposed method, this chapter starts with a brief state-of-the-art flexible electronically tunable antenna. An approach to miniaturise a PDMS-embedded conductive-fabric antenna through inclusion of a PDMS-ceramic composite substrate is also presented in this chapter. The method was applied to the proposed frequency-reconfigurable antenna as an application example. The rest of the chapter contains the numerical and experimental investigations, both in free-space and on-body environments, on the performance of the frequency-reconfigurable antenna compared to its miniaturised version. The experimental investigations include the bending tests, machine-washing tests, and Specific Absorption Ratio (SAR) measurements.

Finally, in Chapter 6 a summary of the key research findings of this thesis and concluding remarks are drawn, along with some guidelines for future work.

## 1.4 Thesis Contribution

This thesis contributes to the area of wearable antenna design and fabrication in several ways. The first contribution is the development of a new approach to realise robust flexible wearable antennas utilising conductive fabric and PDMS. This approach is relatively simple yet effective to achieve a strong integration of the conductive fabric and PDMS



that leads to its withstanding very harsh operating conditions. The details of the proposed approach are presented in Chapter 2, of which the results have been reported in some conference papers and also have been submitted for possible publication in a journal as listed below:

- R. B. V. B. Simorangkir, Y. Yang, and K. P. Esselle, "Robust implementation of flexible wearable antennas with PDMS-embedded conductive fabric," *12<sup>th</sup> European Conference on Antennas and Propagation (EuCAP)*, Apr. 2018 (*Accepted*).
- R. B. V. B. Simorangkir, S. Feng, A. S. Md. Sayem, K. P. Esselle, and Y. Yang, "PDMS-embedded conductive fabric: A simple solution for fabricating PDMS-based wearable antennas with robust performance," *12<sup>th</sup> Int. Symposium on Medical Information and Communication Technology (ISMICT)*, Mar. 2018 (*Accepted*).
- R. B. V. B. Simorangkir, Y. Yang, R. M. Hashmi, T. Bjorninen, and K. P. Esselle, "Polydimethylsiloxane-embedded conductive fabric for realization of robust passive and active flexible wearable antennas," *IEEE Access* (*Under review, submitted on March 15, 2018*).

The second contribution is the new design of a dual-band dual-mode wearable antenna. As compared to previously reported dual-band dual-mode antennas, the design is much simpler, using only a single circular patch fed by a simple probe feed. Instead of using two different radiators, the dual-band dual-mode operation is achieved by utilising the inherently generated higher-order transverse magnetic (TM) modes of the patch, which were tuned with reactive loading techniques, namely a shorting pin and two arc-shaped slots. Beside simplicity, the design has the advantage of having a full ground plane, providing a high degree of isolation between antenna and body. Furthermore, developed with PDMS-embedded conductive-fabric technology, the antenna fulfils the flexibility requirement of wearable applications, in contrast to previous designs that were made of conventional rigid

materials. The details of the antenna design and performance are presented in Chapter 3. Some of the research outcomes have been published in the conference papers and journal article listed below:

- R. B. V. B. Simorangkir, Y. Yang, and K. P. Esselle, "Robust implementation of flexible wearable antennas with PDMS-embedded conductive fabric," *12<sup>th</sup> European Conference on Antennas and Propagation (EuCAP)*, Apr. 2018 (*Accepted*).
- R. B. V. B. Simorangkir, Y. Yang, L. Matekovits, and K. P. Esselle, "Dual-band dual-mode textile antenna on PDMS substrate for body-centric communications," *IEEE Antennas and Wireless Propagation Letters*, vol. 16, pp. 677–680, 2017.
- R. B. V. B. Simorangkir, Y. Yang, K. P. Esselle, L. Matekovits, and S. M. Abbas, "A simple dual-band dual-mode antenna for off-/on-body centric communications," in *Proc. 10<sup>th</sup> European Conference on Antennas and Propagation (EuCAP)*, Apr. 2016, pp. 1–3.

The third contribution is the development of a novel planar flexible UWB antenna design for wearable applications. The design was developed on a simple microstrip technology, maintaining a full ground plane on the other side of the radiator patches. Consequently, the antenna is highly isolated from the human-body loading effect and provides less impact to the body tissue. This approach is significantly unique compared to previously reported flexible planar UWB antennas, which generally have partial/modified ground planes or coplanar waveguide topologies for an easy bandwidth enhancement. The antenna is also suitable for UWB pulse transmission, verified through a system fidelity factor analysis. Chapter 4 discuss the details of the antenna design and performance, of which some outcomes have been reported in the conference papers and journal article below:

- R. B. V. B. Simorangkir, A. Kiourti, and K. P. Esselle, "UWB wearable antenna

with full ground plane based on PDMS-embedded conductive fabric,” *IEEE Antennas and Wireless Propagation Letters*, vol. 17, no. 3, pp. 493–496, 2018.

- R. B. V. B. Simorangkir, S. M. Abbas, and K. P. Esselle, ”A printed UWB antenna with full ground plane for WBAN applications,” in *Proc. 2016 International Workshop on Antenna Technology (iWAT)*, Feb. 2016, pp. 127–130.
- R. B. V. B. Simorangkir, S. M. Abbas, and K. P. Esselle, ”Robust wideband printed antennas for body-centric communications,” in *Proc. 10<sup>th</sup> International Conference on Body Area Networks (BodyNets)*, Sept. 2015, pp. 107–109.

The fourth contribution is the development of a novel approach to realise a robust flexible electronically tunable antenna for wearable applications; by extending the PDMS-embedded conductive-fabric method presented in Chapter 2, electronic tuning components were added to the body of the antenna before applying the PDMS encapsulation layers. A novel frequency-reconfigurable patch antenna has been successfully developed with this method and tested, demonstrating a consistent reconfigurability even after severe deformations and machine washing. This approach, therefore, solves the challenge of having a robust integration of lumped components to flexible materials, faced by previously reported flexible reconfigurable antennas. The details of this approach are discussed in Chapter 5. Part of the outcomes of this chapter have been published in the following conference papers and journal article:

- R. B. V. B. Simorangkir, Y. Yang, and K. P. Esselle, ”Robust implementation of flexible wearable antennas with PDMS-embedded conductive fabric,” *12<sup>th</sup> European Conference on Antennas and Propagation (EuCAP)*, Apr. 2018 (*Accepted*).
- R. B. V. B. Simorangkir, Y. Yang, K. P. Esselle, and B. A. Zeb, ”A method to realize robust flexible electronically tunable antennas using polymer-embedded conductive fabric,” *IEEE Transactions on Antennas and Propagation*, vol. 66, no. 1,

pp. 50–58, Jan. 2018.

- R. B. V. B. Simorangkir, Y. Yang, K. P. Esselle, and Y. Diao, "A varactor-tuned frequency reconfigurable fabric antenna embedded in polymer: assessment of suitability for wearable applications," in *Proc. 2017 IEEE MTT-S Int. Microwave Symposium (IMS)*, Jun. 2017, pp. 204–207.

The fifth contribution of this thesis is the miniaturisation technique of a PDMS-embedded conductive-fabric-based antenna through inclusion of a PDMS-ceramic composite substrate. The method was applied to the frequency-reconfigurable antenna developed in Chapter 5, leading to over 50% miniaturisation of the total size of the antenna. The details of this approach are also discussed in Chapter 5. The related outcomes have also been included in the submitted journal manuscript below:

- R. B. V. B. Simorangkir, Y. Yang, R. M. Hashmi, T. Bjorninen, and K. P. Esselle, "Polydimethylsiloxane-embedded conductive fabric for realization of robust passive and active flexible wearable antennas," *IEEE Access* (*Under review, submitted on March 15, 2018*).

# CHAPTER 2 PDMS-Embedded Conductive Fabric

---

## 2.1 Introduction

In this chapter, the details of the proposed PDMS-embedded conductive-fabric technology are discussed. It begins with Section 2.2, where the description of materials, preparation steps, and systematic process of conductive fabric inclusion inside PDMS are given. Then in Section 2.3 a thorough characterisation of the mechanical and electrical properties of PDMS-embedded conductive fabric is presented. The purposes are to provide valuable insights into the mechanical robustness of this approach, the constraints associated with selection of the conductive fabric for various parts of the antenna, and the effective modelling of the antenna. Following that, the first application example used to demonstrate the applicability of the proposed method for flexible antenna realisation is given in Section 2.4. The performance of the fabricated antenna is presented in Section 2.5 and a summary of the chapter is provided in Section 2.6.

## 2.2 Materials and Method

### 2.2.1 Conductive Fabric and Poydimethylsiloxane (PDMS)

For the realisation of the antenna substrate and the complete encapsulation of the antenna, PDMS was chosen over other polymer materials due to its unique characteristics described as follows. First and foremost, PDMS has a remarkably low Young's modulus which indicates extremely high flexibility and stretchability compared to any other polymers [?, 48]. It also has an acceptable loss in the microwave region with an easy-to-tune relative permittivity value [49], making it attractive for modern RF applications. Unlike most polymers, the preparation of PDMS can be done in a room temperature through a simple and a low-cost process [34]. In addition to that, the molecular structure of PDMS renders it unique properties of water-resistance, heat-resistance (up to 400°C), ultraviolet-rays resistance, and chemical stability, which make PDMS resilient to extreme environments [50, 51].

On the other hand, for the antenna conductive parts, i.e. the ground plane and patch, woven conductive fabrics are considered for their higher and isotropic effective conductivity, compared to those of knitted conductive fabrics [6]. Fig. 2.1 illustrates the regular patterns of the woven conductive fabric used. Entirely plated multifilament threads intertwine with each other in a one-to-one ratio between the vertical and horizontal directions, and the distance between adjacent groups of threads is very small, less than 0.04 mm, thus allowing a good resemblance to a solid metallic plate [52]. There are four different conductive fabrics considered in this work, named CF I, II, III, and IV, the details of which are listed in Table 2.1. The information about the fabrics was gathered from the datasheets provided by the manufacturers, Marktek Inc. and Less EMF Inc. The major differences between the fabrics are their thicknesses, the composition of the

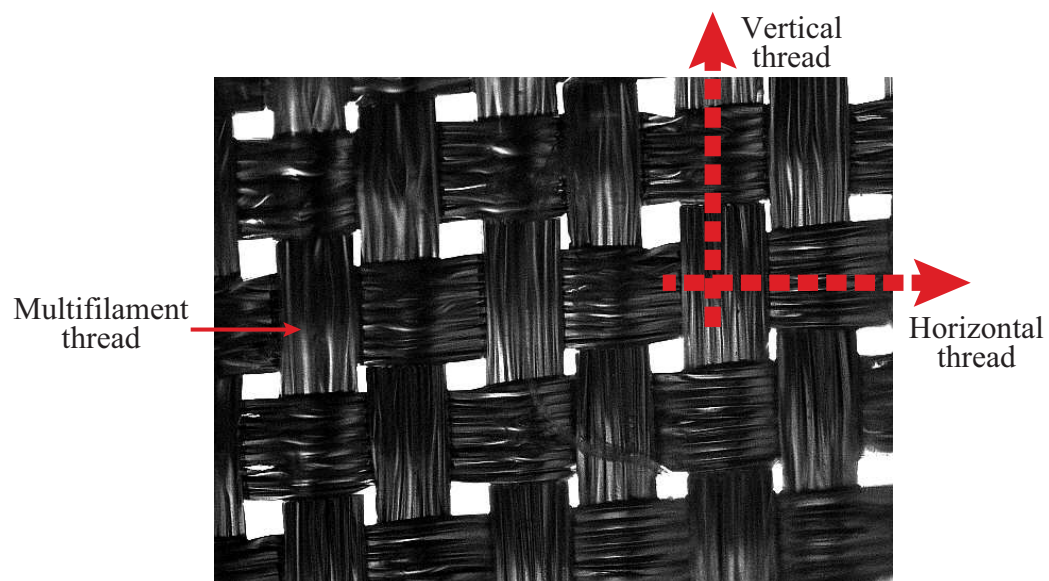


**Figure 2.1:** Regular pattern of woven conductive fabric.

**Table 2.1:** Conductive Fabrics Investigated in this Work

Type	Composition	Thickness (mm)	$\sigma$ (S/m)
CF I	nickel-copper-silver coated nylon ripstop	0.13	$7.7 \times 10^5$
CF II	copper coated polyester taffeta	0.08	$2.5 \times 10^5$
CF III	nickel-copper coated ripstop	0.08	$4.2 \times 10^5$
CF IV	silver coated ripstop	0.05	$8 \times 10^4$

Note  $\sigma$  = effective conductivity

metal coating on the threads, and the threads density, which lead to different effective conductivities, affecting the performance of the fabricated antenna.

A Dow Corning Sylgard 184 silicone elastomer kit was employed for preparation of PDMS layers. Firstly, the base and the curing agent of the kit were mixed at room temperature in a ratio of 10 to 1, followed by degassing the mixed solution in a vacuum desiccator to remove bubbles possibly formed during the mixing. Afterwards, the bubble-free solution was tape-casted or poured into the target mould, to ensure the desired thickness of the PDMS layers. If necessary, the degassing process can be repeated to ensure that no air bubbles are left inside the solution. The last step was the curing of the solution, that can be done at room temperature for 24 hours or at an elevated temperature (65°C for 2 hours) to expedite the polymerisation.

A PDMS-ceramic composite solution was also prepared, which was applied during one of the antenna demonstrations in Section IV. The solution was prepared by homogeneously dispersing ceramic powders into the PDMS solution [49]. Strontium Titanate ( $\text{SrTiO}_3$ ) ceramic powder was used in this work owing to its very high relative permittivity of 270 and a low loss tangent, below 0.001 at microwave frequencies [53, 54]. Depending on the volume concentration of the  $\text{SrTiO}_3$  mixed to the solution, the electrical properties of the PDMS can be tuned as shown by the measurement results in Figs 2.2(a) and (b), obtained using an Agilent 85070E Dielectric Probe Kit. It is interesting to note in Fig. 2.2 the significant increase in the relative permittivity of PDMS the more ceramic powder that is added, yet with a marginal change in the loss. With 30% volume of  $\text{SrTiO}_3$ , a relative permittivity of up to 9.4 can be obtained. A higher permittivity could be achieved by adding more ceramic powder, but at the expense of reduced flexibility and more complicated fabrication process [55]. During the fabrication, it was observed that with more than 30% volume of  $\text{SrTiO}_3$  ceramic powder the mixture becomes thicker, and thus harder to mix homogeneously.



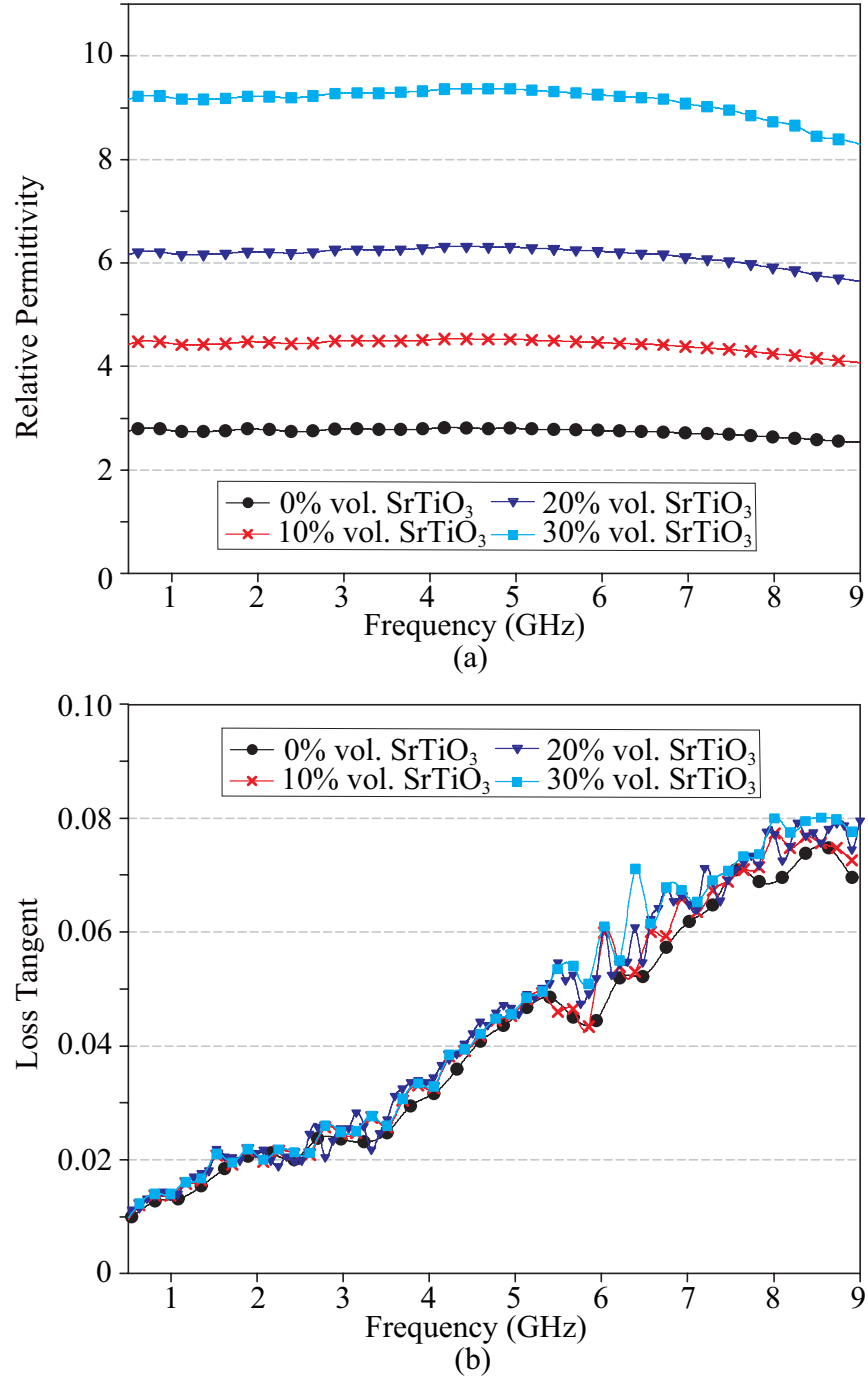


**Figure 2.2:** Measured electrical properties of PDMS at different volume ratio of  $\text{SrTiO}_3$  loading.

(a) Relative permittivity. (b) Loss tangent.

### 2.2.2 Embedding Conductive Fabric inside PDMS

The process of embedding the conductive fabric inside the PDMS layer to build the antenna is done through a multilayer fabrication approach depicted in Fig. 2.3. It starts from the bottom and goes to the top encapsulation layer for an easy integration of each part of the design. Generally, the process can be divided into the following steps.

1. Prepare the solutions, moulds, base, and cut the conductive fabric manually following the dimensions of the antenna.
2. Attach the first mould to the base with a silicone sealant, pour the PDMS solution into the mould, degas in a vacuum desiccator for approximately 30 minutes, and then cure in an oven at 65°C for about 2 hours.
3. Attach the ground plane on top of the cured bottom encapsulation layer with a thin uncured PDMS solution, repel the bubbles occurring between them, and cure in the oven at 75°C for 20 minutes.
4. Repeat Step 2 with the second mould to make the middle PDMS layer.
5. Repeat Step 3 for the main patch.
6. Repeat Step 2 with the third mould to make the top encapsulation layer.
7. Peel carefully the prototype from the mould. If necessary, trim the excess PDMS layers from the edges of the antenna.

Taking advantage of the initial liquid state of PDMS, customised ring-shaped moulds made out of commercial laminates from Taconic with the required thicknesses were used, into which the PDMS solution was poured to guarantee the accuracy of the thickness of each layer. To make the mould, a rectangular aperture that is big enough to contain the design was made on each laminate. To achieve good PDMS-PDMS layer bonding,

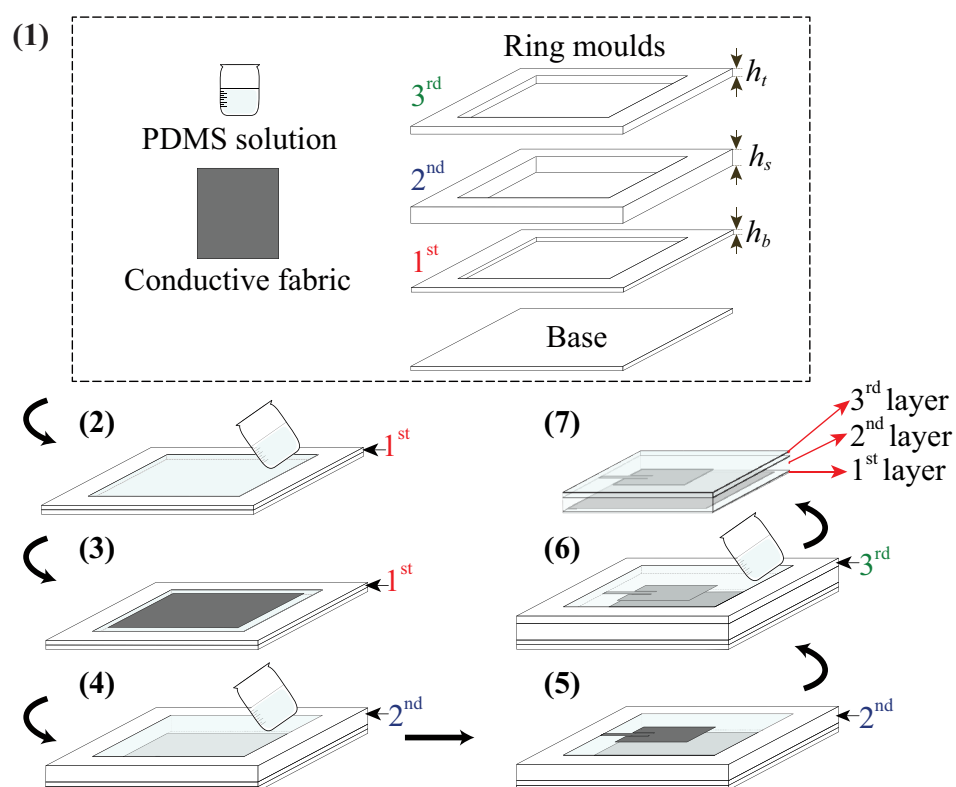


**Figure 2.3:** Schematic illustration of the fabrication process of the PDMS-embedded conductive-fabric based antennas. The numbers represent the order of the process.

the PDMS solution was directly poured and cured over a cured PDMS layer during the multilayer fabrication [56].

The bottom and top encapsulation layers were cut slightly at the edges of the transmission lines, to be able to attach a SubMiniature Version A (SMA) connector for measurement purposes. The attachment was done by means of silver epoxy, and to cure it the antenna was left again in the oven at 65°C for another 1 hour.

## 2.3 Characteristics of PDMS-Embedded Conductive Fabric

Before applying the proposed PDMS-embedded conductive fabric technology to the antenna design, the characterisation of its mechanical and electrical properties was carried out, and the results are discussed in this section.

### 2.3.1 Mechanical Characterisation

To investigate the mechanical properties of the PDMS-embedded conductive fabric, four samples out of the four different conductive fabrics listed in Table 2.1 were fabricated through the antenna fabrication process described before. For validation purposes, three prototypes were made for each type of sample, all with the same dimensions as depicted in Fig. 2.4(a). To highlight the advantage of this approach compared with previously reported work, where the conductive fabrics were attached on the surface of the PDMS substrate [25–27], a non-encapsulation-layer version of all samples was also prepared as illustrated in Fig. 2.4(b).

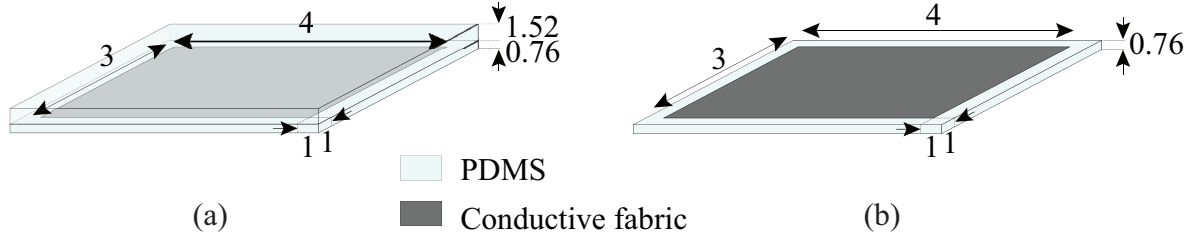


**Figure 2.4:** Illustration of the samples, when: (a) the conductive fabric is embedded inside the PDMS, (b) the conductive fabric is simply attached on the PDMS surface. All dimensions are in millimetres.

As illustrated in Fig. 2.5(a), all of the samples were subjected to a set of mechanical stress tests including severe rolling, twisting, and bending, each repeated 50 times. The tests were conducted in two cycles, and comparisons between the samples before and after each test cycle are given in Figs 2.5(b) and (c). The results show that the PDMS-embedded conductive fabric approach provides a significantly improved physical robustness compared to the previous method of attaching the conductive fabric on the surface of a PDMS layer. During the tests, it was observed that without the PDMS encapsulation layer the tendency of the fabric to detach from the substrate, often starting from the edge and expanding further to the whole part of the fabric, is still very high, resulting in what is shown in Fig. 2.5(c). These results also indicate that samples fabricated with the previous method may not endure washing.

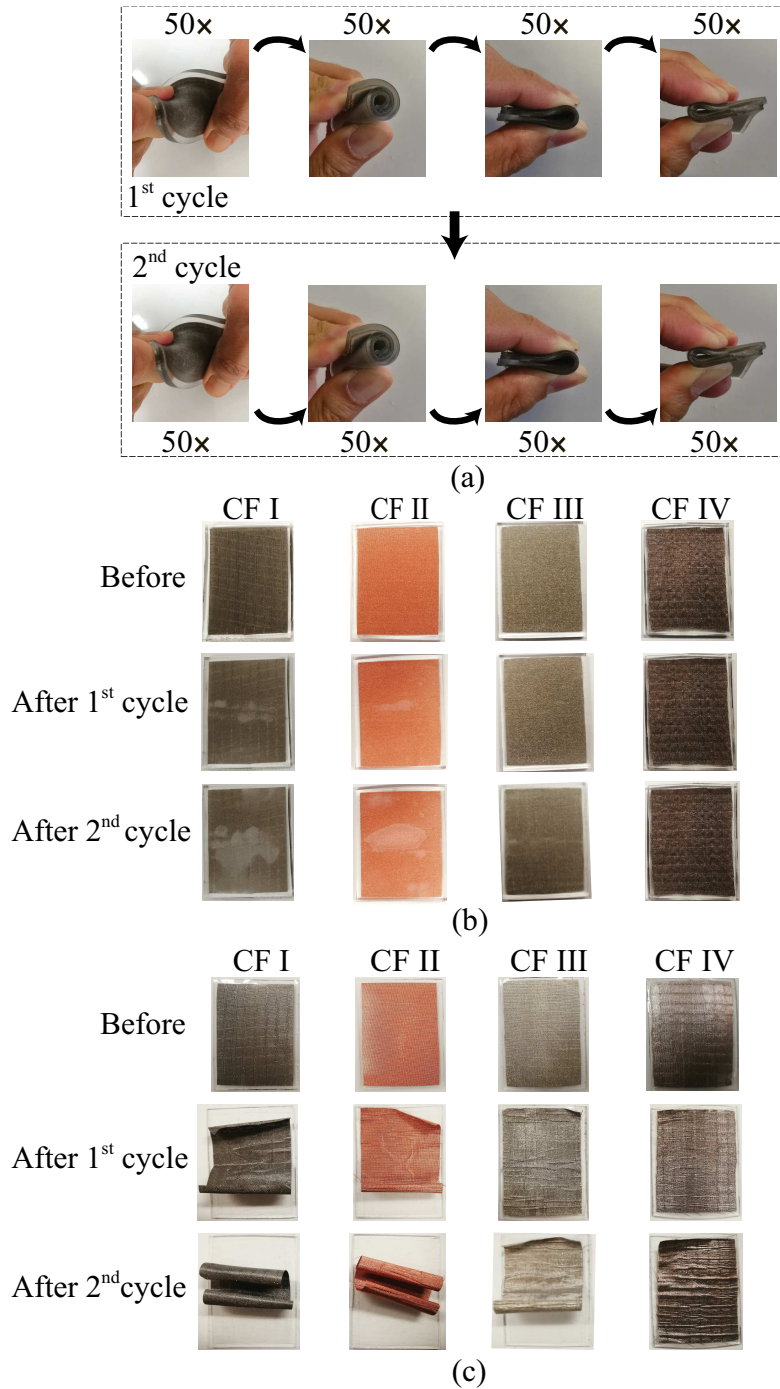


**Figure 2.5:** (a) Illustration of mechanical testing scenarios which consist of two cycles of repetitive deformations. Photograph of the samples before and after tests, when: (b) the conductive fabric is embedded inside the PDMS layer; (c) the conductive fabric is simply attached on top of the PDMS layer.

### 2.3.2 Stability due to Structural Characteristics

The mechanism behind the mechanical robustness of the PDMS-embedded conductive fabric approach can be explained as follows: the porous surface of the conductive fabric allows the PDMS in its initial liquid form to penetrate through the conductive fabric and bond with the PDMS encapsulation layer on the other side of the conductive fabric. This phenomenon can be seen clearly in Fig. 2.6, where a small piece of the sample, with conductive fabric embedded inside the PDMS layer, was torn partly on the top layer and observed under a scanning electron microscope (SEM). Normally, the adhesion between PDMS and conductive elements like metals is weak [25, 43]. However, with the extra support from the PDMS-PDMS layer adhesion created through the pores of the fabric, which is much stronger than that of the PDMS and conductive fabric, a better structural integration is obtained, thus allowing the structure to stand against severe deformations.

As an implication, the mechanical stability of the PDMS-embedded conductive fabric depends upon the porosity of the conductive fabric, as it determines the amount of PDMS-PDMS layer bonding that can be achieved across the fabric. In Figs 2.7(a)–(d) photos of the four conductive fabrics under a fluorescence microscope with ten times magnification are given. The figures show an increasing porosity from CF I to CF IV. This explains the mechanical testing results in Fig. 2.5(b), where the mechanical robustness of the sample increases from CF I to CF IV. It is determined by the amount of white mark across the samples, that decreases from CF I to CF IV. The white mark indicates the gap formed between the conductive fabric and PDMS due to repeated severe deformations. Although for some combinations the gap can still appear, it is worth noting that in this approach the conductive fabric still retains its electrical connectivity as it does not suffer from the crack formation as in a flexible PCB substrate under severe bending. Moreover, in contrast to the samples fabricated with previous methods (Fig. 2.5(c)), the conductive fabric remains inside the PDMS layer, thus is still protected from being peeled off or washed away.

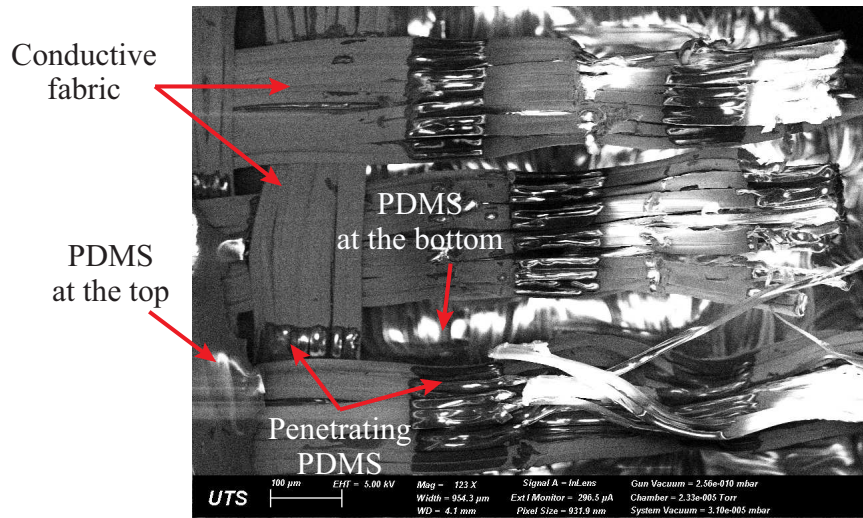


**Figure 2.6:** SEM image view of a PDMS-embedded conductive fabric sample.

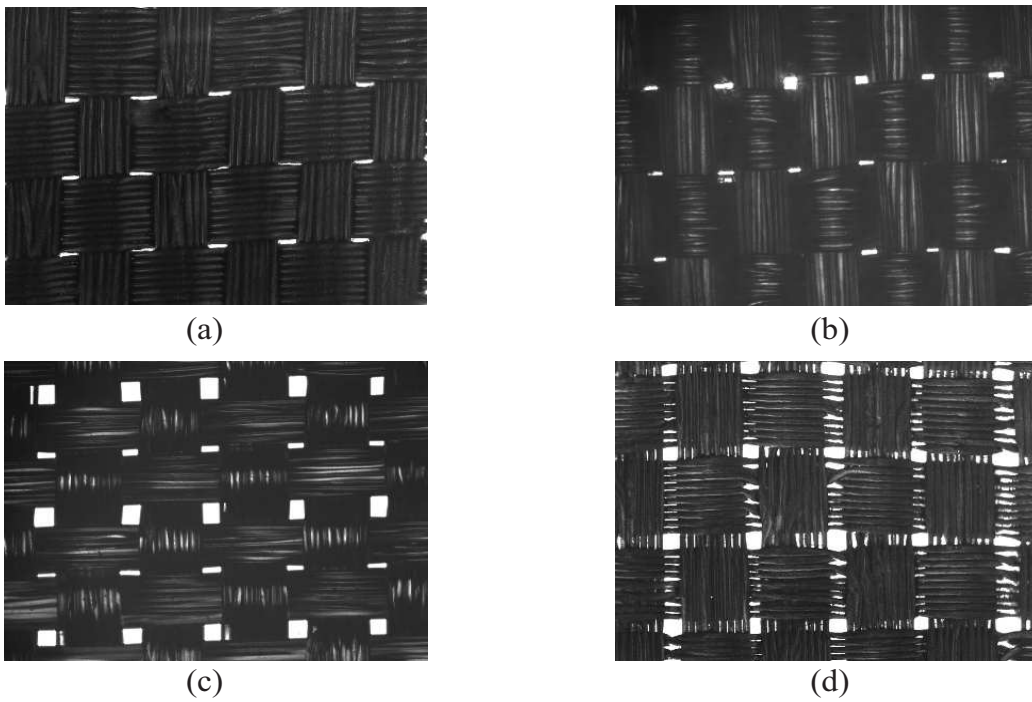


**Figure 2.7:** Photograph of the conductive fabric under a fluorescence microscope. (a) CF I. (b) CF II. (c) CF III. (d) CF IV.



### 2.3.3 Electrical Properties

To characterise the electrical properties of the PDMS-embedded conductive fabric, four  $50\ \Omega$  microstrip transmission lines having the dimensions shown in Fig. 2.8(a) were fabricated and measured. The fabricated prototypes are shown in Fig. 2.8(b). Additional loss in the conductive part was observed, likely caused by the PDMS penetration into the conductive fabric, and therefore needs to be considered during the simulation to attain an accurate design. To do that, the effective conductivity of the conductive fabric which was modelled in the Computer Simulation Technology (CST) Microwave Studio 2016 using a box with the fabric thickness, was adjusted until the best match between the simulated and measured  $|S|$ -parameters was achieved [57]. For better accuracy, the values were also validated using the T-resonators [58] shown in Figs 2.9(a) and (b), designed and fabricated using the PDMS-embedded conductive fabric. The effective conductivity was adjusted until the resonance in simulation matches well with that of the measurement, as shown in Figs 2.10(a)–(d).

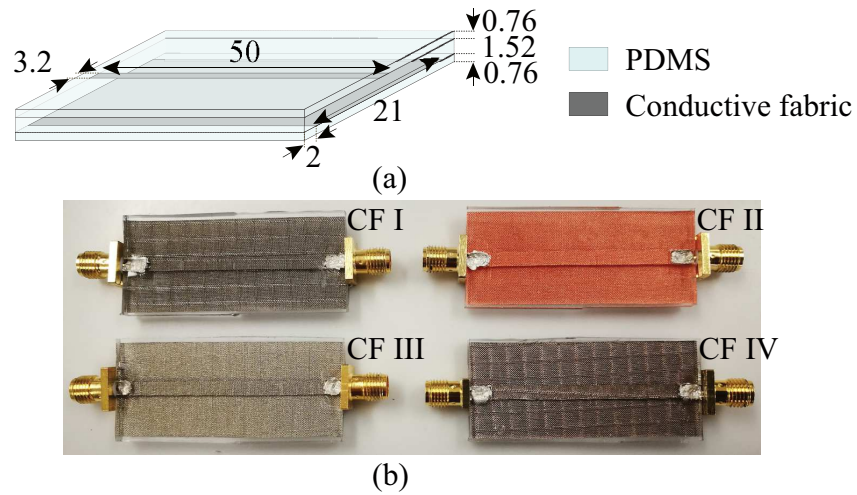


**Figure 2.8:** PDMS-embedded conductive fabric transmission lines. (a) Design (All dimensions are in millimetres). (b) Photograph of prototypes fabricated with four different conductive fabrics.

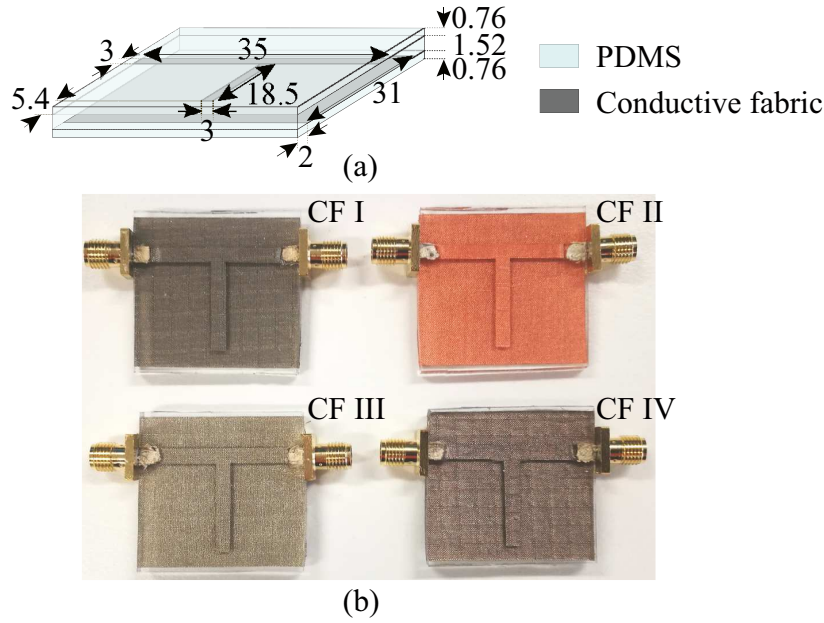


**Figure 2.9:** PDMS-embedded conductive fabric T-resonators. (a) Design (All dimensions are in millimetres). (b) Photograph of prototypes fabricated with four different conductive fabrics.

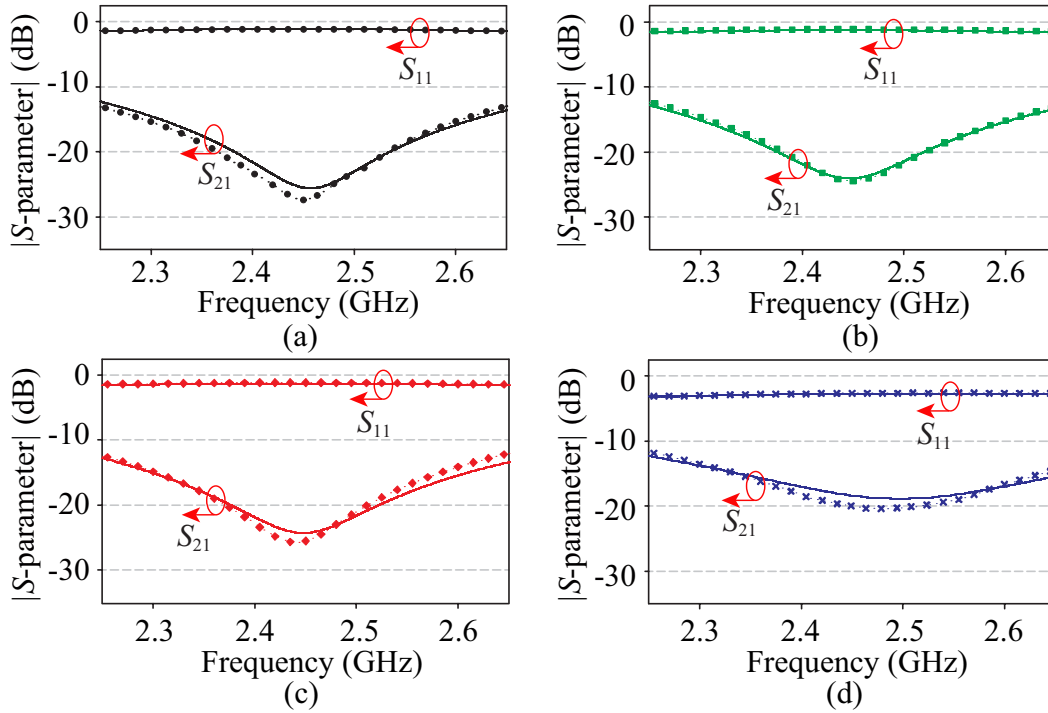


**Figure 2.10:** Simulated (solid lines) and measured (dotted lines)  $|S|$ -parameters of PDMS-embedded conductive fabric T-resonators with (a) CF I, (b) CF II, (c) CF III, and (d) CF IV.

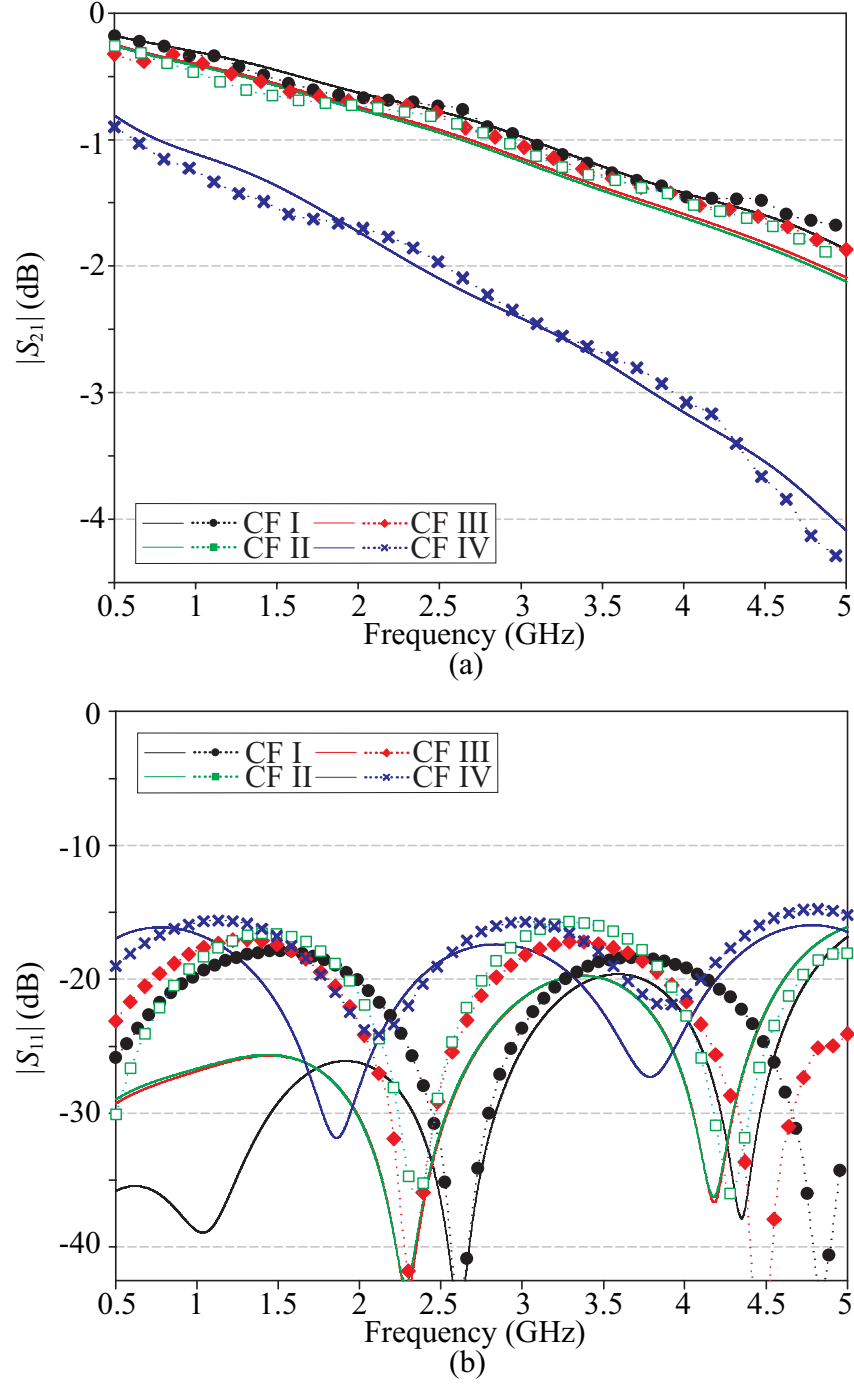


**Figure 2.11:** Simulated (solid lines) and measured (dotted lines) (a) transmission coefficient ( $|S_{21}|$ ) and (b) input reflection coefficient ( $|S_{11}|$ ) of the PDMS-embedded conductive fabric transmission lines.

**Table 2.2:** Adjusted Effective Conductivity Used to Model the Conductive Fabrics Embedded in PDMS

Conductive Fabric Type	Adjusted $\sigma$ (S/m)
CF I	$1.02 \times 10^5$
CF II	$5 \times 10^4$
CF III	$5.4 \times 10^4$
CF IV	$4.8 \times 10^3$

Note:  $\sigma$  = effective conductivity

The comparison between the simulated and measured  $|S|$ -parameters of the transmission lines after adjusting the effective conductivity value is shown in Figs 2.11(a) and (b). For all prototypes the return loss is above 16 dB over the whole observation band, and as expected the insertion loss varies, indicating the different conductivity of each conductive fabric used. The adjusted conductivity values, which are lower than those of the plain conductive fabric provided in the datasheet, are given in Table 2.2. These are the values which were applied to model the conductive fabric embedded in PDMS during the antenna design stage. As can be seen, CF I appears to have the highest conductivity, whereas CF IV has the lowest conductivity.

From both mechanical and electrical characterisations, it can be implied that, in principle, any conductive fabric can be utilised to realise a PDMS-embedded conductive fabric based antenna. However, there will always be a trade-off between mechanical robustness and RF performance of the fabricated antenna, which is strongly dependent on the mechanical and electrical properties of the conductive fabric. As previously shown, generally, the conductive fabric with superior attachment to the PDMS, performs electrically worse, and vice versa. To achieve both excellent mechanical and RF performance is a challenge

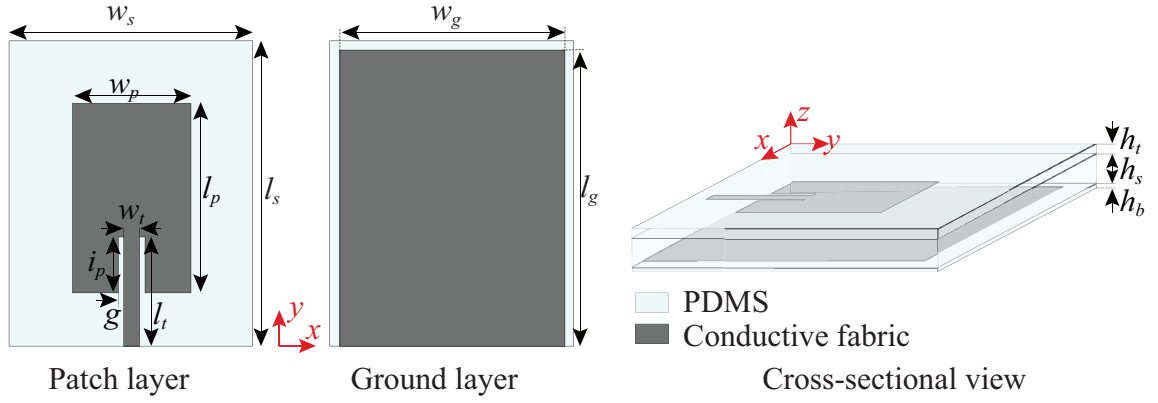


**Figure 2.12:** Patch antenna design for concept demonstration.

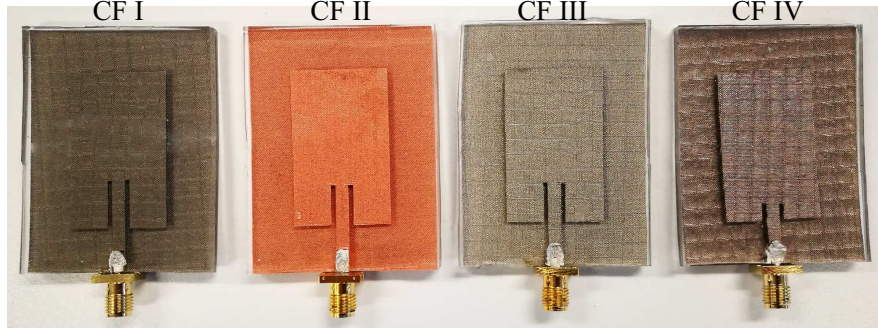


**Figure 2.13:** Patch antennas fabricated with four different conductive fabrics.

that is left for future work.

## 2.4 PDMS-Embedded Conductive Fabric in Realisation of Flexible Antennas

To validate the applicability of the proposed approach for realisation of conformal antennas, the combinations of PDMS and the four conductive fabrics used before were applied to an inset-fed rectangular patch antenna design illustrated in Fig. 2.12. Each conductive fabric acts as the patch and ground-plane layers of the antenna, whereas PDMS layers are used as the substrate and encapsulation that fully covers the antenna. For each combina-

tion, the antenna was optimised to have a fundamental-mode operation at the Industrial, Scientific, and Medical (ISM) 2.45 GHz and fabricated through the same bottom-up multilayer approach described in Section 2.2.2. The photograph of fabricated prototypes are shown in Fig. 2.13. The final dimensions of the antennas are given in Table 2.3.

**Table 2.3:** Detailed Dimensions of Patch Antennas Designed with Four Different Conductive Fabrics

Parameter	Antenna Dimension (mm)			
	CF I	CF II	CF III	CF IV
$w_s$	50.3	50.3	50.3	50.3
$l_s$	59.6	59.5	59.5	58.7
$w_g$	42.3	42.3	42.3	42.3
$l_g$	55.6	55.5	55.5	54.7
$w_p$	22.3	22.3	22.3	22.3
$l_p$	35.6	35.5	35.5	34.7
$w_t$	3	3	3	3
$l_t$	21	19	19	13.5
$i_p$	11	9	9	3.5
$g$	1	1	1	1
$h_t$	0.76	0.76	0.76	0.76
$h_s$	2.5	2.5	2.5	2.5
$h_b$	0.2	0.2	0.2	0.2

Figs 2.14(a)–(b) show the effect of the encapsulation layers on the performance of the antenna, using the CF I patch antenna as the example. As can be seen, the bottom encapsulation layer does not have any impact on the antenna performance, whereas the PDMS layer added on top of the antenna causes a down shift in the resonance frequency, or equivalently helps in reducing the patch size slightly. This phenomenon is expected, since adding a dielectric material on top of the antenna causes a decrease in the guided wavelength which thus increases the electrical length of the patch and hence a decrease in the resonance frequency [59]. In addition to that, a minor decrease in the peak gain is also noticed after adding the top encapsulation layer, which is attributed to the extra loss from the PDMS layer. However, this can be minimised by using a thinner encapsulation layer.

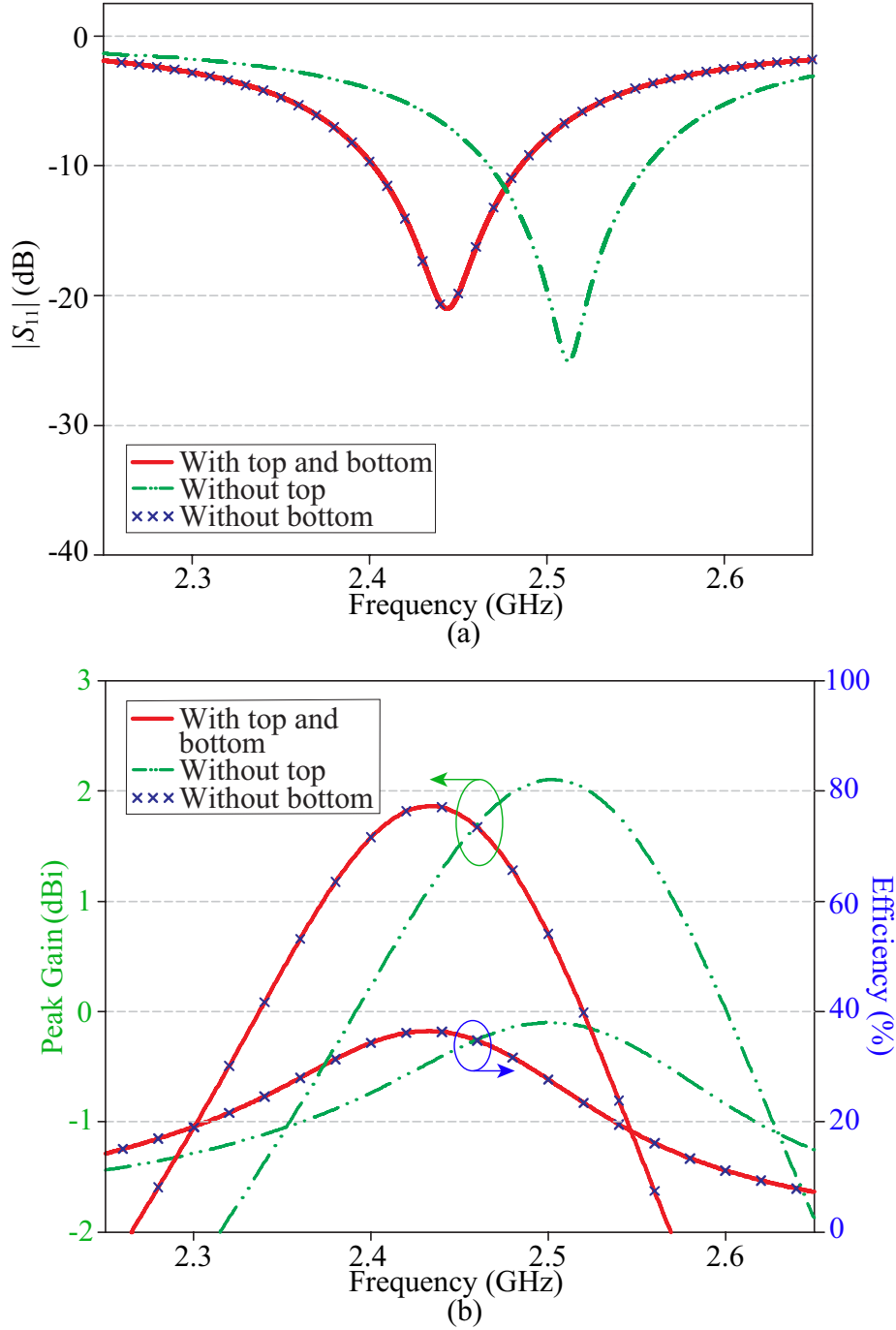


**Figure 2.14:** The effect of encapsulation layers to the performance of the antenna: (a)  $S_{11}$ . (b)

Peak gain and total efficiency. Simulated results of CF I patch antenna are used as an example.



## 2.5 Measurements and Results

The RF performance of all prototypes was characterised, covering  $|S_{11}|$  measurements using the Agilent PNA-X N5242A, calibrated with an electronic calibration module N4691B from Keysight, and far-field measurements in the NSI700S-50 spherical near-field antenna range at the Australian Antenna Measurement Facility (AusAMF), Marsfield. For the  $|S_{11}|$  performance, the measurements were conducted when the antennas were flat and bent around a plastic tube having a radius of 35 mm (see Fig. 2.15). Special care has been taken while bending the antennas to maintain the connection between the SMA and the feeding line.

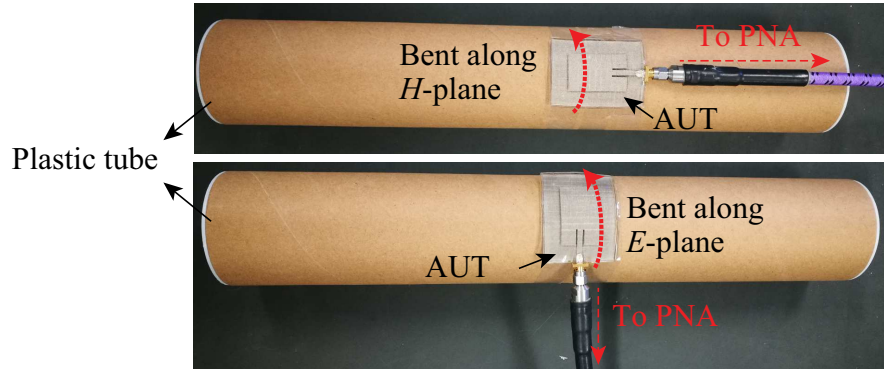


**Figure 2.15:** Illustration of bending the antenna around the plastic tube.

### 2.5.1 Input Matching

As shown in Figs 2.16(a)–(d), there is a good agreement between the measured  $|S_{11}|$  results and those of the simulations. The fabricated prototypes have a resonance approximately at 2.46 GHz with a 10-dB return-loss bandwidth ranging from 3.3 to 5.7%. The minor differences between the simulated and measured results might be caused by the fabrication error during the manual cutting of the fabric, especially CF IV whose edges easily suffered from fraying. When the antennas were bent around the plastic tube, the antennas remained functional despite slight shifts in their resonance frequencies, especially during bending along the  $E$ -plane of the antenna (see Figs 2.16(a)–(d)). This is expected as it affects the main current path of the antenna. However, most importantly as demonstrated before, the conductive fabric remains intact inside the PDMS encapsulation.

### 2.5.2 Far-Field Characteristics

The desired boresight radiations are achieved from all prototypes with a good agreement between the measured and simulated results (see Figs 2.17(a)–(d)). The gains and total efficiencies of all prototypes, measured at their resonance frequencies, are given in Table 2.4, and again agree well with the simulated results. As expected, the antenna fabricated with CF I has the highest efficiency and gain, whereas the one with CF IV has the lowest efficiency and gain.

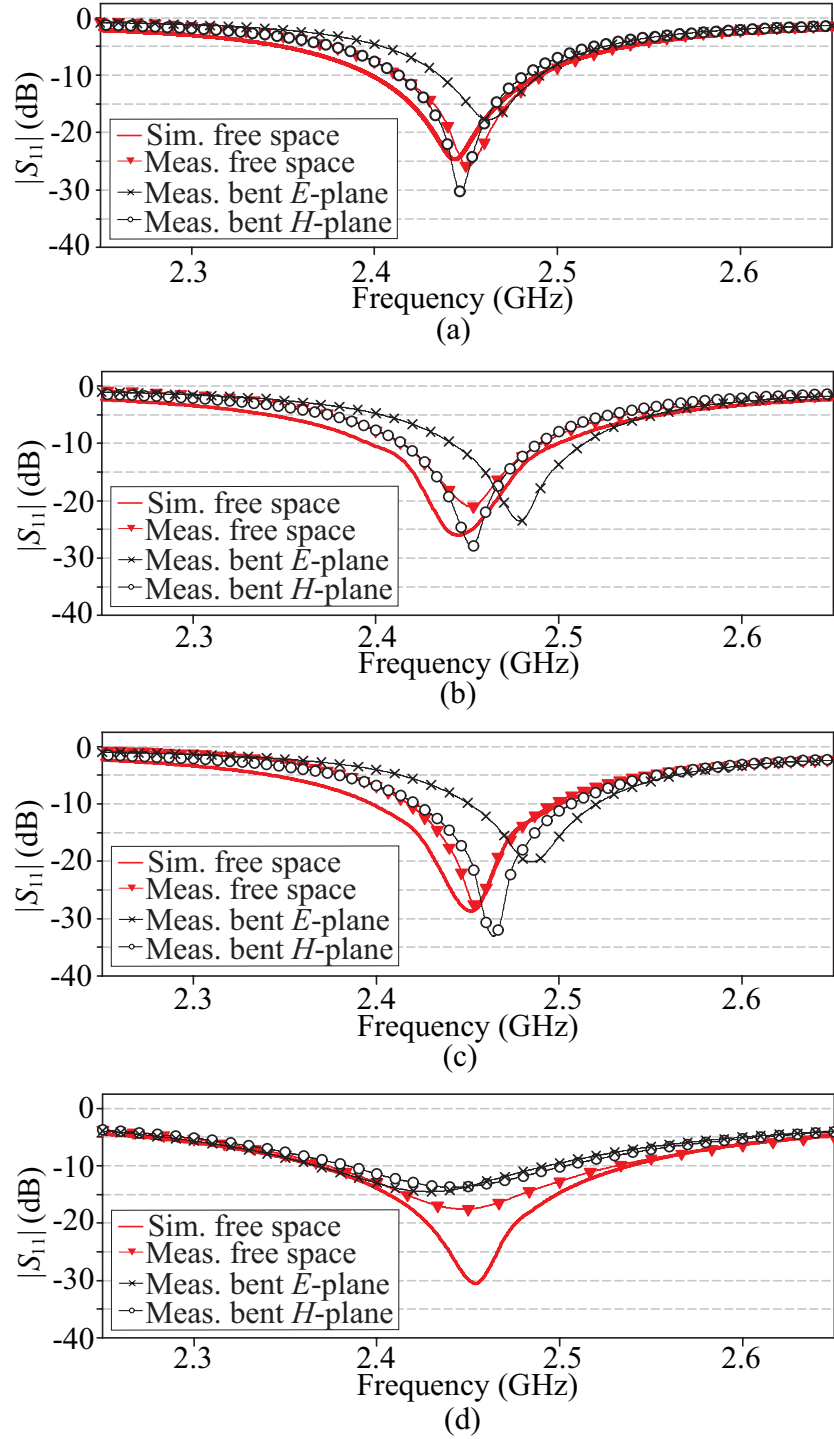


**Figure 2.16:** Simulated and measured  $|S_{11}|$  of the prototype with: (a) CF I, (b) CF II, (c) CF III, and (d) CF IV.

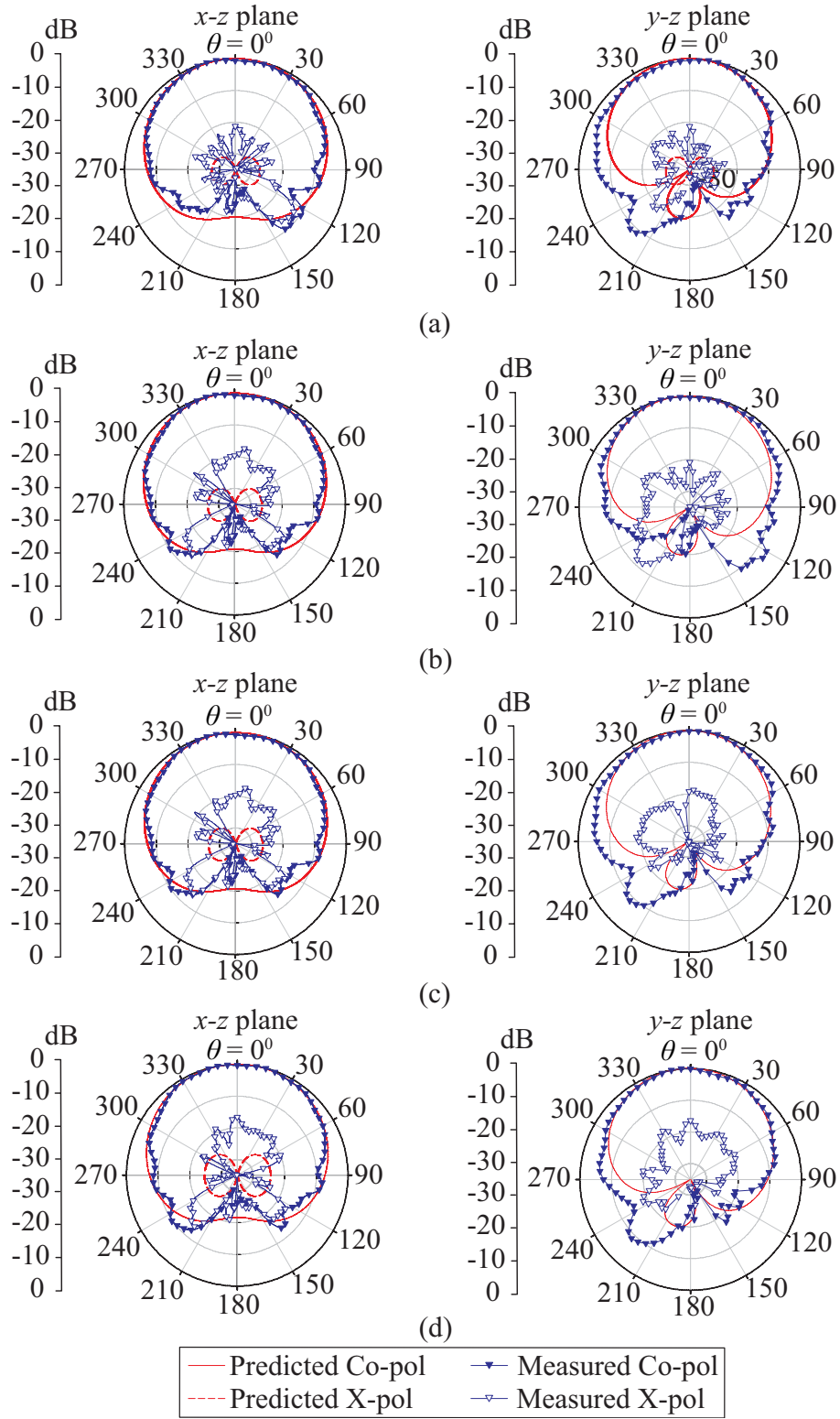


**Figure 2.17:** Normalised simulated and measured radiation patterns of the prototype with: (a) CF I, (b) CF II, (c) CF III, and (d) CF IV.

**Table 2.4:** Summary of the Antenna Prototypes' Peak Gains and Total Efficiencies in Free Space

Antenna	Gain (dBi)		Tot. Eff.(%)	
	Sim.	Meas.	Sim.	Meas.
CF I	1.85	1.75	36.3	35.6
CF II	1.47	1.36	33.1	31.5
CF III	1.53	1.45	33.6	32.1
CF IV	-0.74	-0.82	20.1	19.7

## 2.6 Summary

A simple yet effective approach for realising flexible and mechanically robust wearable antennas is presented. The method combines the conductive fabric used to form the conducting parts of the antenna with PDMS that acts simultaneously as a substrate and encapsulation layers. The mechanical and electrical properties of such combinations of materials have been investigated experimentally. It was shown that, by embedding the conductive fabric inside the PDMS, a stronger integration between them can be achieved, thanks to the PDMS-PDMS bonding formed through the pores of the fabric. There is a trade-off between mechanical stability and radiation performance when selecting the conductive fabric for the antenna design. The fabric with high porosity leads to a more resilient antenna against physical deformations, but it suffers from low total efficiency due to the low effective conductivity. It was also observed that the penetration of PDMS into the fabric needs to be considered in the simulation to obtain an accurate antenna design.

The proposed approach was validated by studying the performance of fabricated rect-

angular patch antennas. A good agreement between the simulated and measured results showed that the materials and methods involved allow reliable antenna optimisation using regular modelling approaches. In the next chapters, more application examples are given to further validate the applicability of the proposed approach for antenna realisation.

# Simple Dual-Band Dual-Mode Wearable Antenna based on PDMS-Embedded Conductive Fabric

## 3.1 Introduction and State of the Art

In certain applications such as a health-care monitoring system, wearable devices may be required to be able to communicate not only with remote terminals outside the body (off-body channel), but also with other wearable devices located on the user's body (on-body channel). Consequently, there is a need for wearable antennas which can provide different radiation characteristics in different bands, for instance: a patch-like radiation in one band for an off-body link and a monopole-like radiation in the other band for an on-body link.

A number of such wearable antennas have been proposed recently: a circular patch antenna arranged concentrically with a shorted annular ring antenna [60] or with a metamaterial-based loop antenna [61]; a half-circular patch antenna loaded with two

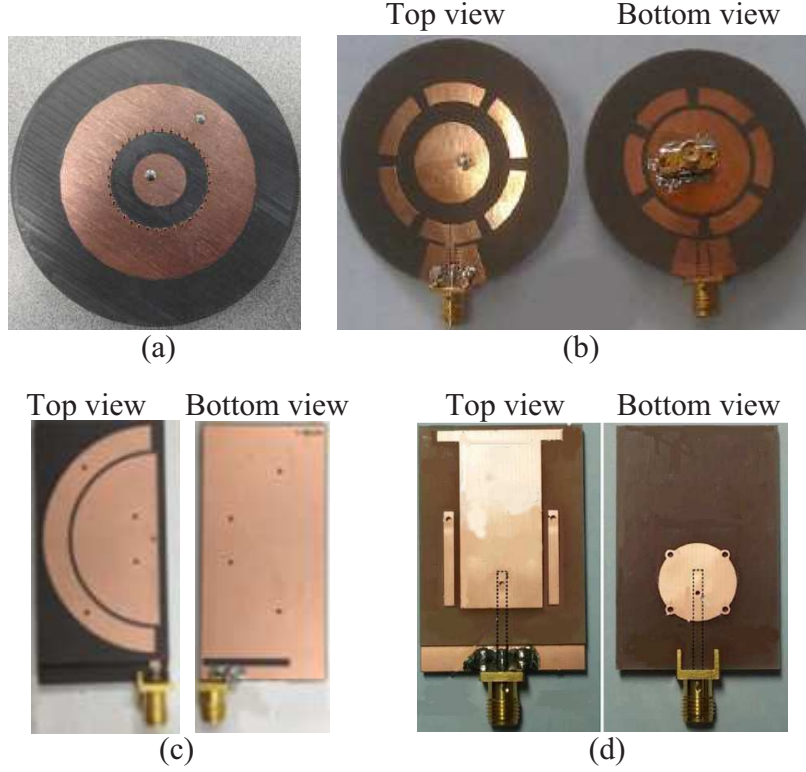


**Figure 3.1:** Previously reported dual-band dual-mode antenna designs. (a) [60]. (b) [61]. (c) [62]. (d) [63].

shorting pins and a slot on the ground [62]; and a shorted circular patch antenna incorporated with a T-shaped patch antenna and some parasitic patches on the opposite side of the substrate [63]. Generally, the dual-band dual-mode operation was achieved previously by integrating two radiators, fed by a single or two-port system, where each radiator operates at a different frequency and provides a different radiation pattern (see Figs 3.1(a)–(d)). Furthermore, they were made of conventional rigid materials which limits their application for wearable systems.

In this chapter, with the motivation to reduce design complexity and improve the wearability issues faced by the previous designs [60–63], a new dual-band dual-mode antenna design realised with the proposed PDMS-embedded conductive-fabric technology is presented. Instead of using two different radiators, the off- and on-body modes are



achieved by utilising the inherently generated  $TM_{11}$  and  $TM_{02}$  modes of a single probe-fed circular patch antenna. The antenna configuration and the fabricated prototype are presented in Section 3.2. Following that, in Section 3.3 the antenna performance is shown in both free space and the on-body environment. A summary in Section 3.4 concludes this chapter.

## 3.2 Design of Dual-Band Dual-Mode Antenna

The proposed antenna, as shown in Fig. 3.2, is based on a conventional circular-patch antenna configuration. A circular patch with a radius of  $r_c$  is at the top of the PDMS substrate, while a full ground plane with a radius of  $r_g$  is maintained on its opposite side. Based on the analysis in Section 2.3, CF I was utilised for realising the patch layer due to having the highest conductivity of the four conductive fabrics. Concurrently, CF III was used as the ground plane. The latter choice was because of its higher porosity, with a better conductivity than CF IV, which is, in turn, beneficial for the PDMS-fabric adherence over such a large area like the entire ground plane. The full PDMS encapsulation

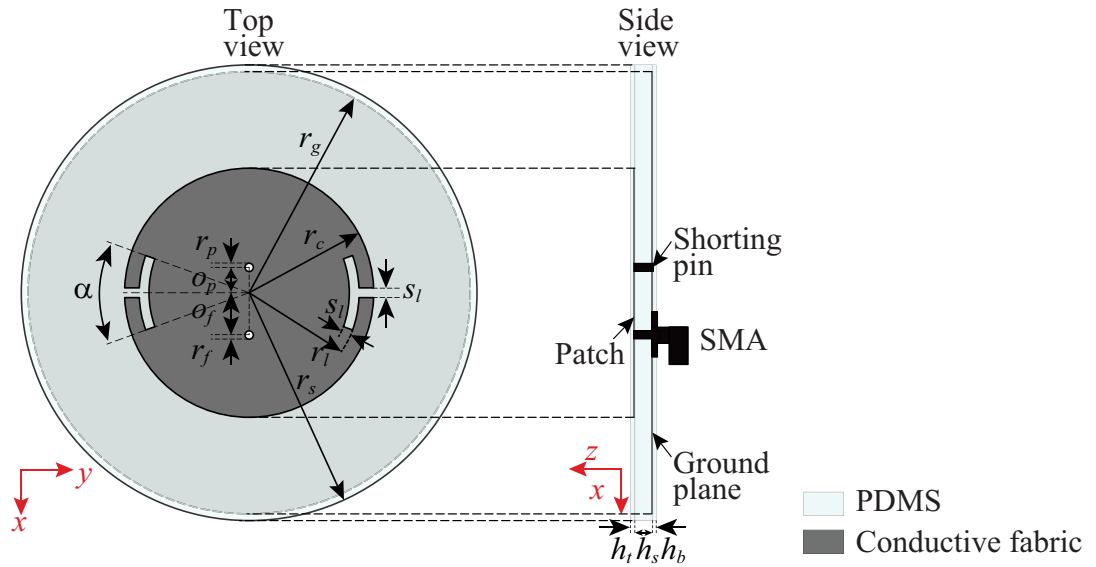


**Figure 3.2:** Detailed geometry of the proposed dual-band dual-mode antenna.

layers are then applied to the antenna (i.e., PDMS layers are added on top of the radiator and ground plane, respectively). A  $50\ \Omega$  coaxial probe is used to feed the antenna at an offset of  $o_f$  from the centre of the patch.

The circular-patch antenna is intended to operate in its  $TM_{11}$  and  $TM_{02}$  modes at the target frequencies of 2.45 and 5.8 GHz, respectively, as these two modes are known for their patch and monopole-like radiations, respectively [64]. In so doing, the dual-band dual-mode antenna can be developed with only one simple radiator and feed. However, it is known that, for a given geometry of the patch, all generated resonance frequencies corresponding to the various modes are related in fixed ratios, thus providing no possibility of dual-band operation at arbitrary frequencies [65].

To overcome the above-mentioned limitation, reactive loading in the form of a shorting pin and two arc-shaped slots [65] was introduced to the patch. To maintain the simplicity of the structure, only one pin was considered in this design, and was placed at a radial distance of  $o_p$  from the centre of the patch, but towards the opposite direction of the feed point. The two arc-shaped slots were positioned symmetrically with respect to the centre of the patch. The simultaneous use of the shorting pin and arc-shaped slots allows tuning of the resonances of both target modes, as it modifies the current path on the patch. It can be seen from Fig. 3.3(a) that, when the pin is placed further from the centre of the patch, the first mode's resonance frequency increases while the second mode's resonance frequency decreases slightly. On the other hand, as shown in Figs 3.3(b) and (c), when the width or the length of the slots increases, the resonance frequency of both modes decreases. The change in the width of the slots gives a more significant effect in the first mode, while the change in the length of the slots gives a more significant effect in the second mode. The real part of the input impedance may also be varied by tuning the position of the pin, the width and the length of the slots, which suggests a change in the antenna's impedance matching.

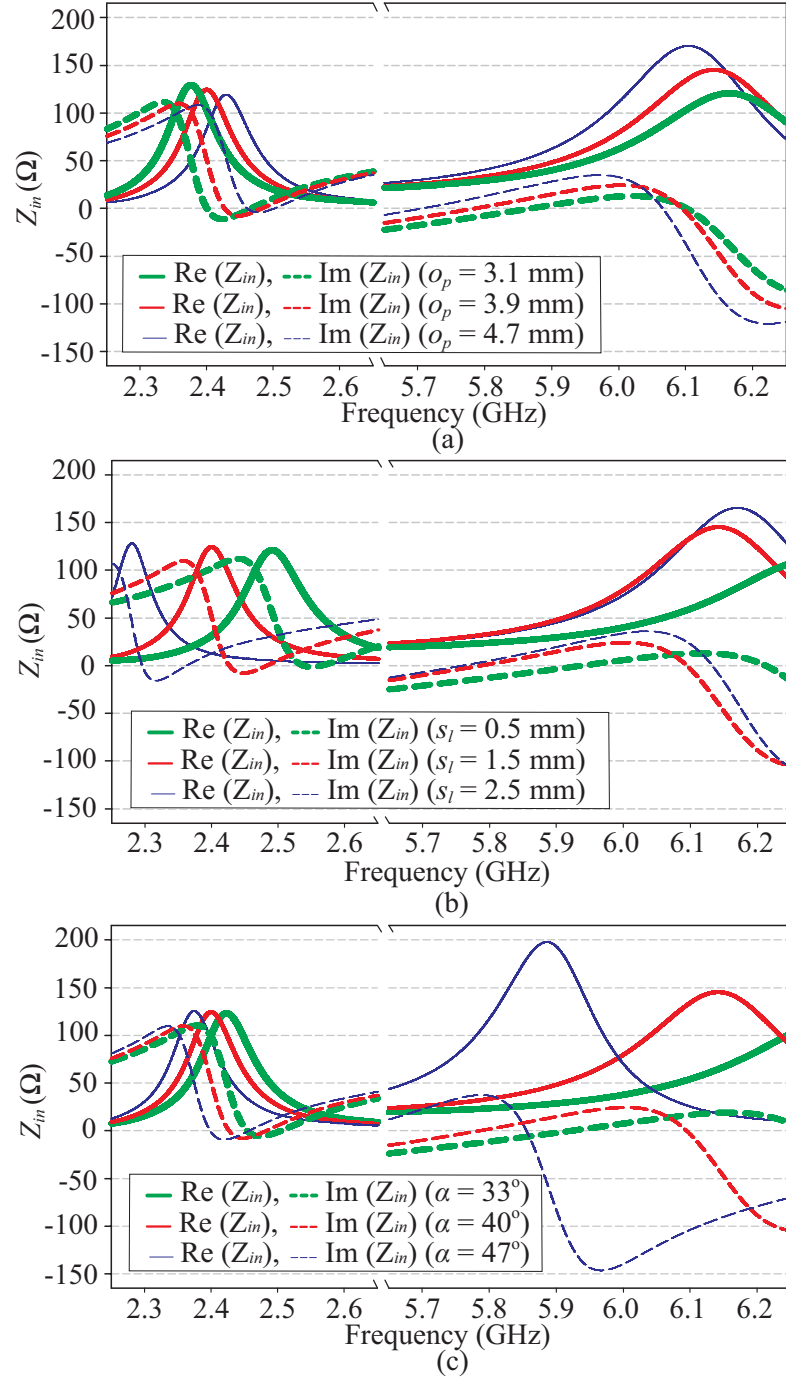


**Figure 3.3:** Simulated input impedance for (a) various positions of the pin ( $o_p$ ) when  $\alpha = 40^\circ$  and  $s_l = 1.5$  mm; (b) various widths of the slots ( $s_l$ ) when  $\alpha = 40^\circ$  and  $o_p = 3.9$  mm; (c) various lengths of the slots ( $\alpha$ ) when  $s_l = 1.5$  mm and  $o_p = 3.9$  mm.

**Table 3.1:** Dimensions of the Proposed Dual-Band Dual-Mode Antenna

Parameter	Dimension	Parameter	Dimension
$\alpha$	40°	$r_c$	19.2 mm
$o_p$	3.9 mm	$r_g$	34 mm
$o_f$	6.5 mm	$r_s$	35 mm
$r_f$	0.64 mm	$h_t$	0.2 mm
$r_p$	0.64 mm	$h_s$	3 mm
$s_l$	1.5 mm	$h_b$	0.2 mm
$r_l$	16.9 mm		

With the aid of full-wave simulations in CST Microwave Studio 2016, the optimum design of the antenna is obtained and given in Table 3.1. The current distribution of the proposed antenna and the corresponding electric field are illustrated in Figs 3.4(a) and (b), confirming that the antenna operates in the  $TM_{11}$  and  $TM_{02}$  modes at 2.45 and 5.8 GHz, respectively [64]. It is noted that the current paths are perturbed around the pin and arc-slots which explains the mechanism of the mode's resonance tuning stated before.

Through the process described in Section 2.2.2, the antenna prototype was realised. Three circular moulds, each having diameter and depth following the total diameter and thickness of each PDMS layer, was used to ensure fabrication accuracy. For the realisation of the shorting pin, a copper pin was inserted into the cured PDMS and connected to both the patch and ground plane using a silver epoxy. The same treatment was applied for connecting the SMA from the underside of the substrate. A small 90° bent SMA was utilised for ease of measurement on the phantoms. A photograph of the fabricated prototype is shown in Fig. 3.5.

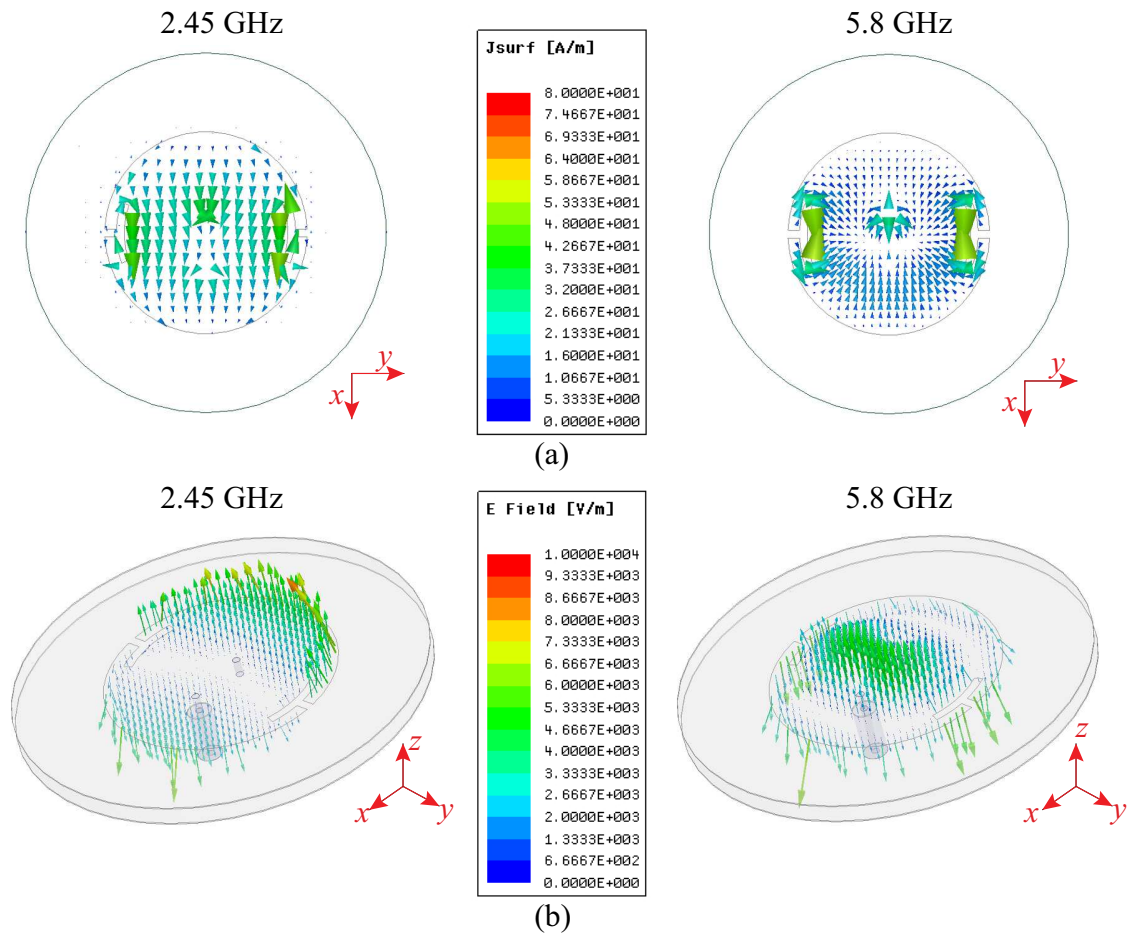


**Figure 3.4:** (a) Current and (b) electric-field distribution of the proposed antenna at 2.45 and 5.8 GHz.

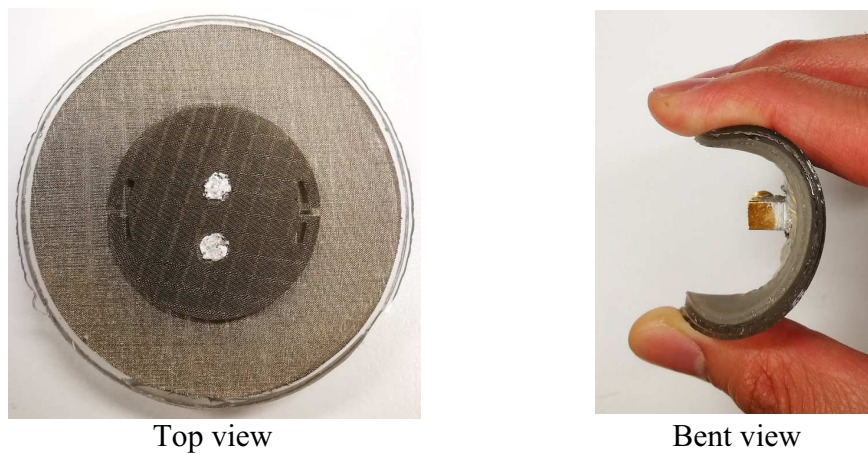


**Figure 3.5:** Photographs of the fabricated dual-band dual-mode antenna.

### 3.3 Dual-Band Dual-Mode Antenna Performance

#### 3.3.1 Experimental Setup

The performance of the antenna was validated experimentally in both free space and an on-body environment. The  $|S_{11}|$  measurements were conducted using an Agilent PNA-X N5242A network analyser, which was calibrated using an electronic calibration module N4691B from Keysight. For the far-field characterisation, the measurements were done in the NSI700S-50 spherical near-field antenna range at the AusAMF, Marsfield.

For on-body measurements, two UWB homogeneous human-muscle equivalent phantoms were fabricated. One is a flat phantom with dimensions of 200 mm  $\times$  200 mm  $\times$  50 mm (Fig. 3.6(a)) and the other is a human-shaped phantom (Fig. 3.6(b)). The first was utilised to investigate the loading effects of the lossy body tissue on the antenna performance, while the second was utilised to investigate any performance degradation when the antenna was conformed to the body shape in several locations to resemble realistic wearing scenarios. The muscle-tissue emulating solution for the phantom was prepared following the procedure described below [66]. The materials employed are: deionised water (85.15%) as the main constituent; agar (2.64%) for shape retention; polyethylene powder (PEP) (10.52%) for complex permittivity tuning; sodium chloride (0.18%) for conductivity tuning; TX-151 (1.46%) as a viscosity improver for ease of mixing the PEP and agar; and sodium dehydroacetate (0.05%) as the preservative. These were combined as follows:

1. Heat deionised water in a kettle until boiled then pour it in a beaker glass for mixing.
2. Quickly put sodium dehydroacetate, sodium chloride, and agar into the water and stir.

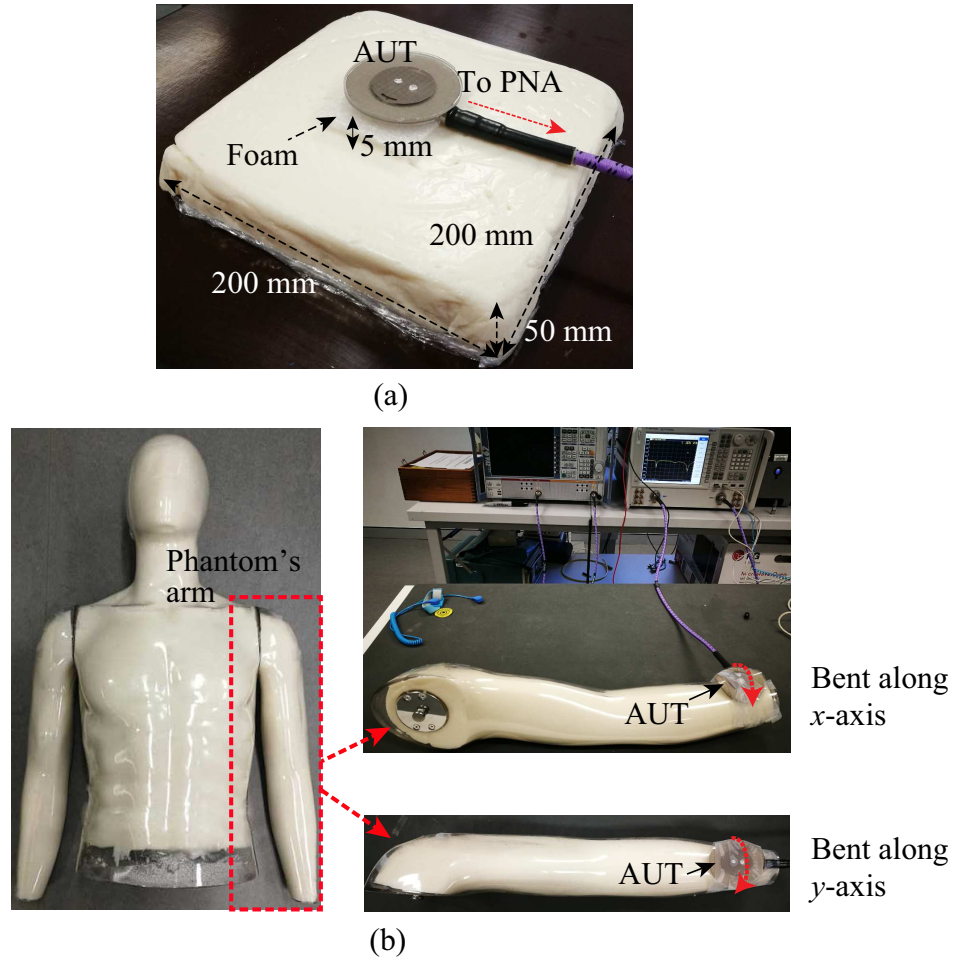


**Figure 3.6:** On-phantom  $|S_{11}|$  measurement setup. (a) The antenna mounted on top of the flat UWB phantom. (b) The antenna wrapped around the wrist of the human-shaped UWB phantom in two different bending configurations.

3. Sprinkle TX-151 into the mixture and quickly mix uniformly.
4. Lastly, add PEP little by little to the mixture and mix uniformly.

To make the flat phantom, the phantom solution was poured into a 200 mm  $\times$  200 mm  $\times$  50 mm mould. After solidification, it was taken out from the mould and wrapped with a plastic film to prevent it from drying. On the other hand, the human-body shaped phantom was prepared by pouring the solution into a hollow human mannequin made

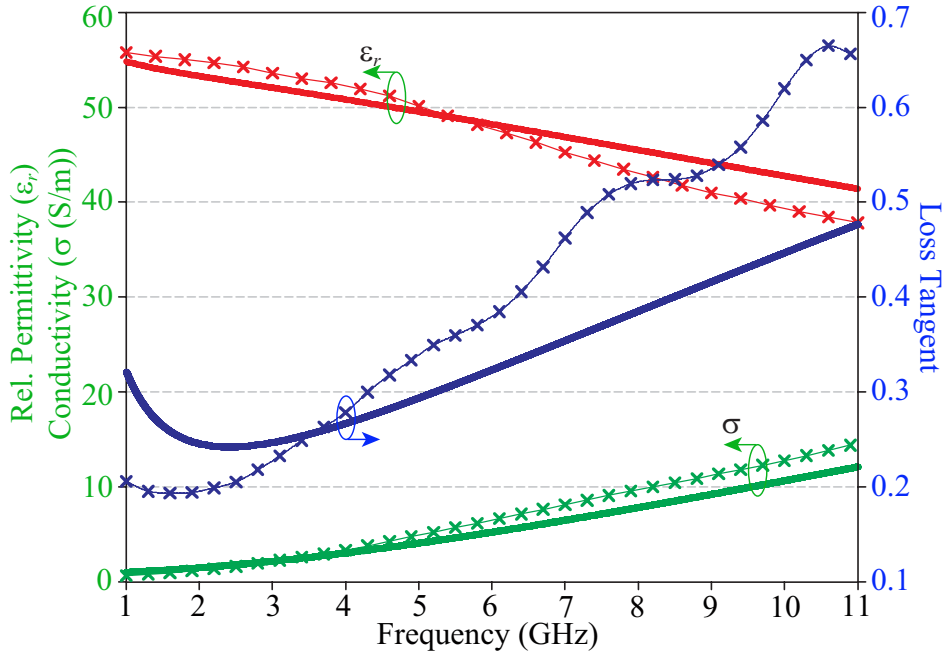


**Figure 3.7:** Electrical properties of the UWB phantoms.

out of plastic, which has a thickness of 1.5 mm and a total volume of 33 L. The solution was left to solidify inside the mannequin and all holes on the mannequin were covered by plastic film to avoid water evaporation. The electrical properties of the UWB phantom measured using the Agilent 85070E Dielectric Probe Kit are given in Fig. 3.7, and mimic quite well the electrical properties of human muscle over a very wide frequency range. These properties are close to the data given in [67]. During the measurement on the flat phantom, the antenna was placed 5 mm above the phantom. This distance emulates the actual placement of the antenna on a human body with clothing. A block of foam was inserted to maintain the gap between the antenna and the flat phantom.

Prior to the measurements, the antenna performance was simulated with both one-layer (homogeneous muscle equivalent) and three-layer (skin-fat-muscle) phantoms (Fig. 3.8(a)) using the tissue properties from [67]. The three-layer phantom represents 1 mm thick skin, 3 mm thick fat, and 46 mm thick muscle, giving a total thickness equal to the flat homogeneous phantom used in the measurements. The width and length of the three-



layer phantom are also equal to those of the homogeneous phantom. We compared the results for the three-layer and homogeneous phantoms and observed that the  $|S_{11}|$  values are nearly identical, and the differences in peak gains are less than 0.4 dB in both bands as can be seen in Fig. 3.8(b). Considering these minor differences as well as the simplicity of the phantom fabrication, the homogeneous phantom was considered adequate for the experimental demonstration.

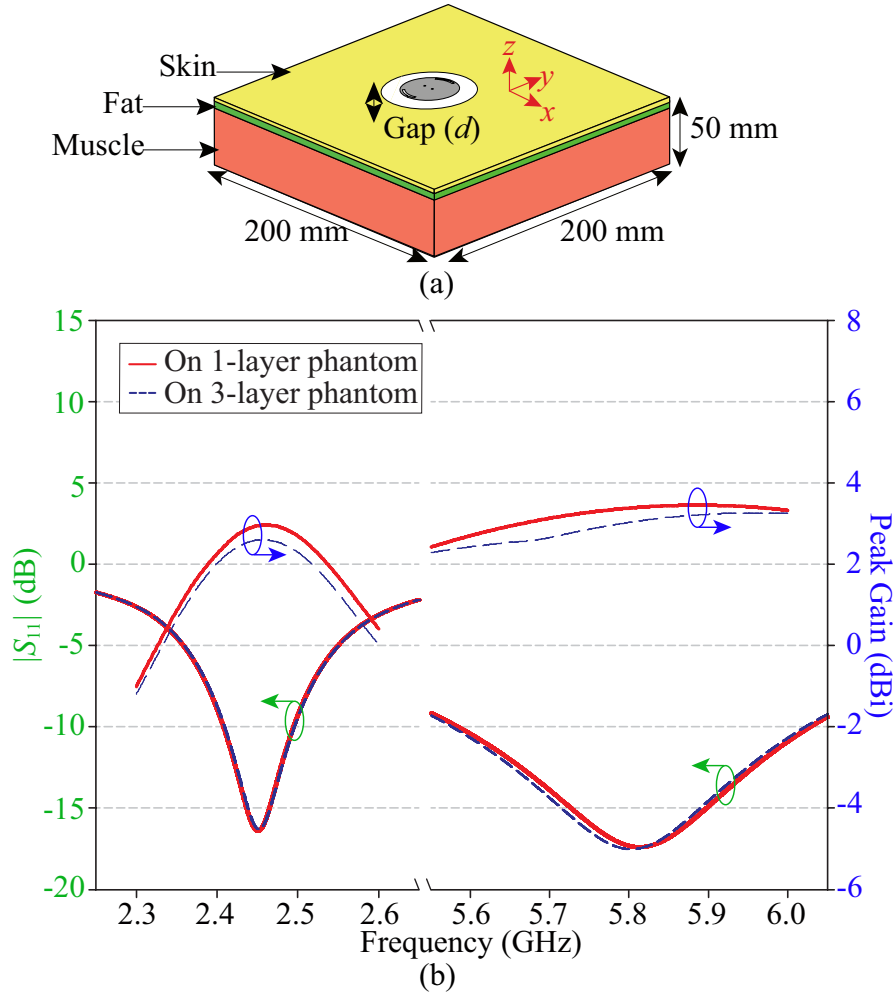


**Figure 3.8:** (a) The proposed antenna on top of the multi-layer phantom. (b) Performance ( $|S_{11}|$  and peak gains) of the antenna when placed 5 mm above the multi-layer and one-layer phantoms.

### 3.3.2 Input Matching

The simulated and measured  $|S_{11}|$  of the proposed antenna when placed in free space and on the flat phantom are shown in Fig. 3.9(a) and are in good agreement. The slight resonance frequency shifts of around 5 MHz in the measured results might be attributed to the tolerances of fabrication (during the manual cutting of the fabrics and inclusion of the shorting pin) and the variations in the material properties of the antenna and fabricated phantom. It can be seen that the reflection coefficients when measured on the phantom are nearly identical to those in free space, which validates the high degree of isolation from the body due to the full ground plane. In free space, the measured 10-dB return-loss bandwidth is 85 MHz (2.409–2.494 GHz) in the first band and 354 MHz (5.59–5.944 GHz) in the second band, while on the phantom it is 87 MHz (2.407–2.494 GHz) in the first band and 339 MHz (5.581–5.92 GHz) in the second band.

The antenna was also tested under several bending conditions to highlight the physical robustness of the proposed method for conformal wearable systems. This was done by wrapping the antenna on the phantom's wrist, having a radius of 28 mm, both along the  $x$ -axis and  $y$ -axis directions, as illustrated in Fig. 3.6(b). The  $|S_{11}|$  performance for each bending configuration is compared with that of the unbent antenna in Fig. 3.9(b). As expected due to the alteration in the electrical length of the antenna, the resonances in the first and second bands are shifted. The same results are also reported in [68]. Despite these variations, the antenna fabricated with PDMS-embedded conductive fabric is more robust against severe deformation. It was observed during the tests that, for the prototype fabricated by simply attaching the conductive fabric to the PDMS surface, there is still a high possibility of conductive-fabric detachment from the substrate, which is attributed to the absence of the encapsulation layer. For comparison, the photograph of the prototypes with and without encapsulation after repetitive bendings (50 times)

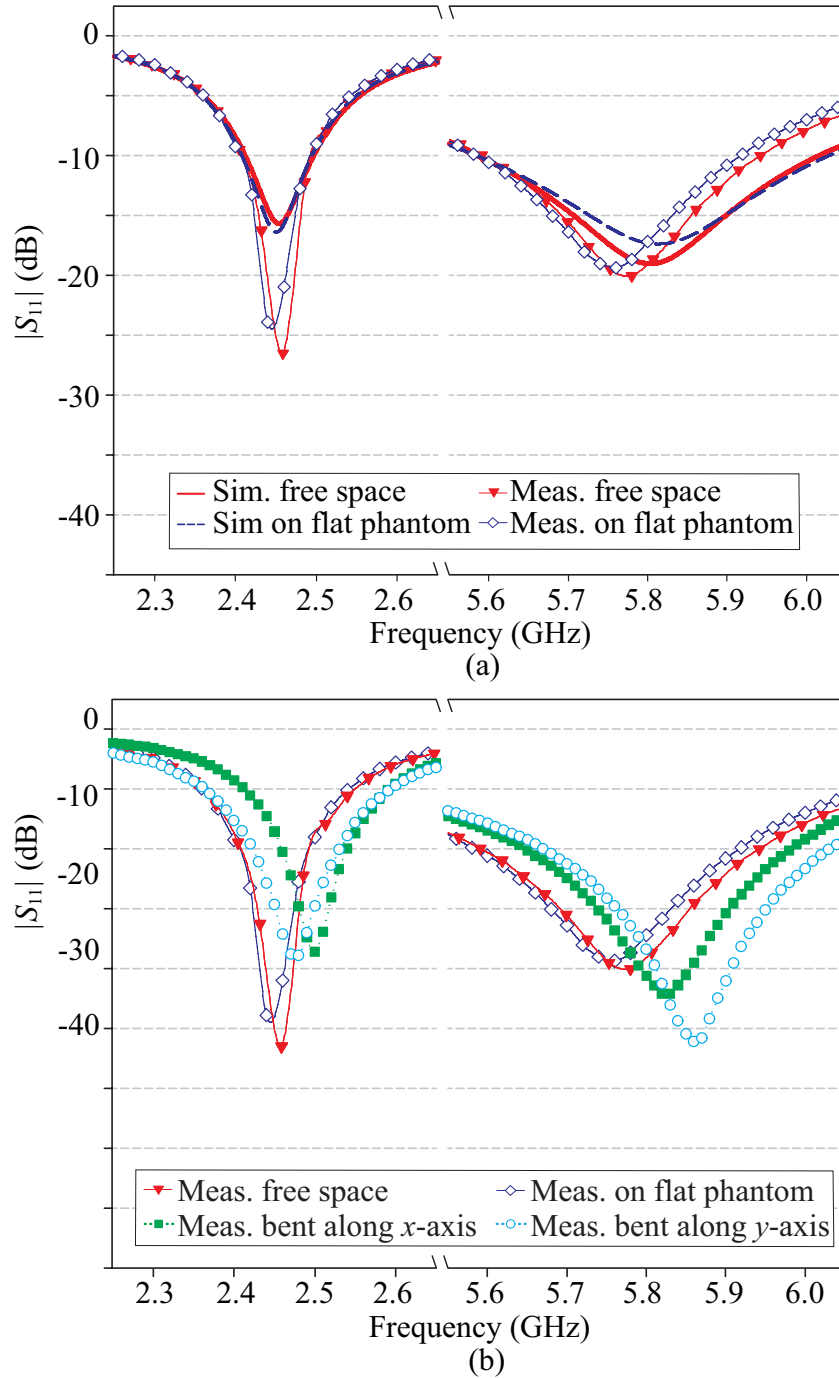


**Figure 3.9:** (a) Simulated and measured  $|S_{11}|$  of the unbent antenna in free space and when placed on the flat phantom. (b) Measured  $|S_{11}|$  of the antenna when bent on the wrist of the human-shaped phantom.

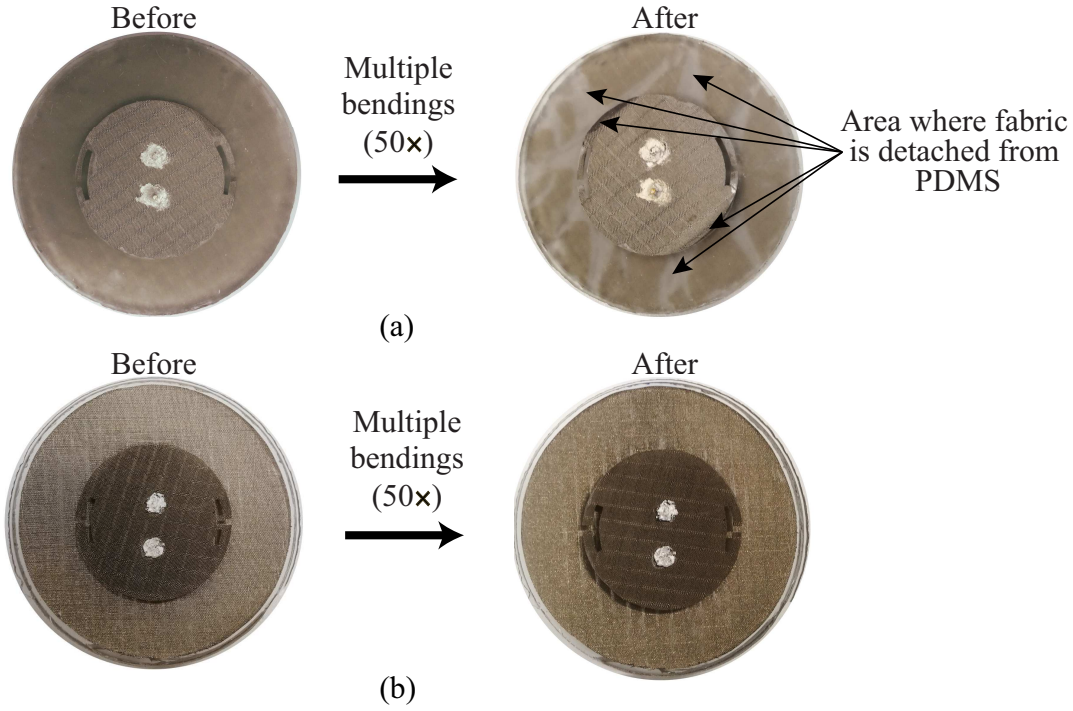


**Figure 3.10:** Photographs of dual-band dual-mode antenna before and after 50 times bendings: (a) Prototype fabricated without encapsulation. (b) Prototype fabricated with encapsulation.

around the phantom's wrist are shown in Figs 3.10(a) and (b). The white marks across the ground plane, that are mainly found in Fig. 3.10(a) after bendings, indicate the zones where the conductive fabric no longer adheres to the PDMS substrate.

### 3.3.3 Dual-Mode Radiation

The measured far-field patterns of the unbent antenna, both with and without the flat phantom, at the resonance frequencies of 2.45 and 5.8 GHz are compared with the simulated patterns in Figs 3.11(a) and (b). The proposed dual-band dual-mode antenna functions with a good agreement between the simulated and measured patterns in both bands, as can be seen clearly in the results. At 2.45 GHz the antenna produces a patch-like radiation which is suitable for off-body communications, while at 5.8 GHz it gives a monopole-like radiation which is desirable for on-body communications.

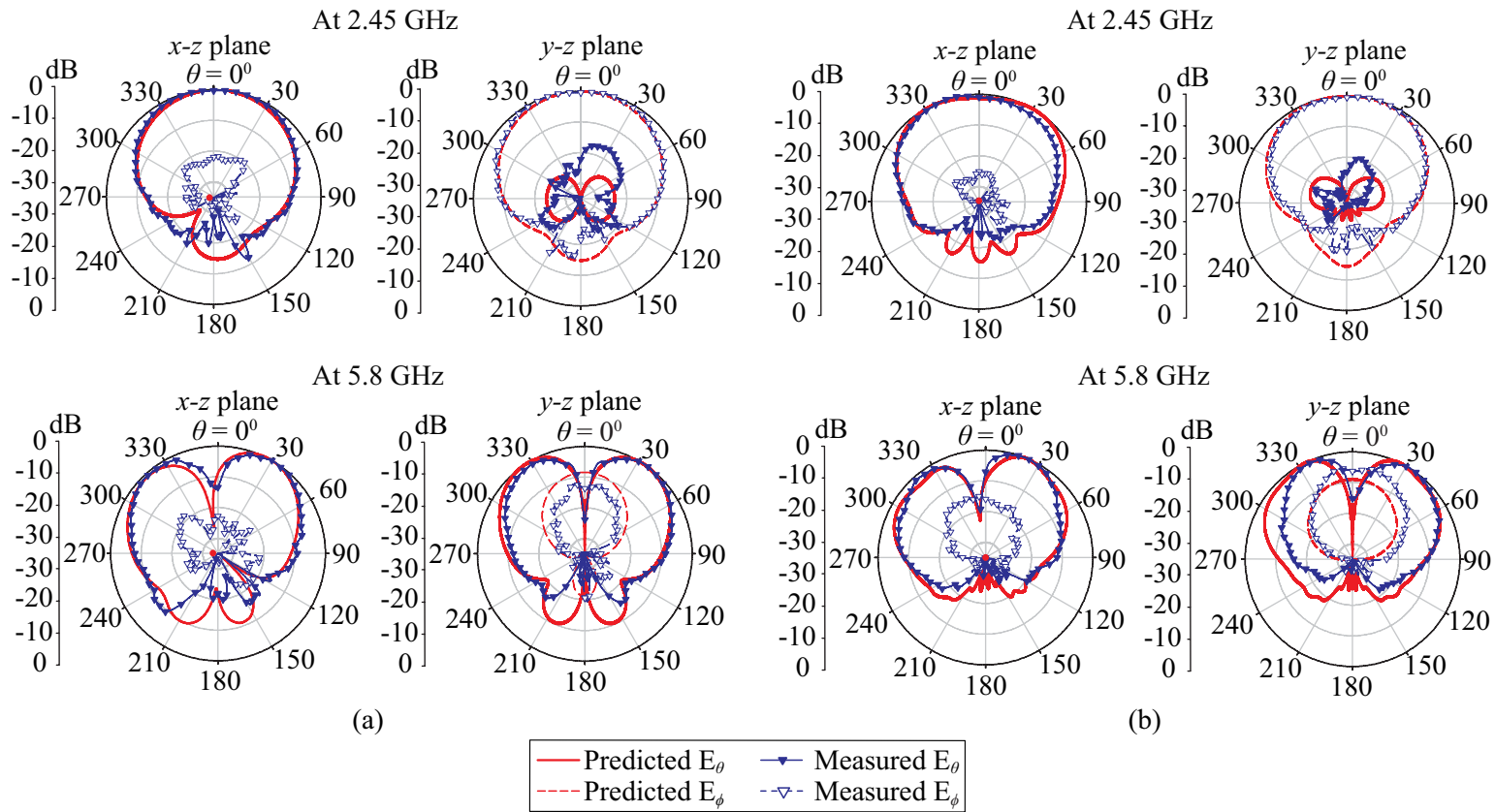


**Figure 3.11:** Normalised simulated and measured radiation patterns at 2.45 and 5.8 GHz. (a) In free space. (b) On the flat phantom.

Compared to Fig. 3.11(a), a considerable decrease in the backward radiation in both bands can be seen in Fig. 3.11(b), due to the presence of the phantom. Thanks to the full ground plane, the antenna is well isolated from the phantom. This is indicated by the peak gains in Fig. 3.12, which are quite stable even when the antenna is placed very close to the phantom. Peak gains of 3.85 and 3.64 dBi, respectively, are achieved in the first and second bands when measured in free space. On the flat phantom, the peak gain decreases slightly to 3.14 dBi for the first band and increases to 4.41 dBi for the second band.

The decrease in the antenna gain in the first band can be understood, as the  $E$ -fields with polarisation parallel to the body ( $TM_{11}$  mode) couple more to the body than the vertically-polarised ones ( $TM_{02}$  mode) [69]. This leads to a higher loss in the first band, which is more significant than the imaginary reflection effect from the phantom. Total efficiencies of up to 41.3% in the first band and up to 45.7% in the second band are obtained from the measurements on the flat phantom. These efficiencies are only 7.2% and 4.9% lower than those in free space, which further confirms the isolation provided by the full ground plane.

The effect of physical deformation to the antenna's dual-mode radiation was also investigated numerically. The antenna was bent around a cylindrical-shaped human-muscle equivalent phantom having a radius of 50 mm and a height of 200 mm, with 5 mm gap maintained between the two. The simulation was done in both bending scenarios, i.e. along the  $x$ -axis and  $y$ -axis directions (see Figs 3.13).

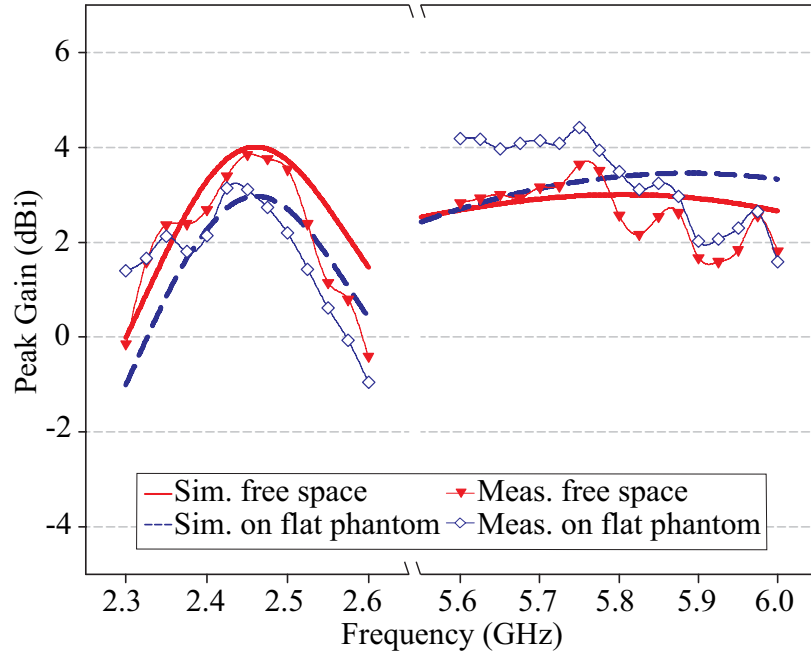


**Figure 3.12:** Simulated and measured peak gains of the antenna in free space and on the flat phantom.

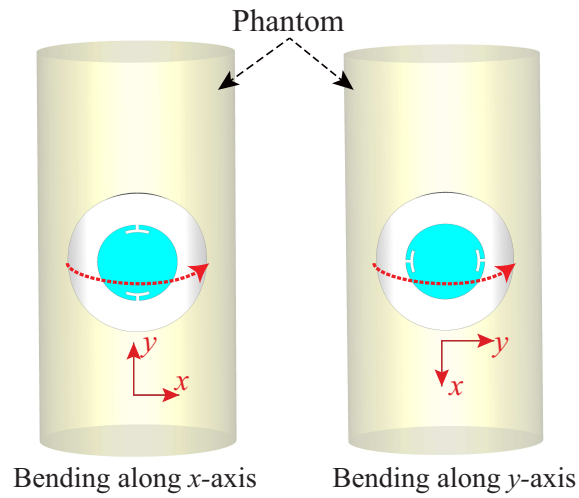


**Figure 3.13:** Illustration of the antenna bending setup on the cylindrical-shaped phantom in simulation.

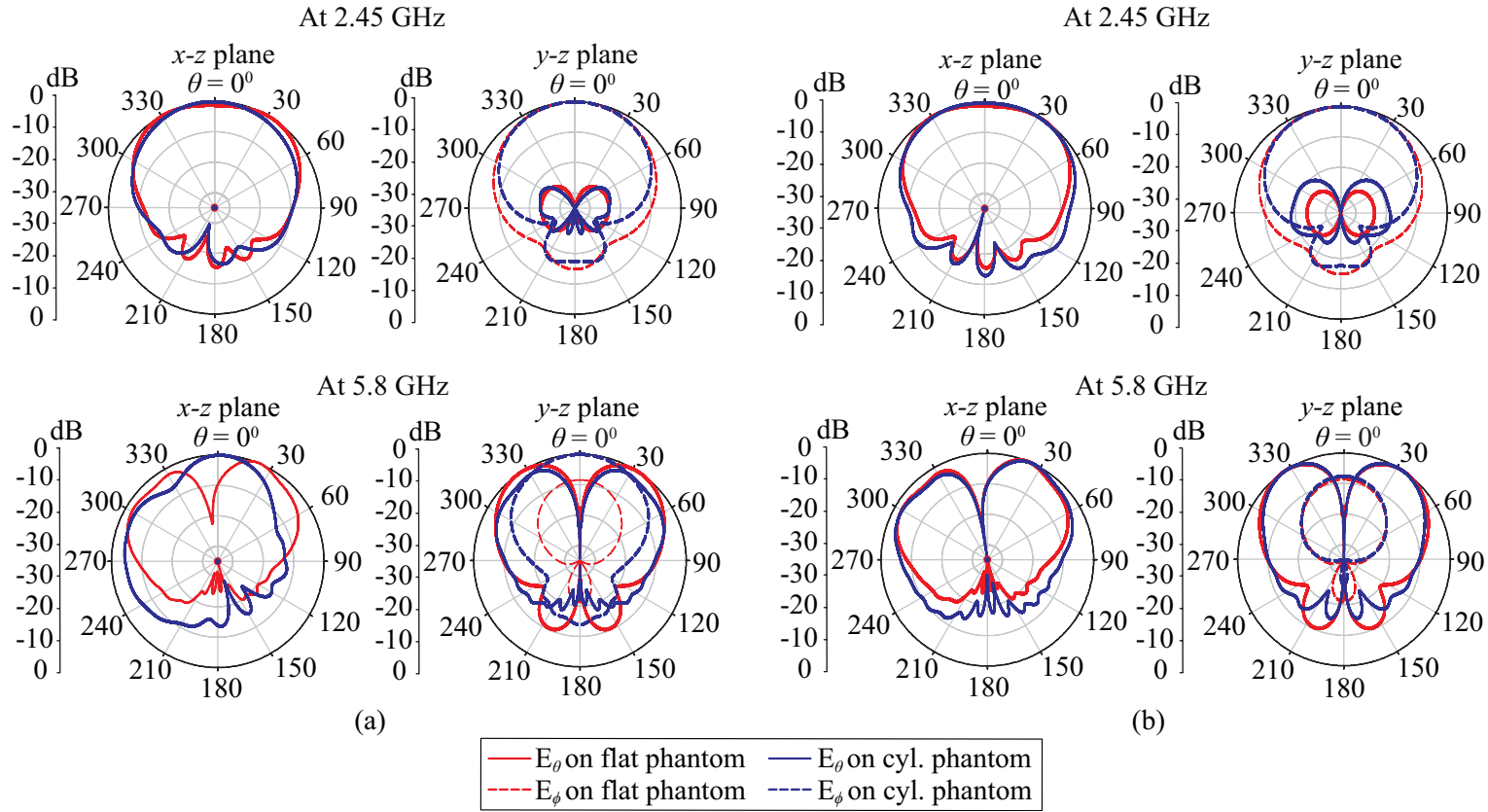


**Figure 3.14:** Normalised simulated on-phantom radiation patterns at 2.45 and 5.8 GHz. (a) Flat vs. bent along the  $x$ -axis. (b) Flat vs. bent along the  $y$ -axis.



As can be seen in Figs 3.14(a) and (b), bending the antenna in either directions has a very small effect to its off-body mode radiation. The maximum radiation of the antenna is still maintained at its boresight direction. The insignificant change is also shown in the on-body mode radiation of the antenna when it is bent along the  $y$ -axis direction. On the other hand, it was found that bending the antenna along the  $x$ -axis affects the on-body mode radiation of the antenna. Fig. 3.14(a) shows that the null position in the bending axial ( $x$ - $z$ ) plane is shifted from the boresight direction, while the  $E_\phi$  component in the  $y$ - $z$  plane increases. This phenomenon might be caused by the change in the position of the shorting pin relative to the feeding point when the antenna is bent along the  $x$ -axis direction, which leads to the change in the higher-order mode current paths. The comparison of the antenna's peak gains when it is placed flatly on the phantom with those when it is bent around the phantom is shown in Fig. 3.15.

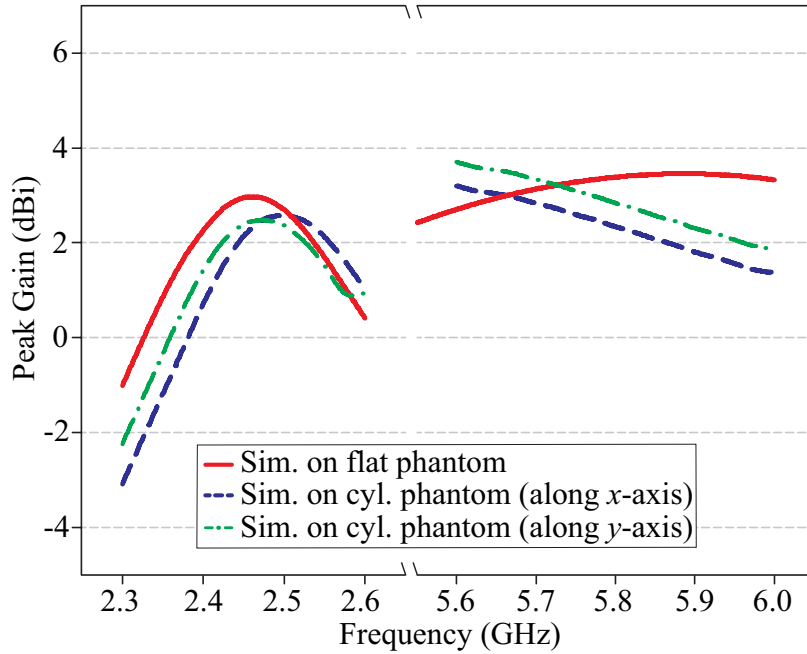


**Figure 3.15:** Simulated peak gains of the antenna when placed on the flat phantom compared to when bent around the cylindrical phantom.

### 3.3.4 SAR

To ensure conformance to the international safety guidelines on human exposure to RF fields, the SAR distribution of the proposed antenna was investigated numerically with CST Microwave Studio 2016 and displayed in Figs 3.16(a) and (b). The antenna is placed 5 mm above the  $200 \text{ mm} \times 200 \text{ mm} \times 50 \text{ mm}$  simplified human muscle phantom which uses the electrical properties obtained from the measurements. The SAR values were calculated based on the IEEE C95.1-2005 standard averaged over 10 g of tissue with the input power of 0.5 W. The simulations show that the maximum 10 g averaged SARs at 2.45 and 5.8 GHz are 0.377 and 0.225 W/kg, respectively, which are far below the safe limit of 2 W/kg [70].

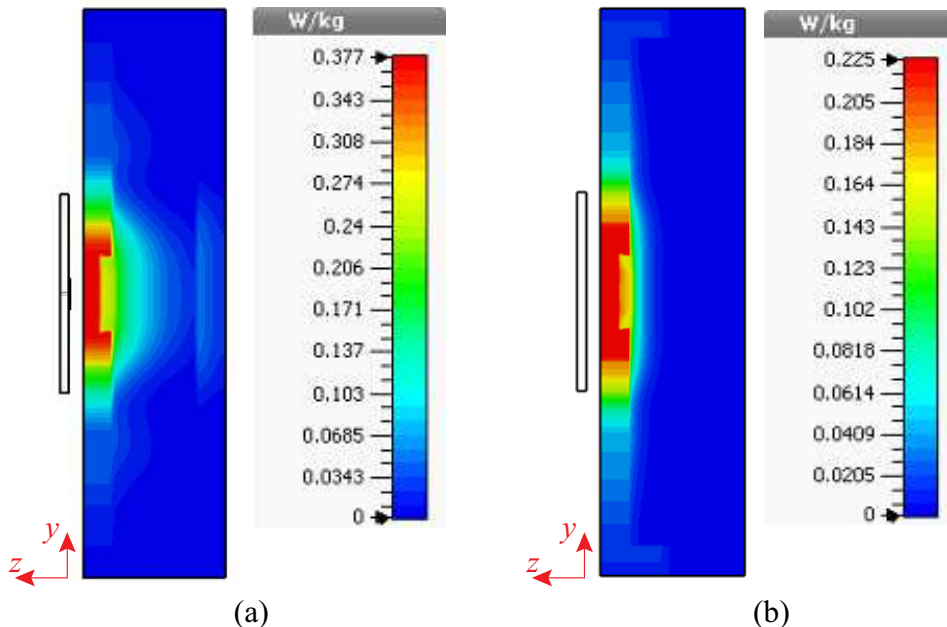


**Figure 3.16:** Computed 10-g averaged SAR distribution of the antenna at (a) 2.45 GHz and (b) 5.8 GHz when operating 5 mm above a human muscle phantom with an input power of 0.5 W.

### 3.4 Summary

In this chapter, a new dual-band dual-mode circular patch antenna suitable for off and on-body communications has been demonstrated. As compared to the previously reported dual-band dual-mode wearable antennas, the design is much simpler using only a single circular patch fed by a simple probe feed. Instead of using two different radiators, the off- and on-body modes are achieved by utilising the inherently generated  $TM_{11}$  and  $TM_{02}$  modes of the circular patch. To tune the resonance of both modes to the desired frequencies of 2.45 and 5.8 GHz, respectively, reactive loading techniques, i.e. a shorting pin and arc-shaped slots, are used. Beside simplicity, this proposed approach allows a full ground plane to be maintained on the opposite side of the patch, providing a high degree of isolation from the lossy human body tissue. Furthermore, unlike the previous designs that were made of conventional rigid materials, this antenna was fabricated using the proposed PDMS-embedded conductive fabric, which provides the flexibility and physical robustness required by wearable applications.

A range of experimental investigations of the antenna performance has been carried out in free space and on semisolid human-muscle equivalent phantoms. A promising antenna performance against the human-body loading effect and physical deformation is observed, validating not only the proposed antenna design but also the applicability of the proposed fabrication approach. When placed on the flat phantom, measured bandwidths of 87 and 339 MHz in the 2.45 and 5.8 GHz bands, respectively, are achieved with the corresponding peak gains of 3.14 and 4.41 dBi, which are quite close to the performance in free space. For an input power of 0.5 W, the SAR levels in the underlying tissues were found to be less than 2 W/kg in both bands, implying conformance with international safety guidelines.



---

# UWB Wearable Antenna with Full Ground Plane based on PDMS-Embedded Conductive Fabric

## 4.1 Introduction and State of the Art

UWB technology is recently emerging as an attractive solution for several short-range wireless applications, including wireless body-centric networks. Indeed, UWB communications exhibit major advantages as compared to conventional (narrow-band) technologies, including low-power implementations, high-data-rate transmission capabilities, and robustness against multi-path [71]. Along these lines, several research efforts have focused on developing flexible and planar UWB antennas for wearable applications [30, 72–82]. Flexible materials used for the aforementioned purpose include textiles, liquid metal, paper, copper foil, conductive threads, and polymers.

A common characteristic of most of the previously reported flexible planar UWB antennas is the lack of a full ground plane on the back of the radiator. Instead, par-

tial/modified ground planes or coplanar waveguide topologies are generally preferred (see Figs 4.1(a)–(d)), as they allow for easy bandwidth enhancement . However, such designs are highly undesirable for wearable applications mainly for the following reasons. Firstly, the lack of a full-ground plane implies that the high-permittivity and lossy biological tissues will significantly load the antenna, affecting, in turn, its performance. Secondly, those antenna designs are associated with back radiation (i.e., radiation in their lower hemisphere), which, in turn, unavoidably increases the SAR inside the human body. To mitigate the aforementioned problems, complex UWB antenna designs equipped with a full ground plane have recently been reported [79,80]. Although flexible, these prototypes were textile-based, and thus highly sensitive to wetness, heat, and extreme deformations. Consequently, they are unsuitable for harsh operating conditions, such as those encountered in wearable applications.

In this chapter, a new planar UWB antenna design with suppressed backside radiation, suitable for wearable applications in the 3.7 to 10.3 GHz band, is presented. Notably, the antenna is fabricated via PDMS-embedded conductive-fabric technology, which enables conformality, flexibility, easy realisation, robustness, water resistance, thermal and chemical stability. Thus, this design becomes the first-ever flexible and physically robust body-worn UWB antenna with a full ground plane.

The rest of the chapter is organised as follows. Section 4.2 presents the UWB antenna design. Section 4.3 discusses the simulated versus measured antenna performance, which includes an analysis of the antenna performance with respect to human-body proximity as well as structural deformations using the fabricated UWB phantoms. In addition to the antenna SAR analysis, its time-domain performance is also discussed in Section 4.3. Finally, a summary of the work is drawn in Section 4.4.

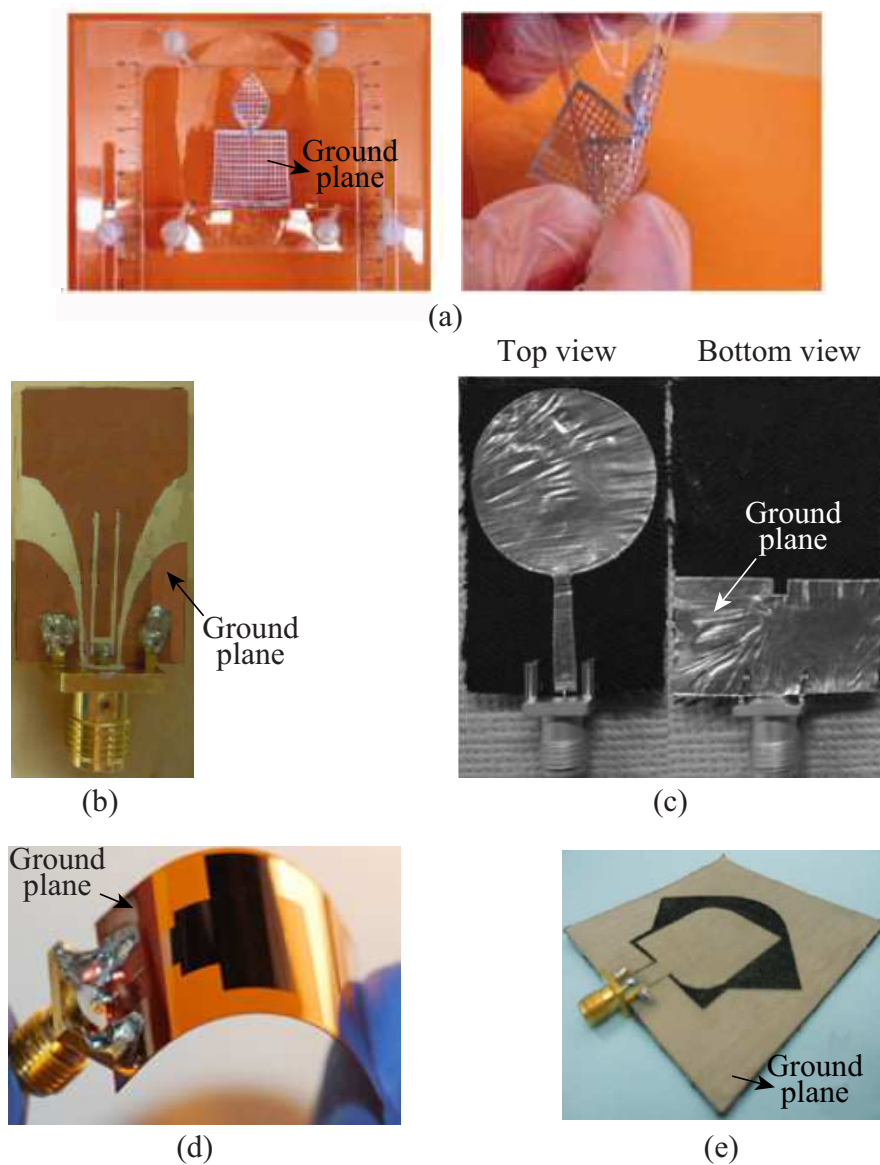


**Figure 4.1:** Some examples of previously reported flexible planar UWB antennas. (a) [30]. (b) [75]. (c) [76]. (d) [77]. (e) [78].

## 4.2 UWB Antenna Topology and Prototype

As seen in Fig. 4.2, the proposed antenna design is based on a simple microstrip patch technology. Two modified arc-shaped patches operating as the main radiator are placed on top of a PDMS substrate. On the opposite side of the substrate, a full ground plane is preserved. For the same reasons described during the dual-band dual-mode antenna fabrication in Chapter 3, CF I was utilised for realisation of the patch layer, while CF III was used for the ground layer. The entire structure is further encapsulated into PDMS.

As is well known, a conventional thin patch antenna with a full ground plane is inherently narrowband. Thus, to achieve an ultra-wide bandwidth, several bandwidth enhancement techniques, including the use of multiple resonators and slots [83], were applied. Specifically, as seen in Fig. 4.2, two arc-shaped patches, operating in the higher and lower bands of the desired Federal Communications Commission (FCC) UWB range, were employed. Each patch was fed by two small transmission lines connected to a coaxial probe on the opposite side of the substrate. To further improve the matching at lower frequen-

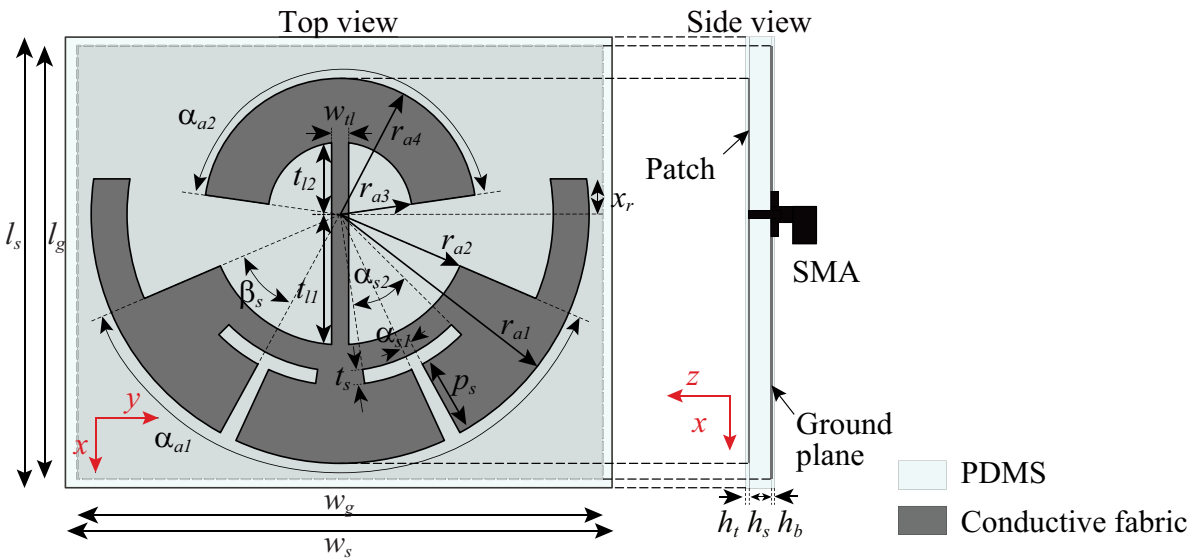


**Figure 4.2:** Detailed geometry of the proposed UWB antenna.



cies, two identical T-shaped slots having a length of approximately less than a quarter of the effective wavelength at the lowest target operation frequency (3.1 GHz) were added. An optimisation process was further pursued in CST Microwave Studio 2016 to get the final antenna dimensions listed in Table 4.1.

The effects of some critical parameters to the UWB behaviour of the antenna, including the size of both arc-shaped patches, the position of the T-shaped slots, and the length of feeding lines are shown in Figs 4.3(a)–(c) and 4.4(a)–(c), which were obtained through simulations by maintaining all other parameters constant. As can be seen, changes of dimensions in the big arc-shaped patch including the two T-shaped slots (e.g.  $r_{a1}$ ,  $\alpha_{a1}$ ,

**Table 4.1:** Dimensions of the Proposed UWB Antenna

Parameter	Dimension	Parameter	Dimension (mm)
$\alpha_{a1}$	134°	$\beta_s$	38°
$\alpha_{a2}$	164°	$p_s$	11 mm
$r_{a1}$	35.1 mm	$t_s$	2 mm
$r_{a2}$	18.4 mm	$w_g$	74 mm
$r_{a3}$	10.2 mm	$l_g$	61 mm
$r_{a4}$	19.2 mm	$w_s$	80 mm
$t_{l1}$	18.3 mm	$l_s$	67 mm
$t_{l2}$	10.2 mm	$h_t$	0.2 mm
$w_{tl}$	2.4 mm	$h_s$	3 mm
$\alpha_{s1}$	4°	$h_b$	0.2 mm
$\alpha_{s2}$	38°	$x_r$	5 mm

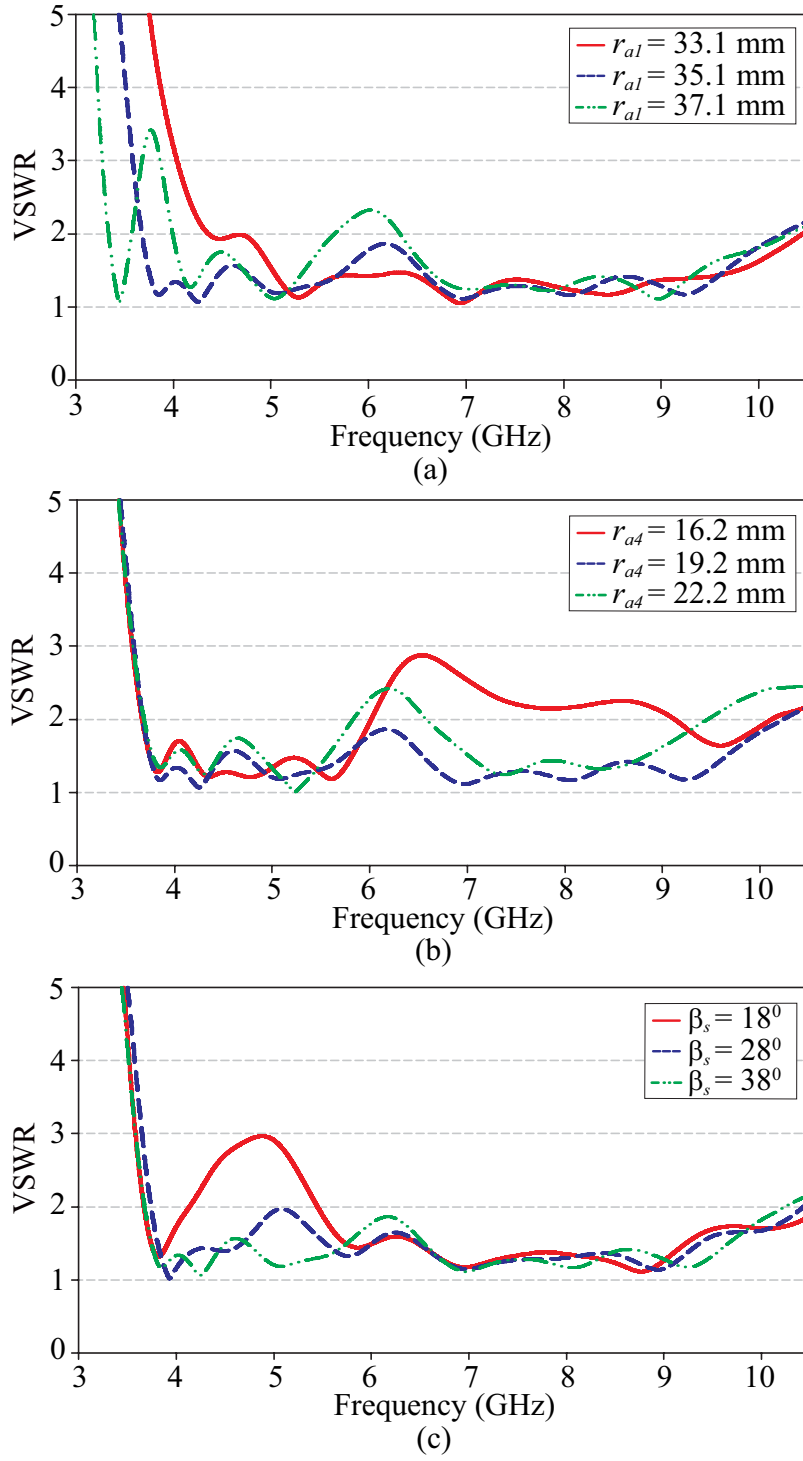


**Figure 4.3:** Simulated VSWR with varying (a) radius of big arc-shaped patch ( $r_{a1}$ ), (b) radius of small arc-shaped patch ( $r_{a4}$ ), and (c) position of T-shaped slot ( $\beta_s$ ).

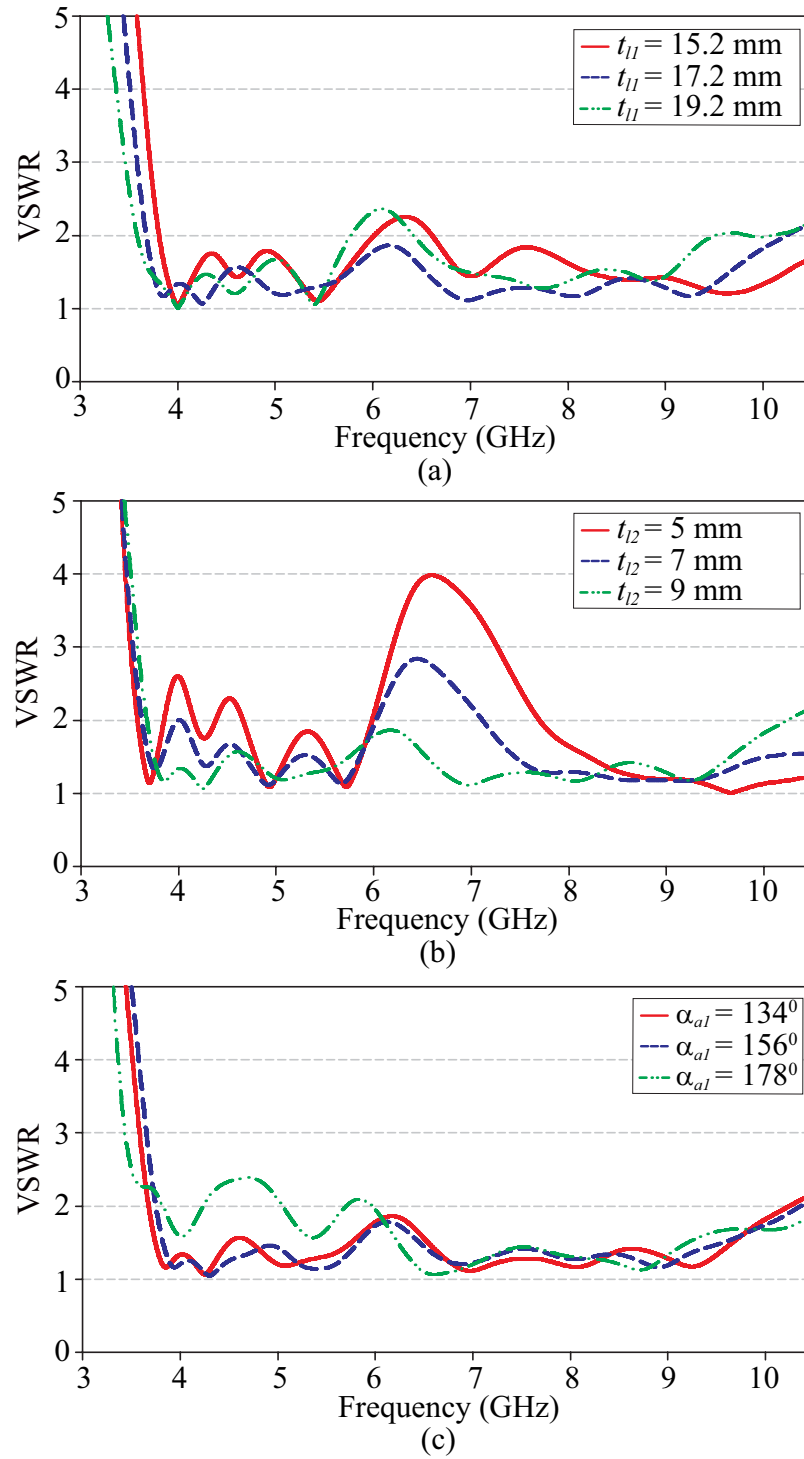


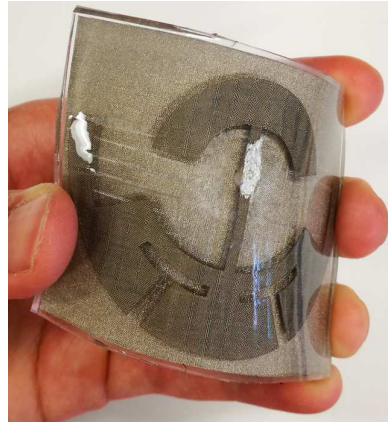
**Figure 4.4:** Simulated VSWR with varying (a) length of feeding line of big arc-shaped patch ( $t_{l1}$ ), (b) length of feeding line of small arc-shaped patch ( $t_{l2}$ ), (c) curvature angle of big arc-shaped patch ( $\alpha_{al}$ ).

and  $\beta_s$ ) affect the impedance matching in the lower bands, whereas changing the dimensions of the small arc-shaped patch (e.g.  $r_{a4}$ ) affects the impedance matching in higher bands. On the other hand, tuning the lengths of the microstrip feeding lines ( $t_{l1}$  and  $t_{l2}$ ) was found to be critical to the antenna impedance matching in the middle bands.

Antenna prototyping was performed through the bottom-top multilayer fabrication process described in Section 2.2.2. To ensure fabrication accuracy, three rectangular ring-shaped moulds were used, whose thickness and dimensions matched those of the optimised antenna design. Laser cutting was used for patterning of the radiating patch, to obtain an accurate dimension of the patch layer. For ease of measurements (particularly in the case of on-phantom testing), a small 90° bent SMA connector was utilised at the antenna feeding point. Fig. 4.5 shows the fabricated UWB antenna prototype.



Top view



Bent view

**Figure 4.5:** Photographs of the fabricated UWB antenna.

## 4.3 UWB Antenna Performance

The performance of the antenna was studied in free space and near-body environments. The latter was done by using both the UWB semisolid phantoms prepared in Section 2.3.1, where the antenna was placed 5 mm above each phantom using a small block foam.

### 4.3.1 Voltage Standing Wave Ratio (VSWR)

The measured free-space and on-phantom VSWR results, obtained through the measurements with the Agilent PNA-X N5242A network analyser, are compared with the simulated results in Fig. 4.6(a). Remarkably, the VSWR performance is almost identical in free space and when the antenna is placed upon the flat phantom, which signifies that the presence of the full ground plane isolates the antenna from the lossy tissue. As such, good impedance matching can be maintained by the antenna when placed upon the human body. Slight discrepancies, however, are observed in the measured results, which are most likely due to fabrication errors such as SMA connector positioning and burnt fabric edges following the laser cutting (see Fig. 4.7). The latter resulted in minor dimension changes in some parts of the antenna, which affect the antenna input impedance, as was observed during the antenna optimisations.

The effect of antenna deformation upon the VSWR was also investigated. To do this, the antenna prototype was bent around the head and wrist of the human-shaped phantom shown in Figs 4.8(b) and (c) (across both the  $x$ -axis and the  $y$ -axis). The VSWR performance for the bent antenna setups as compared to the unbent antenna placed upon the flat phantom is shown in Fig. 4.6(b). As seen, a stable VSWR is maintained, verifying the robustness of the proposed antenna against physical deformation. Even more importantly, the antenna returned to its original shape after bending, and the conductive fabrics remained intact inside the PDMS encapsulation. The latter is attributed to the PDMS-PDMS bonding formed through the pores of the fabric.

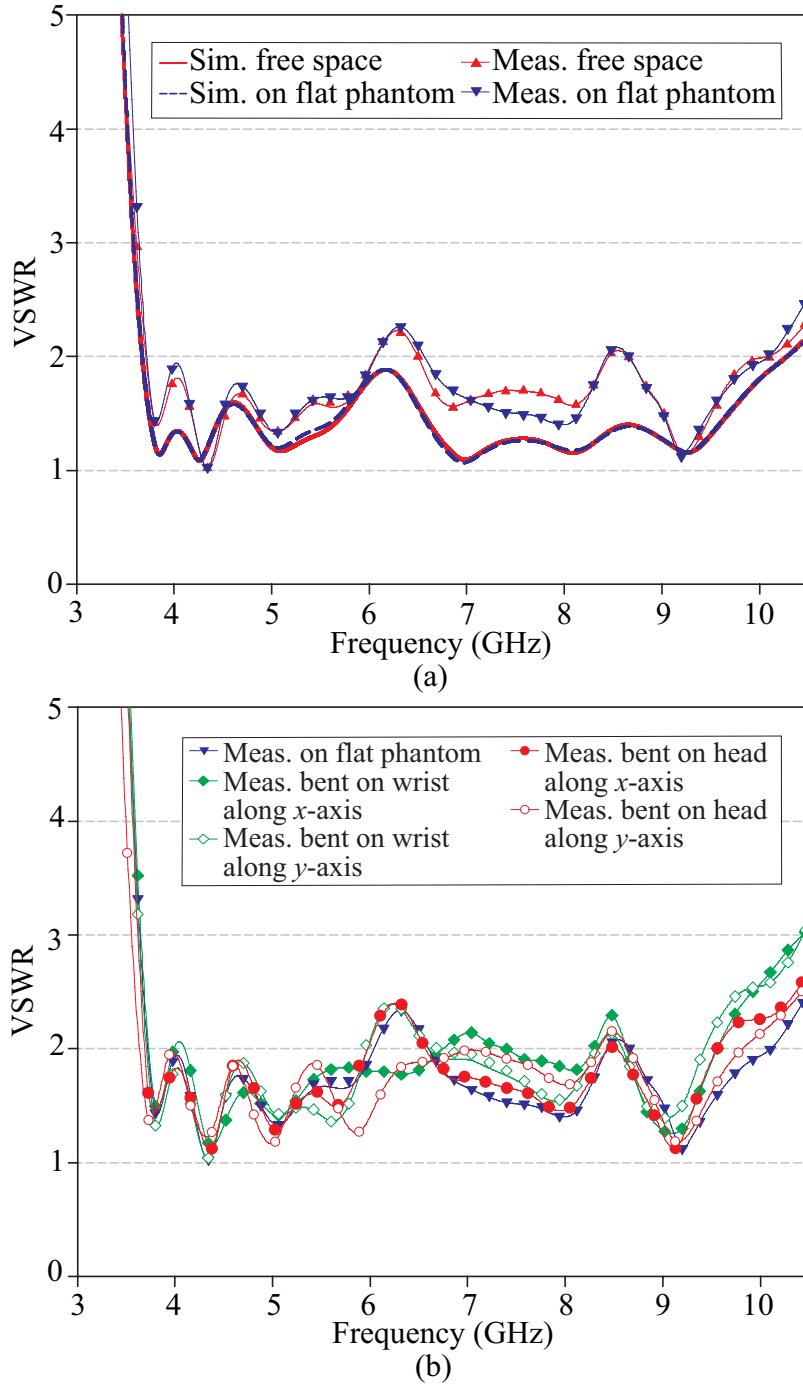


**Figure 4.6:** (a) Simulated and measured VSWR of the unbent antenna in free space and when placed on the flat UWB phantom. (b) Measured VSWR of the antenna when bent on the head and wrist of the human-shaped UWB phantom.

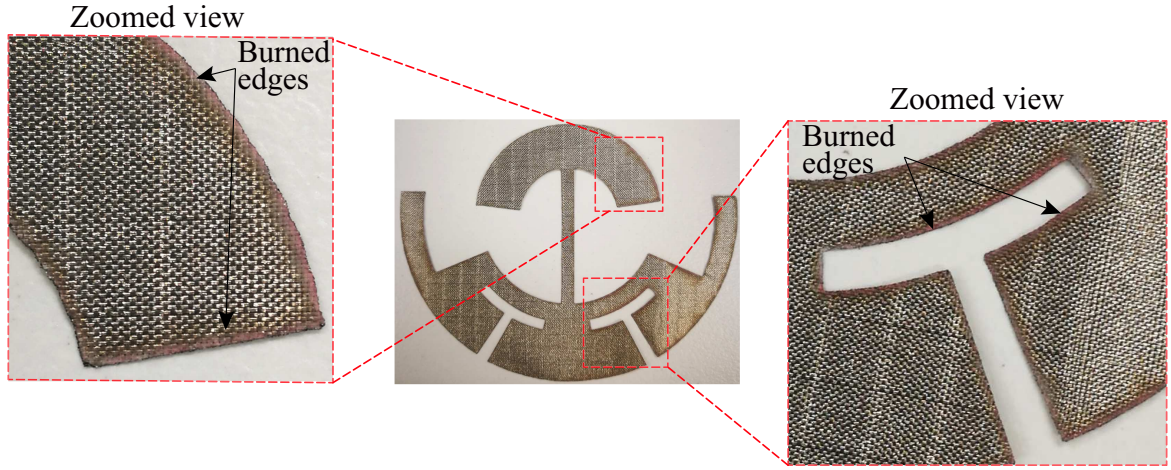


**Figure 4.7:** Photograph of the fabric patch layer obtained through laser cutting.

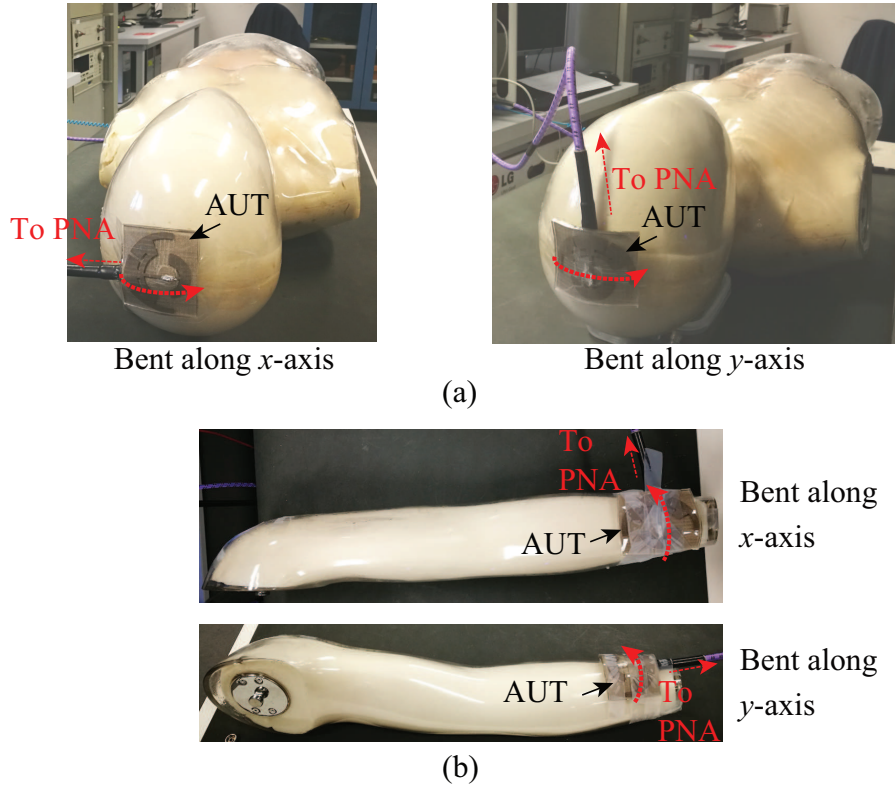


**Figure 4.8:** On-phantom VSWR measurement setup. (a) The antenna wrapped on the head of the human-shaped phantom. (b) The antenna wrapped around the wrist of the human-shaped phantom.

### 4.3.2 Far-Field Characteristics

The antenna far-field performance was measured in the NSI700S-50 spherical near-field antenna range at the AusAMF, Marsfield, and the results are shown in Fig. 4.9. Two scenarios were considered, viz. antenna in free space (Fig. 4.9(a)), and antenna placed upon the flat phantom (Fig. 4.9(b)). In general, a good agreement is achieved between measured and simulated results. As expected, due to the full ground plane, the antenna radiates mainly towards its boresight direction. In turn, this minimises antenna-body coupling and energy dissipation inside the body.

Notably, this mode of directional radiation is maintained even at higher frequencies. When the antenna is placed upon the flat phantom, the patterns are similar to those in free space. Expectedly, even lower back radiation is observed as attributed to the reflection from the phantom. Fig. 4.10 shows the measured peak gains and efficiencies of the antenna, which are again in good agreement with the corresponding simulated results. From the measurements, the total radiation efficiencies of the antenna are slightly reduced when mounted on the phantom, but thanks to the full ground plane, the difference is less than 5.7% as compared to the free-space scenario. It is also worth noting that the peak gains, particularly at higher frequencies (i.e. above 6.2 GHz), increase when the antenna is in close proximity to the phantom. This is attributed to reflections from the phantom [79, 84].



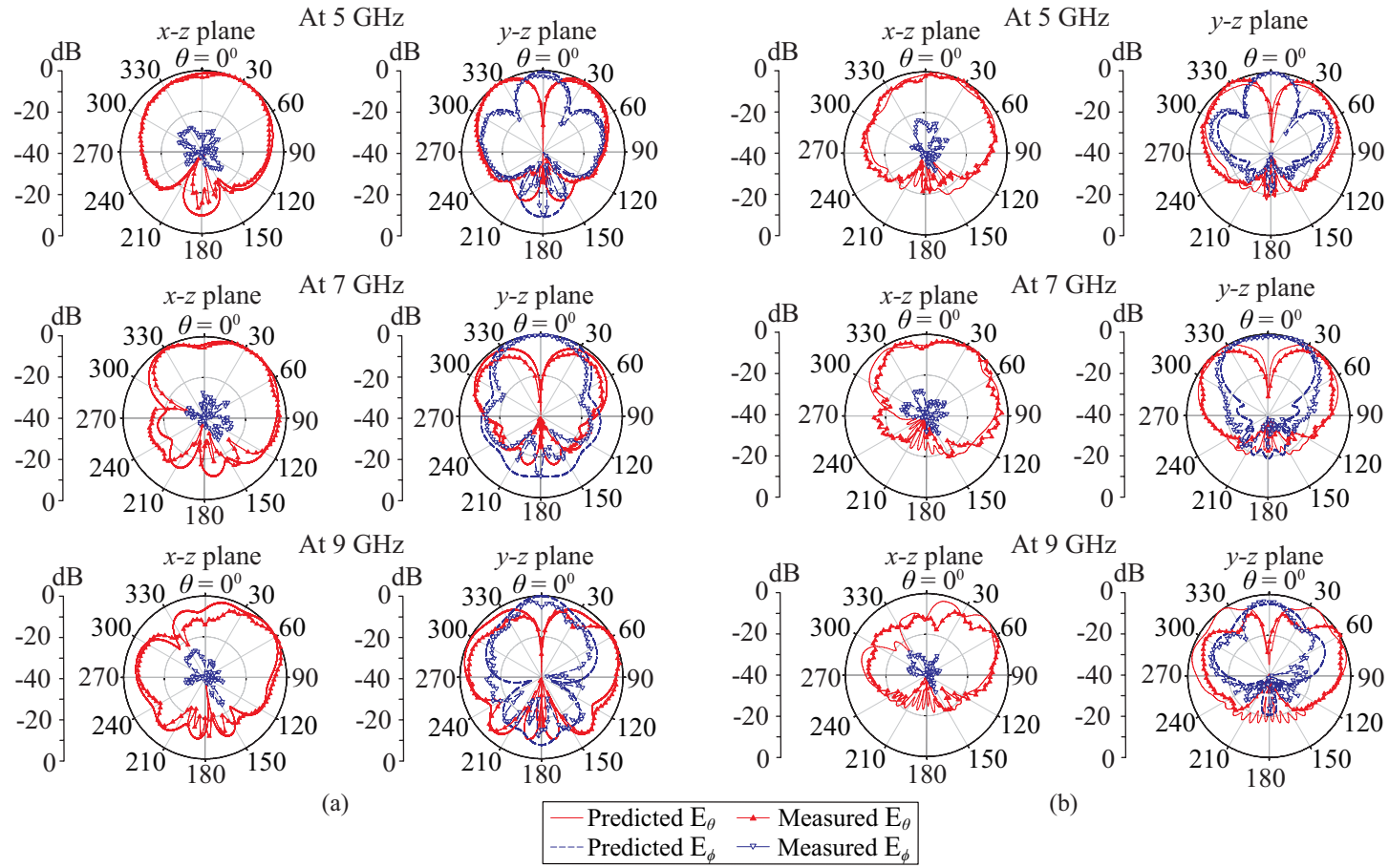


**Figure 4.9:** Normalised radiation patterns of the antenna at 5, 7, and 9 GHz. (a) In free space. (b) On the flat phantom.

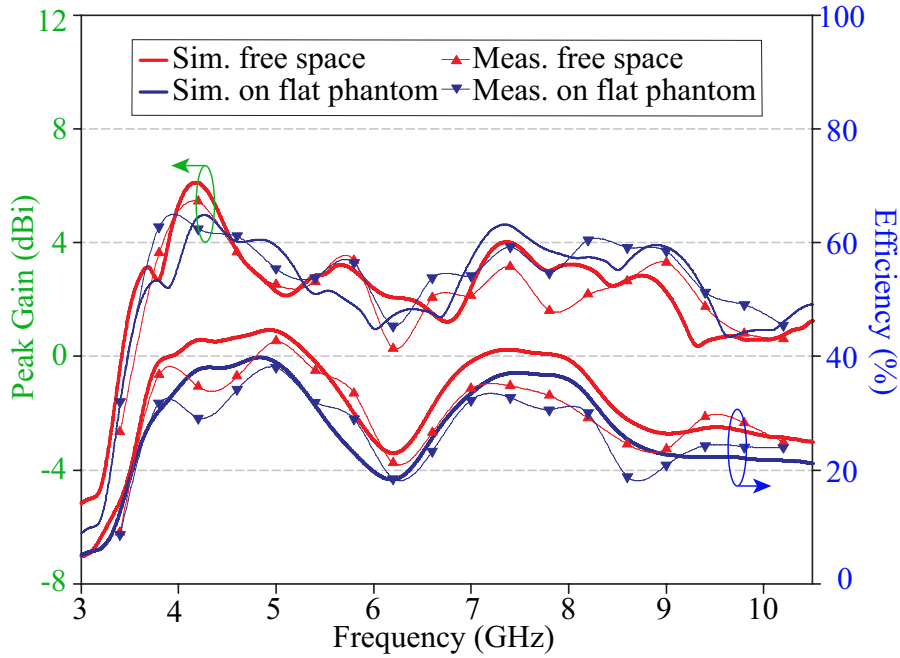


**Figure 4.10:** Simulated and measured peak gains and total efficiencies of the antenna when in free space and on the flat phantom

The radiation performance of the antenna under deformation was also investigated numerically. In simulation, the antenna was bent around a cylindrical-shaped human-muscle equivalent phantom having a radius of 30 mm and a height of 200 mm. Considering the stable VSWR shown in Fig. 4.6(b), only the bending scenario across the  $y$ -axis, was investigated. A 5 mm gap was maintained between the antenna and phantom. As can be seen in Figs 4.11(a) and (b), the simulated radiation patterns of the antenna are quite similar to those when the antenna was placed unbent above the flat phantom. The same thing is also observed in the antenna's peak gains and total efficiencies as shown in Fig. 4.12, which validates further the robustness of the proposed design against physical deformation.

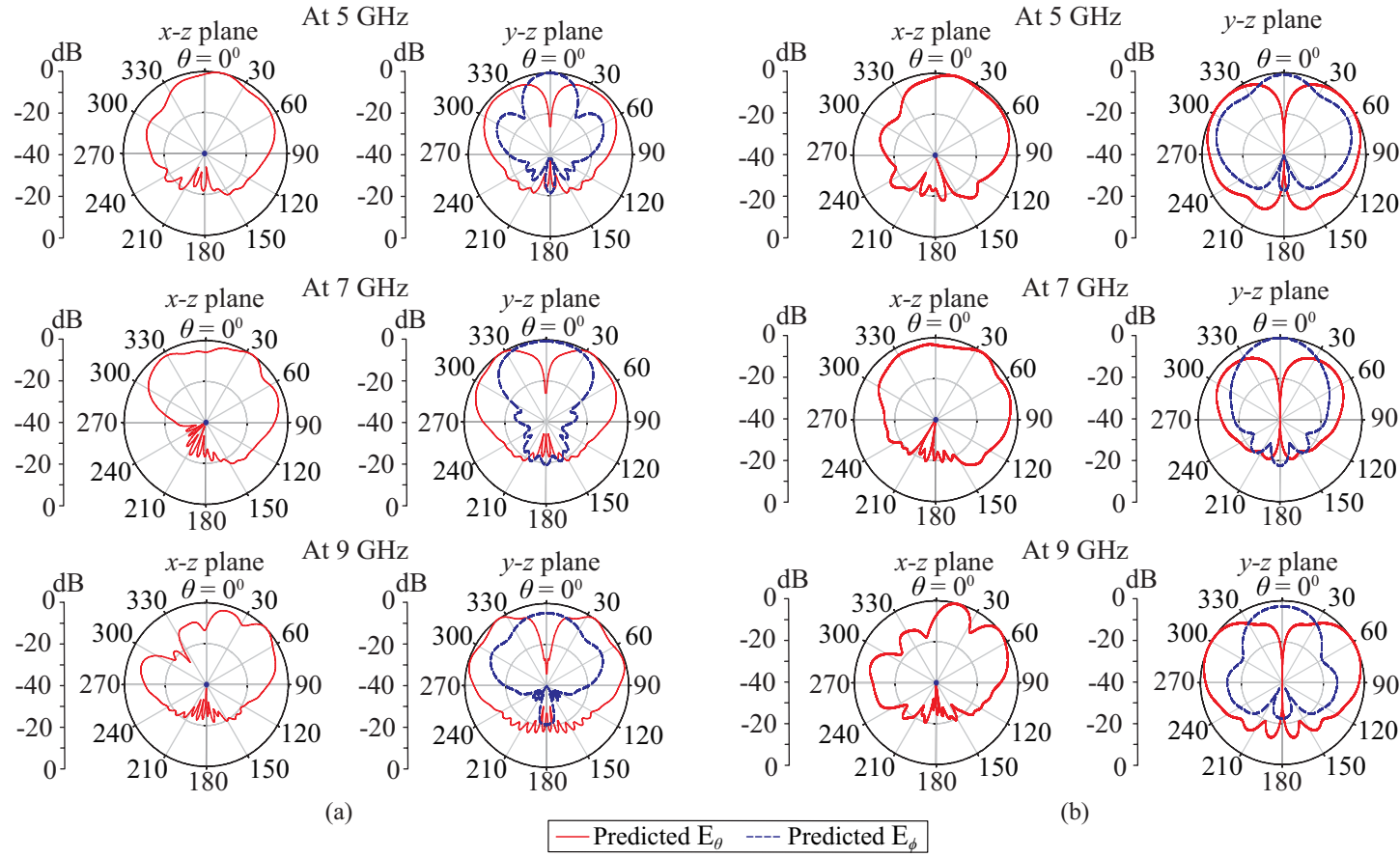


**Figure 4.11:** Normalised simulated radiation patterns of the antenna at 5, 7, and 9 GHz. (a) On the flat phantom. (b) Bent around the cylindrical phantom.

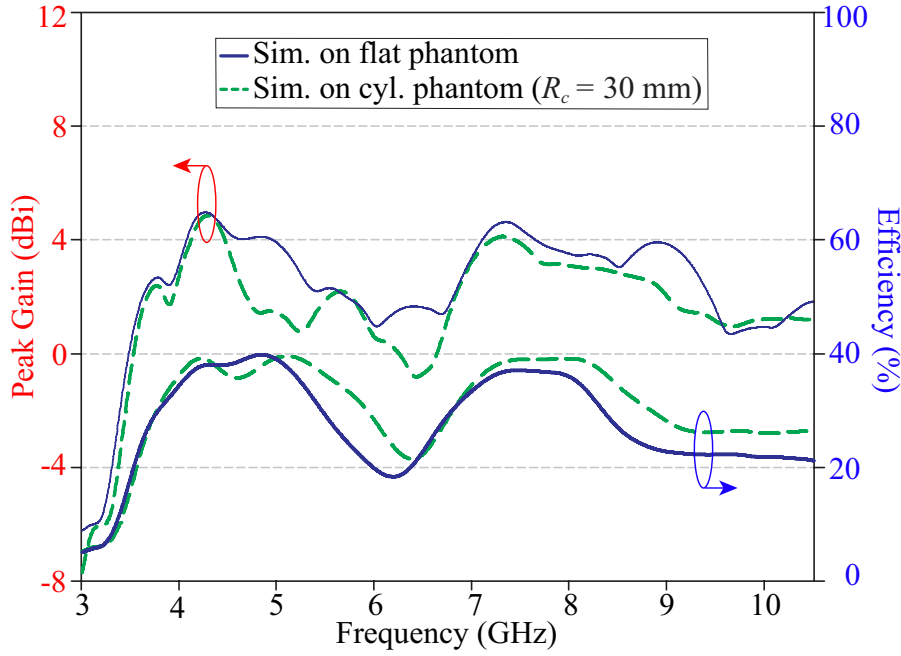


**Figure 4.12:** Simulated peak gains and total efficiencies of the antenna when placed on the flat phantom and bent around the cylindrical phantom

### 4.3.3 SAR

The impact of the antenna to the underlying human body tissues was investigated in CST Microwave Studio 2016. Two scenarios were considered. First, the antenna was placed 5 mm above the same human-muscle phantom used in the previous chapter. Second, the antenna was simulated 5 mm above the cylindrical phantom used in previous section. The SAR distributions were calculated based on the IEEE C95.1-2005 standard averaged over 10 g of tissue, assuming an input power of 0.5 W. Thanks to the isolation provided by the ground plane, the peak SAR results of the first case at 5, 7, and 9 GHz were found to be equal to 0.147, 0.174, and 0.09 W/kg, respectively, whereas in the second case the results were equal to 0.124, 0.259, and 0.117 W/kg, respectively (see Figs 4.13(a) and (b)). The results conform to the SAR requirement of lower than 2 W/kg [70], which further highlights the superiority of the proposed antenna for on-body applications.

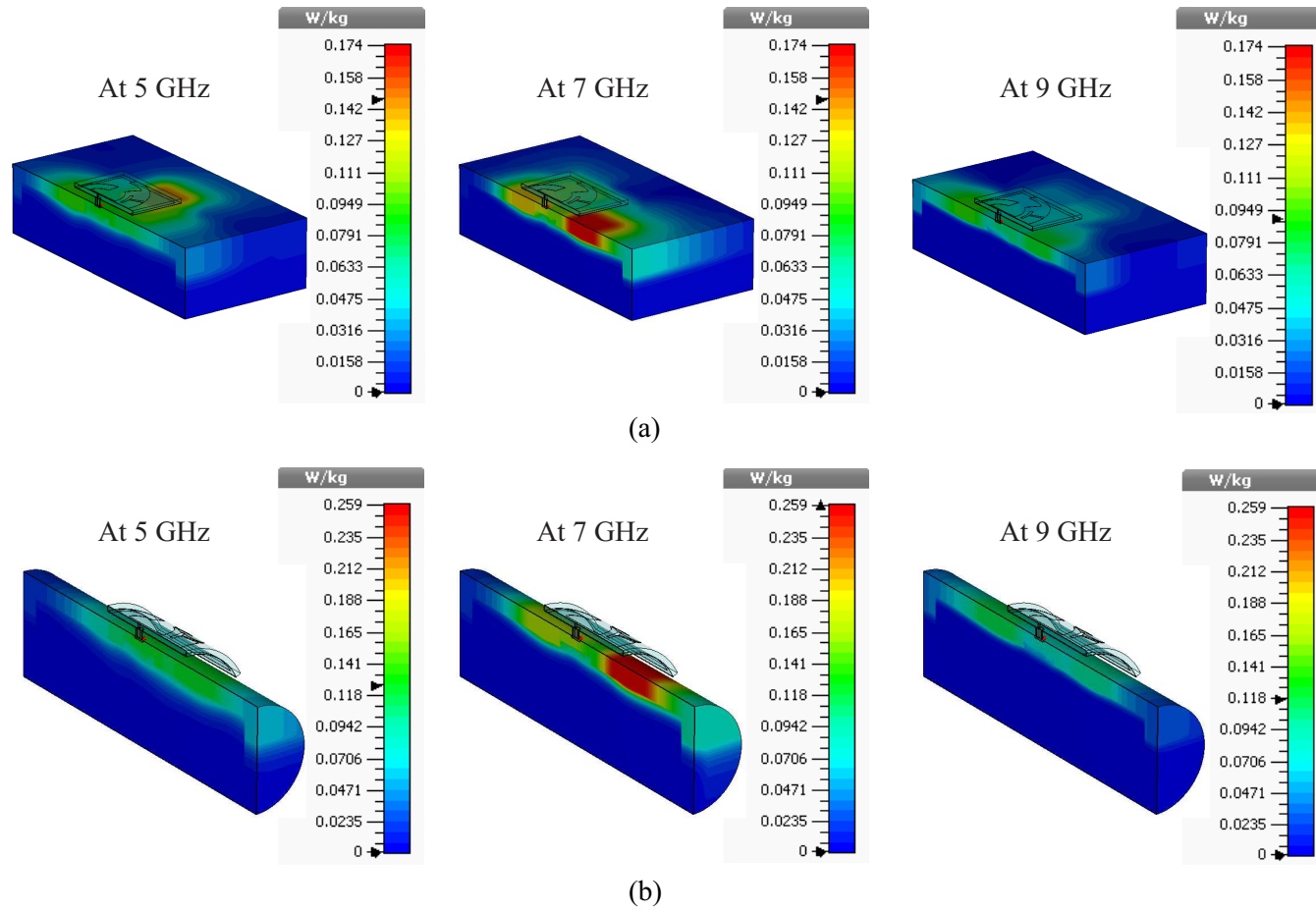


**Figure 4.13:** Simulated 10-g averaged SAR distribution of the antenna at 5, 7, and 9 GHz. (a) On the flat phantom. (b) On the cylindrical phantom. The input power of the antenna is 0.5 W and the distance between the antenna and the phantom is maintained 5 mm.

#### 4.3.4 Time-Domain Performance

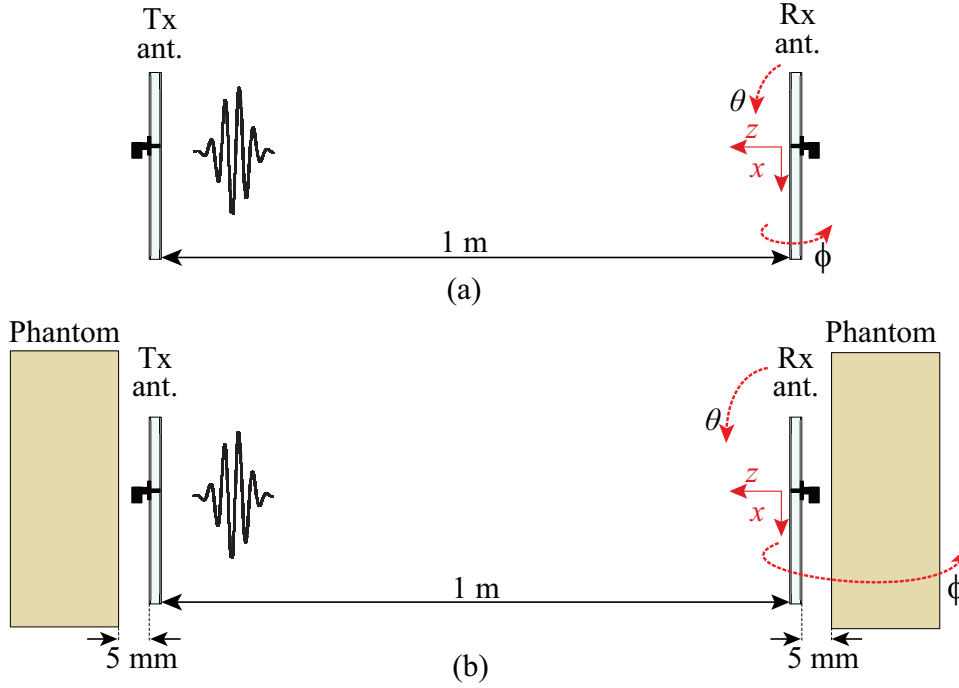


**Figure 4.14:** Simulation setup for time-domain analysis. (a) Free-space case. (b) On-phantom case.

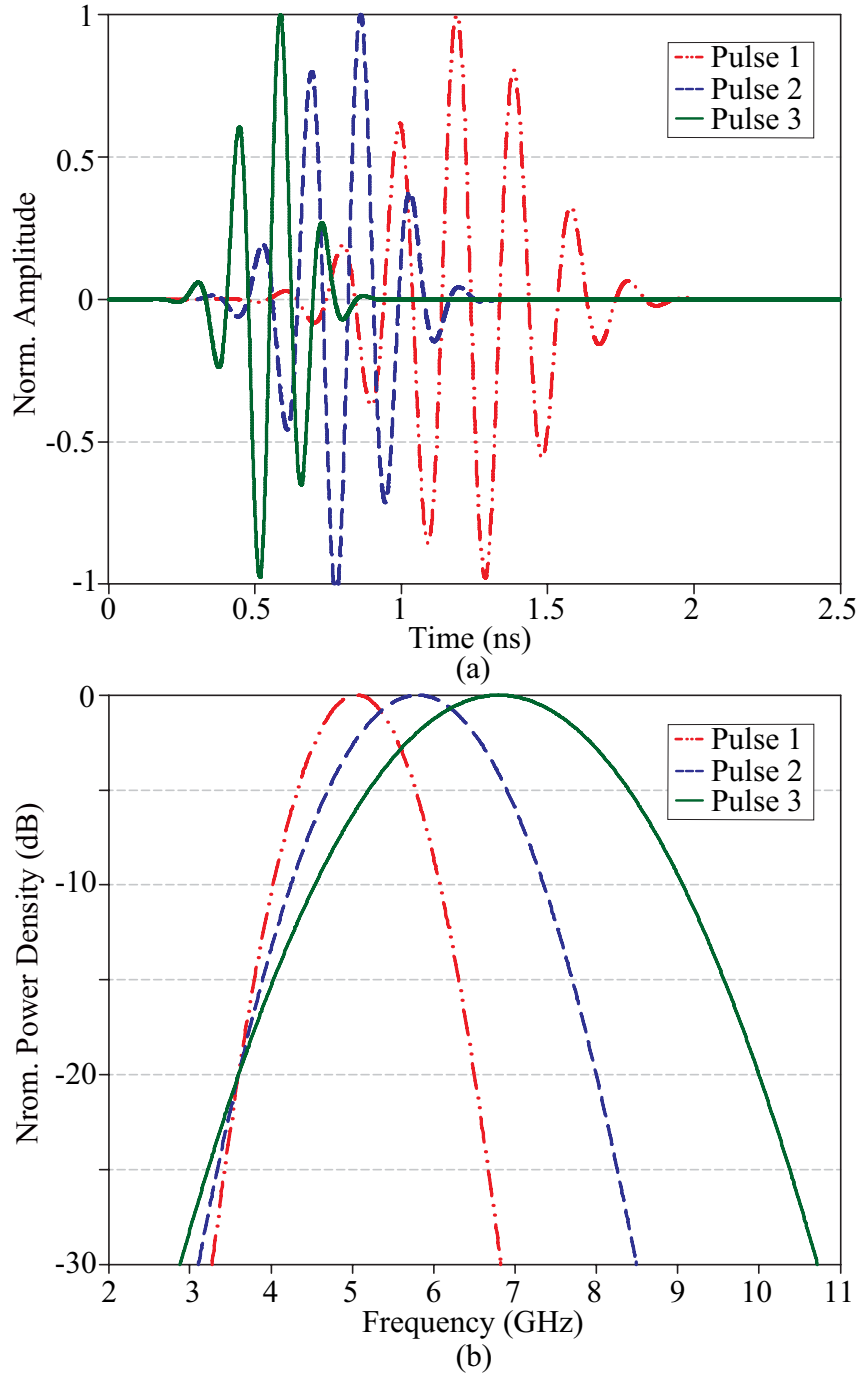
Lastly, the capability of the proposed UWB antenna for a pulse-based transmission was evaluated through a system fidelity analysis in both free-space and on-body environments [85, 86]. To do this, two identical UWB antennas, transmitter (Tx) and receiver (Rx), were aligned in CST Microwave Studio 2016 across 1 m distance as illustrated in Figs 4.14(a) and (b), and the simulated  $|S_{21}|$  parameter of this system was obtained. For the on-body case, the same human-muscle phantom used in the SAR analysis, yet with a smaller dimension ( $110 \text{ mm} \times 110 \text{ mm} \times 50 \text{ mm}$ ) for reduced computational cost, was employed at 5 mm behind each antenna. Considering this setup as a linear time-invariant system [85], the spectrum of the received pulse was obtained by multiplying the spectrum of the input pulse with the transfer function of this system ( $|S_{21}|$ ). An inverse Fourier

transform was then applied to generate the time domain signal of the received pulse.

Three sine-modulated Gaussian pulses shown in Fig. 4.15(a) were considered to excite the Tx antenna, and were different in terms of centre frequency and bandwidth (see Fig. 4.15(b)). Figs 4.16(a) and (b) show the received pulses compared with the corresponding transmitted pulses, obtained through the post-processing explained above, in the case when the Tx and Rx antennas are aligned face-to-face ( $\phi = \theta = 0^\circ$ ) in free space and with the flat phantom. To quantify the antenna's ability to preserve the pulse shape, the SFF was calculated for both cases through a cross correlation between the normalised input and received pulses [86]. Due to the normalisation of the pulses, the SFF value ranges between 0 and 1, with the value of 1 indicating that the received pulse is identical to the input pulse or no dispersion occurred during transmission.

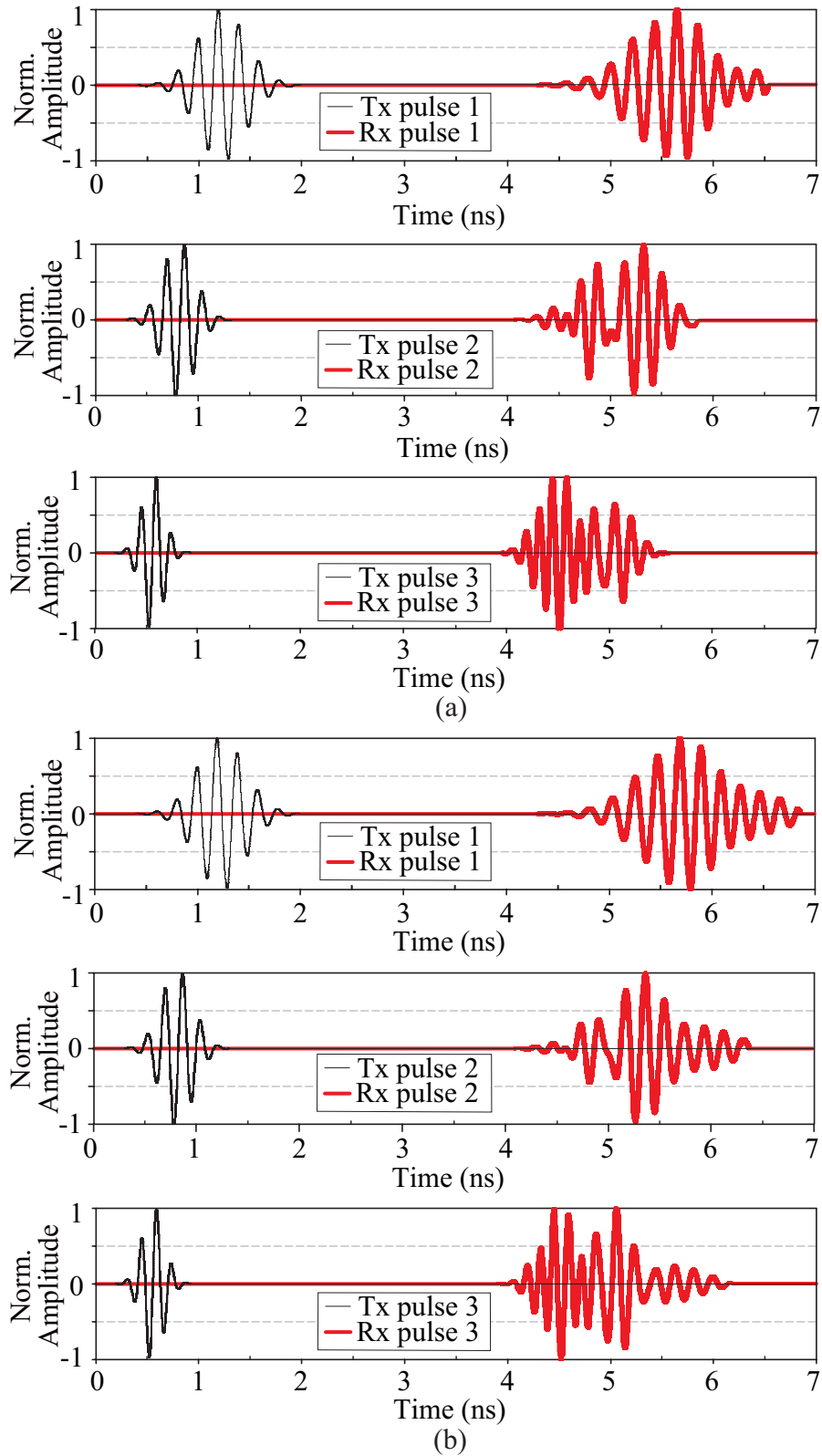
The SFF results are presented in Table 4.2. In general, it can be noticed that the human body has a small effect on the fidelity of the received pulses. However, the SFF does decrease as the bandwidth of the pulse increases, which might be due to the existence of more of the spectra of the pulse falling into the lower radiation region of the antenna [87], i.e. 6.2 GHz and above 8.5 GHz. Nevertheless, the values are still higher than the commonly accepted SFF for UWB signal transmission ( $\text{SFF} > 0.5$ ) [86].

The system fidelity patterns of the antenna when pulse 1 was used as the excitation signal were also obtained. This was performed by rotating the position of the receiver antenna every  $15^\circ$  in both horizontal ( $y$ - $z$ ) and vertical ( $x$ - $z$ ) planes, while maintaining the transmitter antenna stationary. Only the patterns for the upper hemisphere of the antenna were observed considering the radiation mechanism of the antenna. The results are given in Figs 4.17(a) and (b) for the free-space and on-phantom cases. On the flat phantom, the average SFF values were 0.88 and 0.86 in the horizontal and vertical planes, respectively. These are very close to the free-space case in the horizontal plane (0.88) and vertical plane (0.91).



**Figure 4.15:** Different excitation pulses used in the system fidelity analysis. (a) Time domain waveforms. (b) Power spectral density.

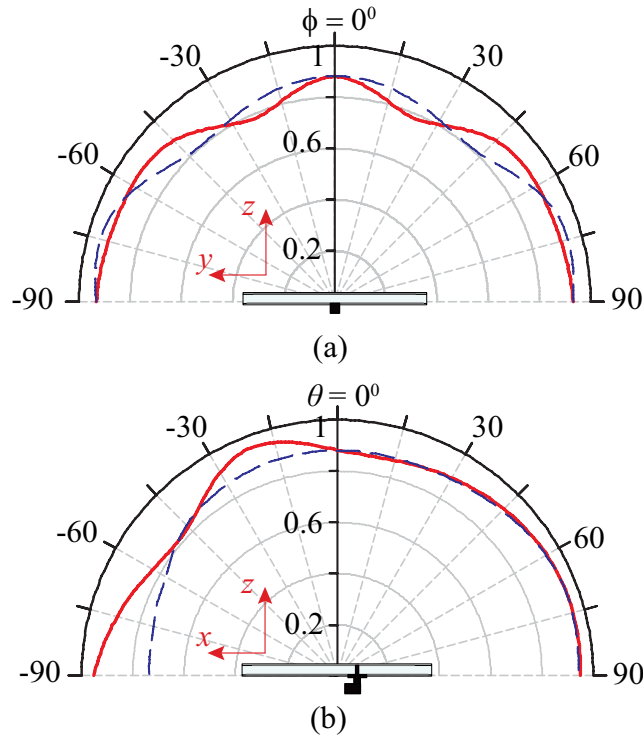




**Figure 4.16:** Simulated Tx and Rx pulses. (a) In free space. (b) With the flat phantom.

**Table 4.2:** System Fidelity Factor of the Antenna at  $\phi = \theta = 0^\circ$  with Three Different Pulses

Signal	SFF	
	Free space	On flat phantom
Pulse 1	0.88	0.88
Pulse 2	0.77	0.79
Pulse 3	0.72	0.68

**Figure 4.17:** System fidelity patterns of the proposed UWB antenna in free space (solid lines) and on the flat phantom (dashed lines), at the (a) horizontal ( $y$ - $z$ ) plane and (b) vertical ( $x$ - $z$ ) plane.

## 4.4 Summary

A new flexible planar UWB antenna with a full ground plane has been presented. As opposed to previously reported flexible UWB antennas, the proposed UWB design: a) maintains a full ground plane which delivers the necessary isolation between the antenna and the human body when worn, and b) exhibits extreme physical robustness attributed to the employed PDMS-embedded conductive fabric fabrication technology. On-body measurements upon a phantom show that the antenna achieves a bandwidth of more than 6 GHz (from 3.68 to 10.1 GHz) with VSWR less than 2.2, an average peak gain of 4.53 dBi, and an average total efficiency of 27%, which are quite close to the performance in free space. For an input power of 0.5 W, the SAR levels in the underlying tissues were found to be less than 2 W/kg, implying conformance with international safety guidelines. Time-domain performance investigations also demonstrated that the proposed antenna is suitable for UWB pulse transmission. The results shown in this chapter specifically validate the applicability of the proposed PDMS-embedded conductive fabric for UWB and high-frequency applications.



## Realising Robust Flexible

## Electronically Tunable

## Antennas using

## PDMS-Embedded Conductive

## Fabric

## 5.1 Introduction and State of the Art

There is a demand for wearable antennas that are not only flexible but electronically tunable. Reconfigurability is of interest in this area as it enhances the functionality of the antenna in modern wireless communication systems. In the last decade, there have been significant advances in rigid reconfigurable antennas made out of conventional substrates, and they have demonstrated reconfigurability of operating frequency, radiation pattern, and polarisation electronically [88–94]. However, the progress has been relatively slow when it comes to the realisation of electronic reconfigurability in flexible antennas.

Some investigations on flexible antennas that are electronically tunable can be found in [8, 42, 81, 95–98]. Among them are pattern-reconfigurable patch antennas realised with

conductive fabric adhered to a felt substrate [95,98], and silver paste on polyester-cotton or 100% cotton fabric [8,97]. Fabric-based frequency-reconfigurable patch antennas, reported in [81,96], utilise denim as the substrate with copper tape and embroidered layers as the conductive parts. An inkjet-printed slot antenna with frequency and polarisation reconfigurability has been reported recently in [42]. The general approach is the utilisation of unconventional materials to meet the flexibility requirement and the addition of lumped components, required for electronic tuning and a biasing network, on top of the flexible materials to obtain the desired reconfigurability (see Figs 5.1(a)–(d)).

One of the primary challenges involved is the robust integration of the lumped components to flexible materials to maintain the reconfigurability. Such exposed lumped elements on top of the flexible material are at a high risk of being detached due to repeated physical deformations, which are possible in a realistic human-body environment (e.g. bending, stretching, and twisting), and also when washing. This problem also applies to the integration of the conductive parts of the antenna and the substrates used, and hence presents a significant challenge in achieving a physical robustness of flexible reconfigurable antennas.

In this chapter, the application of PDMS-embedded conductive-fabric technology is expanded to cover the realisation of robust, flexible, electronically tunable wearable antennas, addressing the aforementioned challenges. The details of the implementation scenario are described in Section 5.2. As concept demonstrations, two new frequency-reconfigurable antenna prototypes have been fabricated and tested; their designs are also presented in this section. In Section 5.3, the RF performance of the fabricated prototype in both free space and on the flat UWB phantom is presented. It is followed by Section 5.4, where a range of mechanical tests to validate the physical robustness provided by the proposed approach is given. They include bending on the human-shaped UWB phantom and machine-washing tests. Finally, a summary is given in Section 5.5.

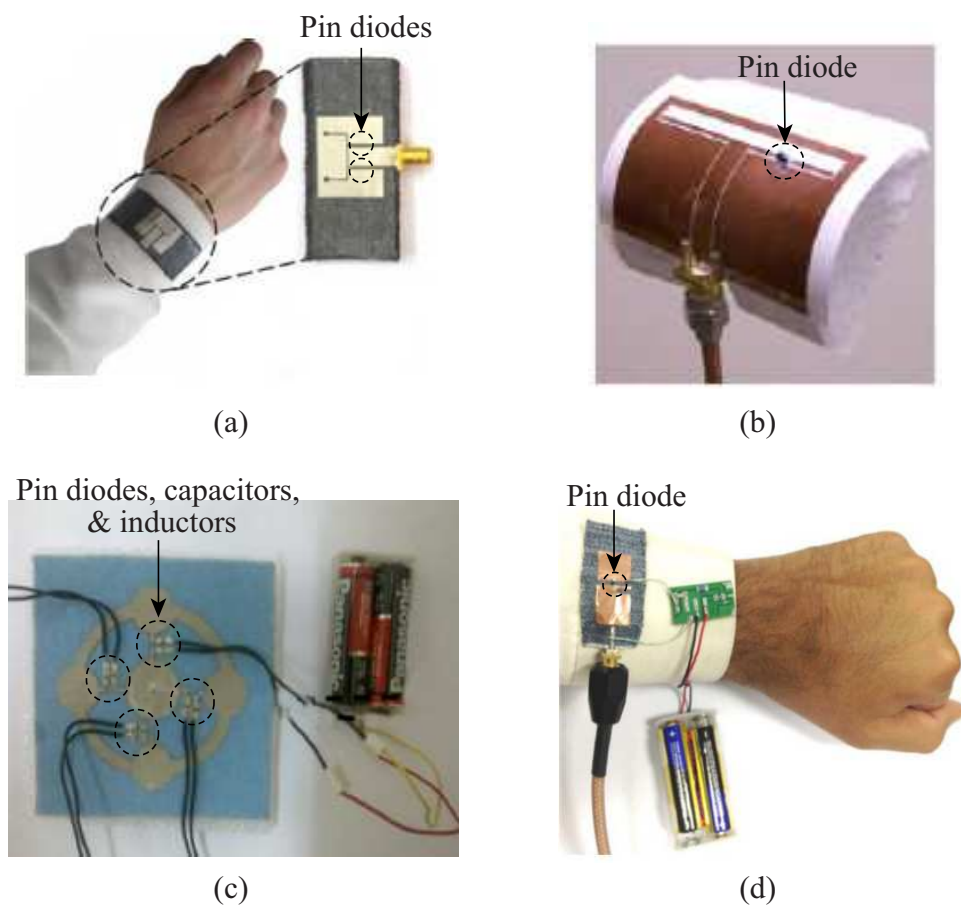


**Figure 5.1:** Some examples of previously reported flexible electronically tunable antennas. (a) [8, 97]. (b) [42]. (c) [95]. (d) [96].

## 5.2 Realisation of Flexible Electronically Tunable Antennas

The development of electronically tunable versions of PDMS-embedded conductive-fabric based antennas is done by adding the electronic tuning components on the body of the antenna before applying the PDMS encapsulation. With the multilayer fabrication approach as described in Section 2.2.2, this process can be done easily. The attachment of lumped tuning components to such materials as conductive fabric and PDMS can also be done through a very simple process.

### 5.2.1 Antenna Configuration

To clearly demonstrate the concept, the antenna illustrated in Fig. 5.2(a), referred to as RFPA 1, was designed initially. An inset-fed rectangular patch antenna with a full ground plane has been selected as the main radiator, considering its advantages of low profile, simplicity, and broadside radiation pattern. The full ground plane is maintained to significantly reduce the coupling to the human body. The rectangular patch was designed to operate in its fundamental mode on top of a PDMS substrate. A thick substrate was used to achieve a modest bandwidth while maintaining the simplicity of the radiator. Other bandwidth-enhancement techniques might be applied but are beyond the scope of this work. To achieve continuous frequency reconfigurability, a U-shaped parasitic patch was introduced around the rectangular patch, and the gap between them was bridged using two GaAs hyperabrupt varactor diodes (MGV 125-20-0805-2) from Aeroflex Metelics. To encapsulate the antenna, additional PDMS layers are applied above the radiating patch and below the ground plane, respectively. The thicknesses of these layers were determined by the height of varactors and the availability of moulds when the antenna was designed.

Later, as an improvement of the first design, the antenna depicted in Fig. 5.2(b),



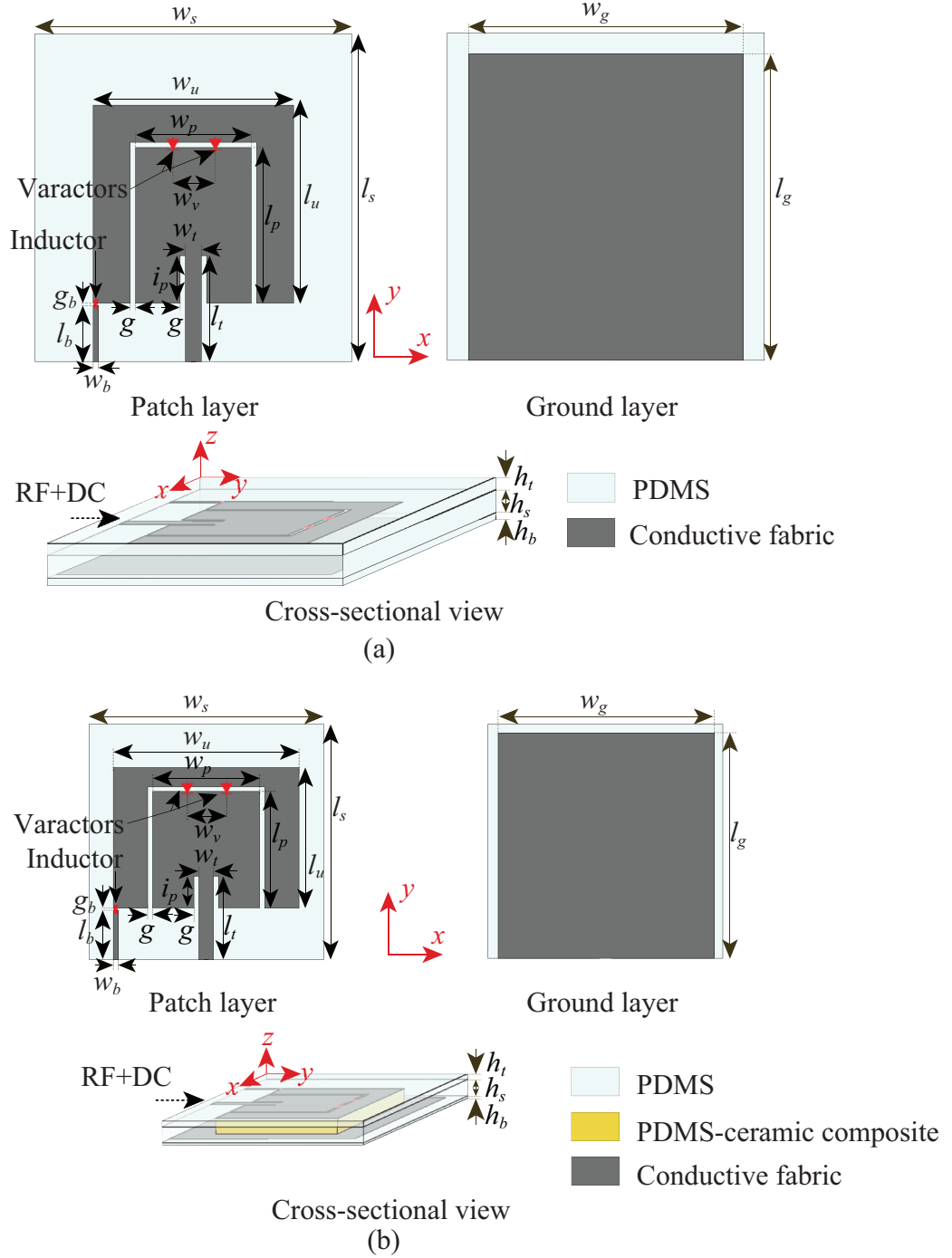


**Figure 5.2:** Configuration of proposed frequency-reconfigurable antennas. (a) RFPA 1. (b) RFPA 2.

referred to as RFPA 2, was developed. Different from the one in Fig. 5.2(a), a PDMS-ceramic composite with 20% volume of  $\text{SrTiO}_3$  was employed as part of the substrate. This  $\text{SrTiO}_3$  loading increases the relative permittivity of PDMS upto 6.36, yet with a marginal change in the loss. As the result, a 52% miniaturisation of the total size of the antenna is achieved, while maintaining its flexibility. The dimension of the composite substrate was optimised to be as large as the area of the radiating patches, after considering the miniaturisation factor and additional dielectric loss contributed by the ceramics. More miniaturisation could be achieved by adding more ceramic powder, but at the expense of further dielectric losses and lower fringing fields due to the high permittivity [99]. These two together will degrade the efficiency of the antenna. Moreover, a larger amount of ceramic loading affects the flexibility of PDMS and complicates its fabrication [55]. The details on the preparation and characteristics of the composite substrate can be referred to Section 2.2.1.

Apart from the inclusion of the PDMS-ceramic composite substrate, the improvement in RFPA 2 includes the use of thinner substrate and encapsulation layers to reduce the profile of the antenna. Moreover, the conductive parts of the antenna were realised using different combinations of conductive fabrics, which leads to a better mechanical robustness. Whilst in RFPA 1 all the conductive parts were realised with CF I, in RFPA 2 the antenna patches were realised with CF I and the ground plane was realised with CF III. CF I was chosen due to its higher conductivity among the other four conductive fabrics, which is necessary for a higher antenna efficiency. On the other hand, considering its high porosity and acceptable conductivity, CF III was chosen over CF IV for the ground plane. Fabric with higher porosity is more beneficial for the PDMS-fabric adherence over such a large surface as the ground.

Both antennas were designed and optimised using CST Microwave Studio 2016. The final dimensions of both antennas are given in Table 5.1. In simulation each varactor

**Table 5.1:** Detailed Dimensions of RFPA 1 and 2

Parameter	Dimension (mm)		Parameter	Dimension (mm)	
	RFPA 1	RFPA 2		RFPA 1	RFPA 2
$w_s$	59.8	40.2	$l_p$	29.4	21.6
$l_s$	59.8	42.6	$g$	1	1
$w_g$	51.8	38.2	$w_v$	8	4
$l_g$	55.9	41.6	$w_t$	3	3
$h_b$	0.76	0.2	$l_t$	20	17
$h_s$	3.18	2.5	$i_p$	9	7
$h_t$	1.52	0.76	$g_b$	0.5	0.5
$w_u$	37.8	32.2	$w_b$	1	1
$l_u$	37.4	25.6	$l_b$	10.5	9.5
$w_p$	21.8	18.2			

**Table 5.2:** Reverse-Bias Voltage and Corresponding Varactor Junction Capacitance

Bias State	$V_1$	$V_2$	$V_3$	$V_4$	$V_5$	$V_6$
Voltage (V)	0	2	4	6	10	20
$C_j$ (pF)	1.1	0.72	0.46	0.34	0.187	0.097

was modelled with a series RLC equivalent circuit, which consists of  $R_s$  of  $1.6 \Omega$ , diode parasitic inductance ( $L_p$ ) of  $0.4 \text{ nH}$ , parasitic capacitance ( $C_p$ ) of  $0.06 \text{ pF}$ , and  $C_j$  as given in Table 5.2 [88,100]. The MGV 125-20-0805-2 diode was particularly selected due to its low  $R_s$  and adequate range of  $C_j$  for a corresponding reverse-bias voltage variation from 0 to 20 V.

The varactors are placed at the upper gap as shown in Figs 5.2(a) and (b), in line with the current distribution on the patch, that flows predominantly in the  $y$ -direction (see Fig. 5.3). Therefore, variation of the varactor reverse-bias voltage changes the effective electrical length of the patch and hence the antenna resonance frequency. The anodes of both varactors are connected to the parasitic patch, while the cathodes are connected to the main patch. Both varactors are reverse biased by the same Direct

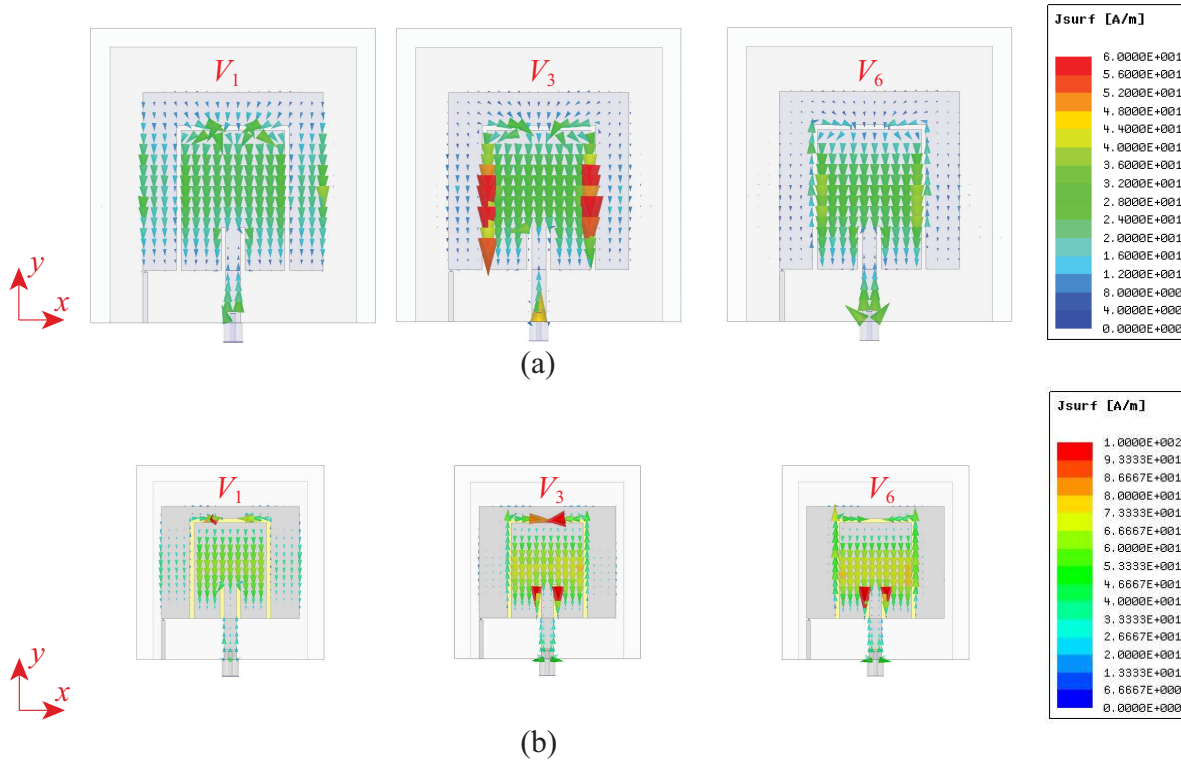


**Figure 5.3:** Current distribution of the antenna at its resonance frequency corresponding to the given reverse-bias voltages. (a) RFPA 1. (b) RFPA 2.

Current (DC) voltage, applied to the antenna input together with the RF signal through the input connector. The parasitic patch is DC grounded by a thin conducting line, which is isolated from the RF signal by an RF-choke chip inductor (47 nH) from Coilcraft.

The number of varactors in the antenna mainly affects the frequency tuning range and the efficiency of the antenna. A fixed distance of  $w_v$  has been maintained between varactors. As shown in Figs 5.4(a) and (b), addition of more varactors decreases the resonance frequency and increases the efficiency of the antenna. Giving consideration to tuning range, efficiency, and cost, two varactors were selected for the prototype.

### 5.2.2 Fabrication

The realisation process, which in principle is similar to the steps described in Section 2.2.2, is illustrated in Fig. 5.5 and detailed below:

1. Get the solutions, varactors, and inductor ready. Cut the conductive fabric manually following the antenna dimensions given in Figs 5.2(a) and (b), and prepare the moulds and base.
2. For both designs, attach the first mould to the base with a silicone sealant, pour the PDMS solution into the mould, degas in a vacuum desiccator for approximately 30 minutes, and then cure in an oven at 65°C for about 2 hours.
3. Attach the ground plane on top of the cured bottom encapsulation layer of both designs with a thin uncured PDMS solution, repel the bubbles occurring between them, and cure in an oven at 75°C for 20 minutes.
4. For RFPA 1, repeat Step 2 with the second mould to make the middle PDMS layer. On the other hand, for RFPA 2, position the third mould so that its aperture fits the position of the radiator patches in the design. Then pour the composite solution into the mould, degas in the vacuum desiccator for about 40 minutes and cure in an

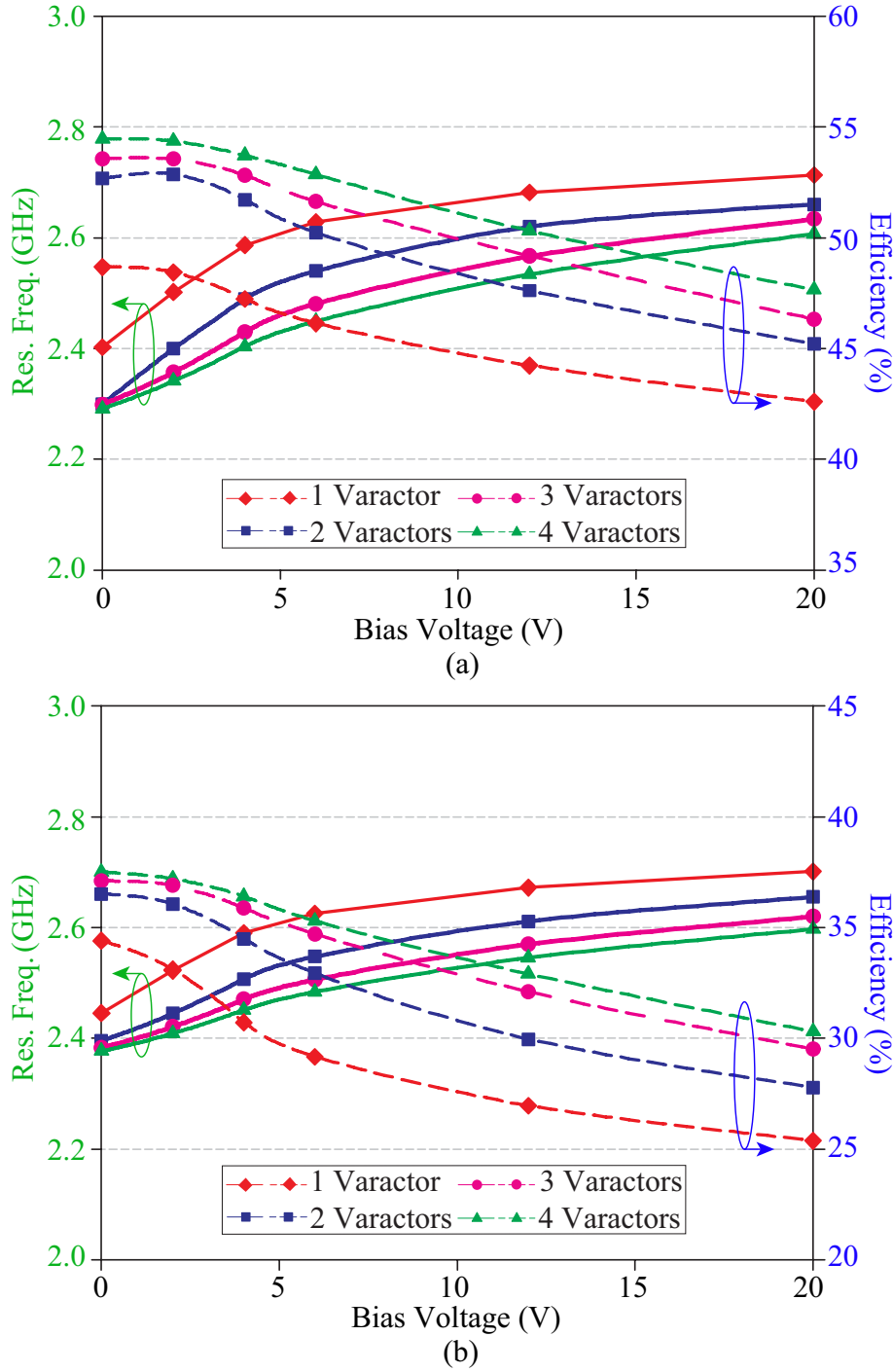


**Figure 5.4:** The effects of the number of varactors on the resonance frequency and total efficiency of the antenna. (a) RFPA 1. (b) RFPA 2.

oven at 65°C for 2 hours. Once cured, remove the third mould by cutting the edges of the cured composite layer. After that, attach the second mould and repeat Step 2 to make the middle PDMS layer around the composite substrate.

5. Repeat Step 3 for the main patch, parasitic patch, and bias line of both RFPA 1 and 2. Once they attach firmly, connect the varactors and the inductor using silver epoxy, then cure in an oven at 65°C for 1 hour.
6. For both designs, repeat Step 2 with the fourth mould to make the top encapsulation layer.
7. Peel carefully the prototypes from the mould. If necessary, trim the excess PDMS layers from the edges of the antennas following the dimensions in Figs 5.2(a) and (b)).

Customised ring-shaped moulds made out of commercial laminates from Taconic having the thicknesses required by the designs were used to guarantee the accuracy of the thickness of each layer. Specifically, for the third mould, the width and length of the aperture were exactly made following the area of the radiator patches of RFPA 1. This is to ensure that the size of the composite substrate fits the area of the radiating patches.

The top and bottom encapsulation layers were cut slightly at the edges of the transmission lines and the bias lines. This is so that SMA connectors and a short copper wire connecting the bias line to the ground plane can be attached by means of silver epoxy for measurement purposes. To cure the epoxy, the antennas were left again in an oven at 65°C for another 1 hour. The photographs of the fabricated electronically tunable antennas are shown in Figs 5.6(a) and (b).

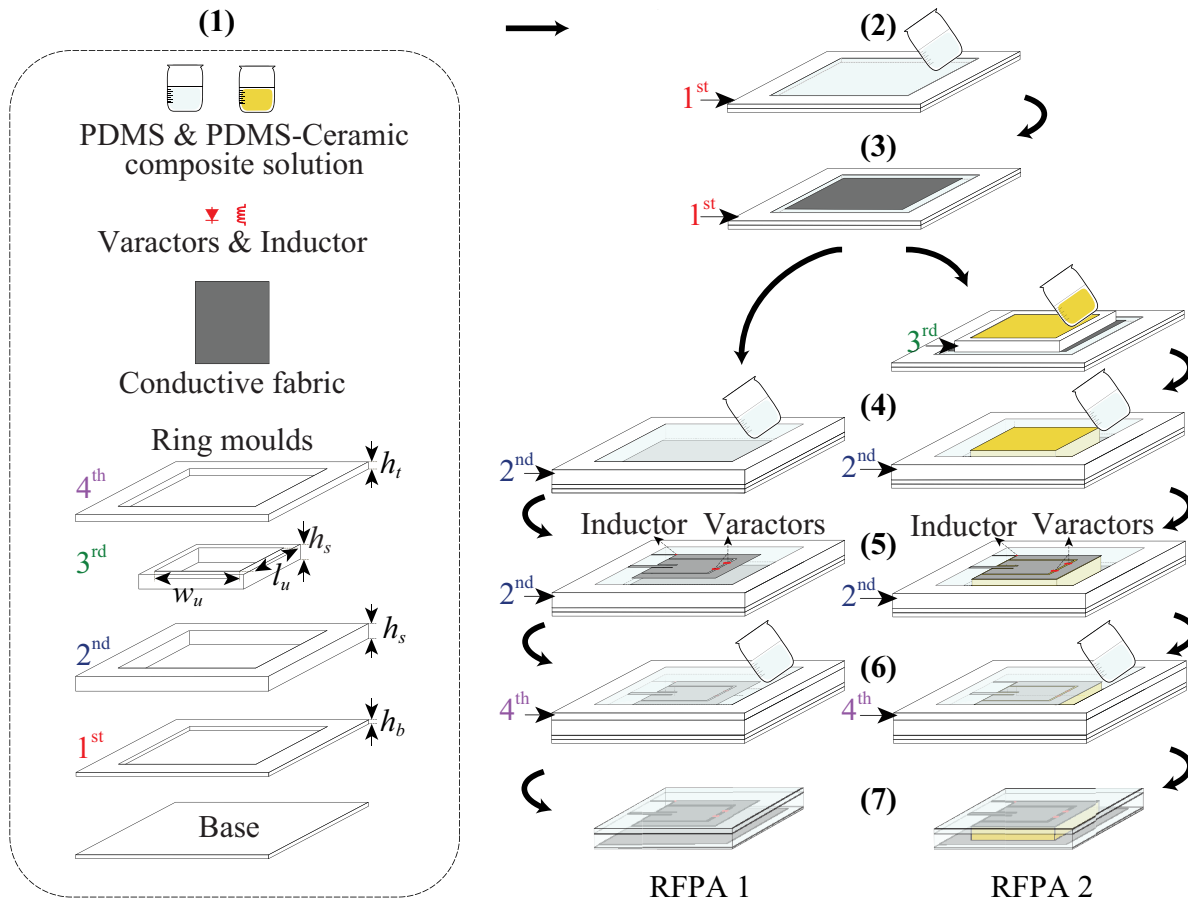


**Figure 5.5:** Schematic illustration of the fabrication process of the PDMS-embedded conductive-fabric based reconfigurable antennas. The numbers represent the order of the process.



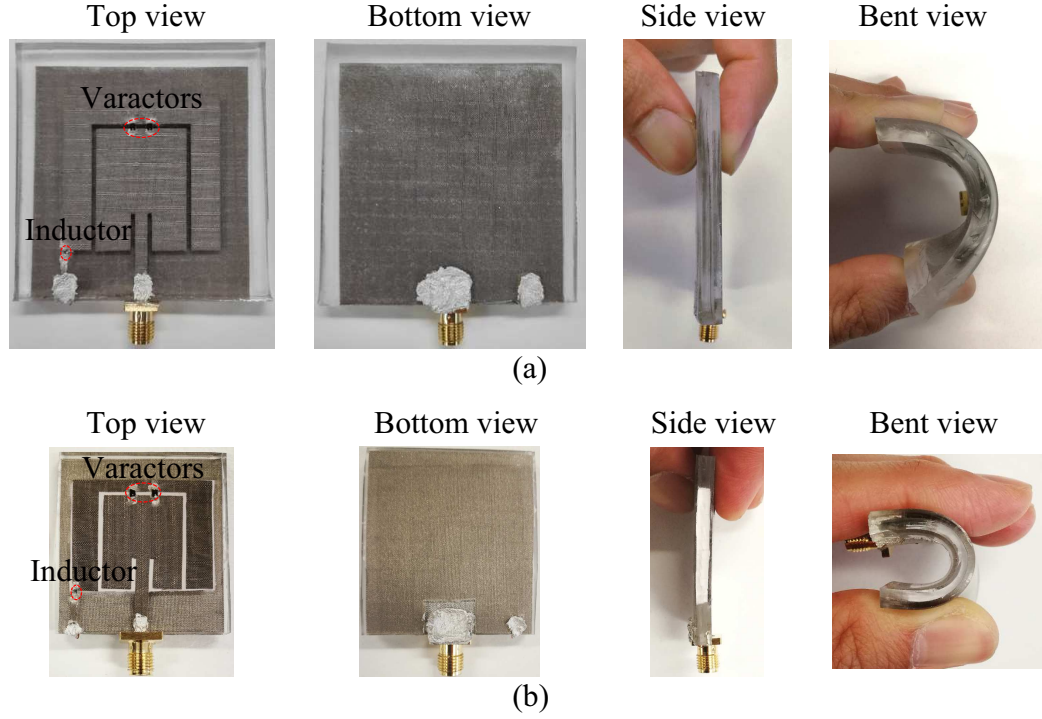


**Figure 5.6:** Fabricated reconfigurable antenna prototypes. (a) RFPA 1. (b) RFPA 2.

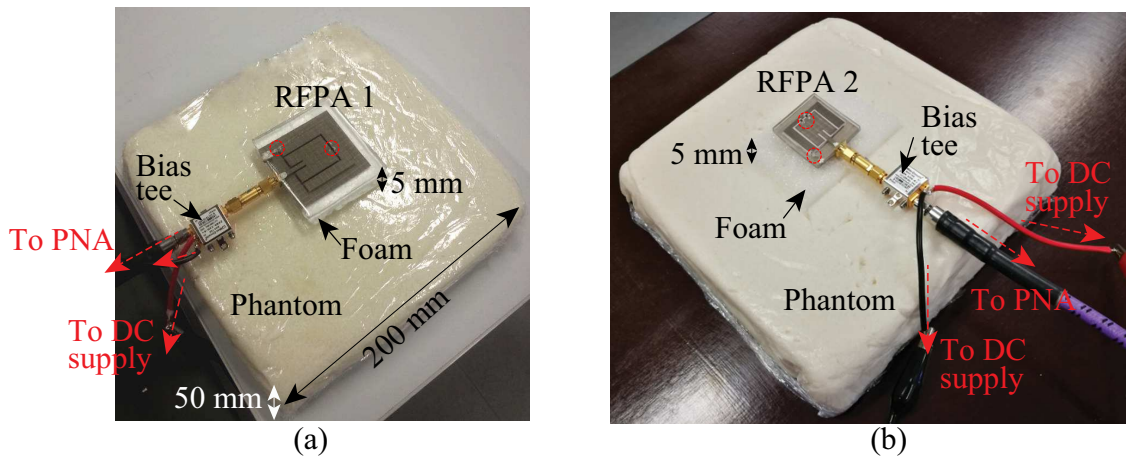


**Figure 5.7:** Experimental setup for  $|S_{11}|$  measurements of the antenna on the flat phantom.

(a) RFPA 1. (b) RFPA 2.

## 5.3 Performance of Fabricated Prototype

To validate the concept the RF performance of both prototypes was next characterised in free space and in an on-body environment using both of the UWB semisolid phantoms described in Section 3.3.1. A gap of 5 mm was maintained between the antennas and the phantom using a small foam block (see Figs 5.7(a) and (b)). The conducted measurements including the  $|S_{11}|$  characterisation using the Agilent PNA-X N5242A network analyser, calibrated using an electronic calibration module N4691B from Keysight, and far-field characterisation in the NSI700S-50 spherical near-field antenna range at the AusAMF, Marsfield. A DC power supply from Sorensen (XG 300-2.8) was utilised to supply the reverse-bias voltage (0 to 20 V) to the antenna, which was applied together with the RF signal into the antenna input port by using a bias tee. This approach eliminates the need for a complex bias circuit, and hence maintains simplicity and avoids radiation performance degradation caused by the cables associated with the bias network.

### 5.3.1 Input Matching

The comparison between the simulated and measured  $|S_{11}|$  of RFPA 1 in free space and on the flat phantom are shown in Figs 5.8(a) and (b), while for RFPA 2 they are shown in Figs 5.9(a) and (b). As can be seen, the measured results are largely in accord with the simulations. Slight variations in the resonance frequencies and input reflection coefficients could be attributed to the antenna fabrication tolerances (during manual cutting of the fabric and alignment of the parasitic patch), the uncertainties in the capacitance values of the varactor, and the variations in the material properties of the antenna and fabricated phantom. In free space, RFPA 1 demonstrates a resonance frequency tuning from 2.3 to 2.65 GHz with an average 10-dB return-loss bandwidth of 3.3%, whereas RFPA 2 demonstrates a resonance frequency tuning from 2.37 to 2.66 GHz with an average 10-

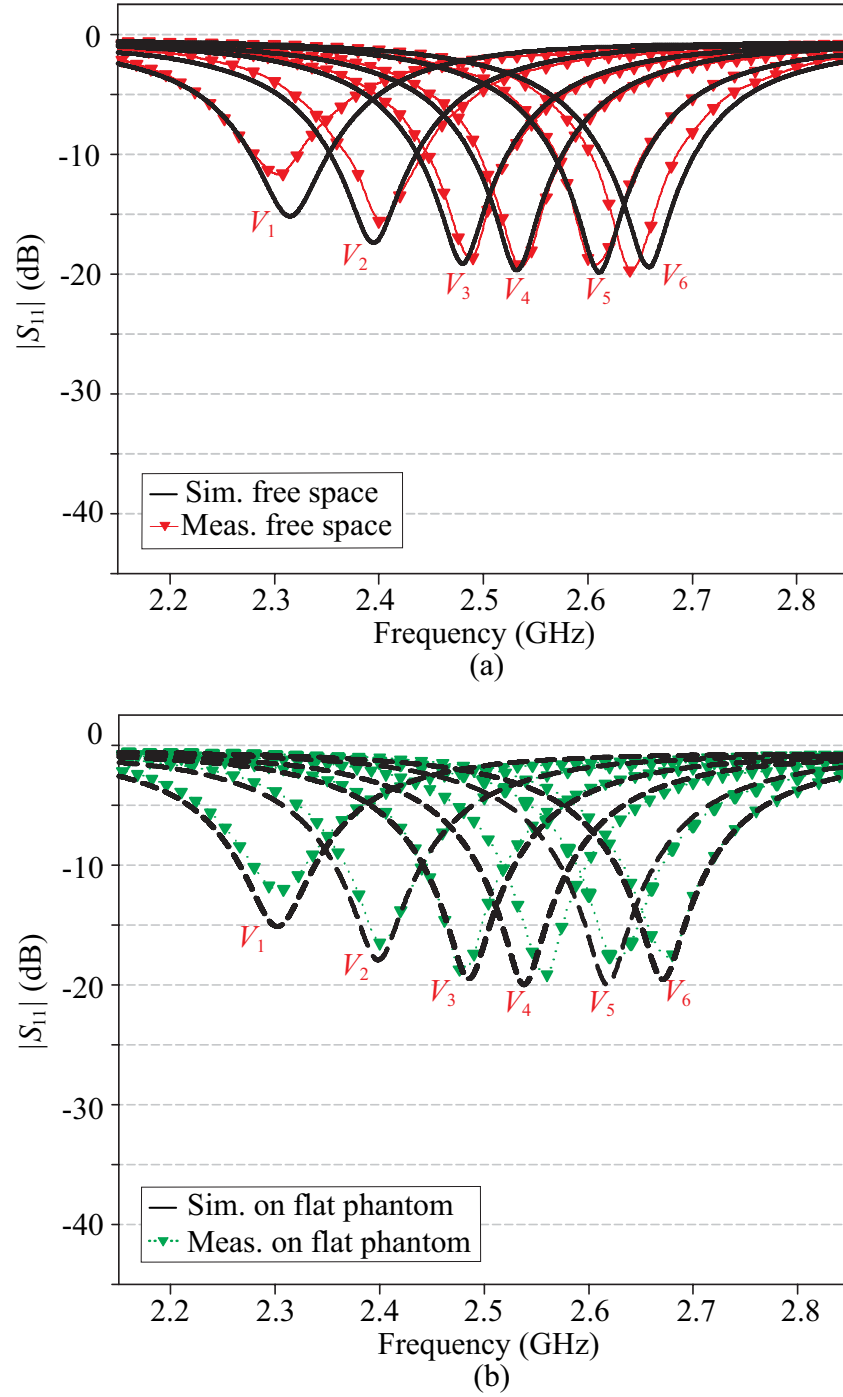


**Figure 5.8:** Simulated and measured  $|S_{11}|$  of RFPA 1 with various reverse-bias voltages. (a) In free space. (b) On the flat phantom.

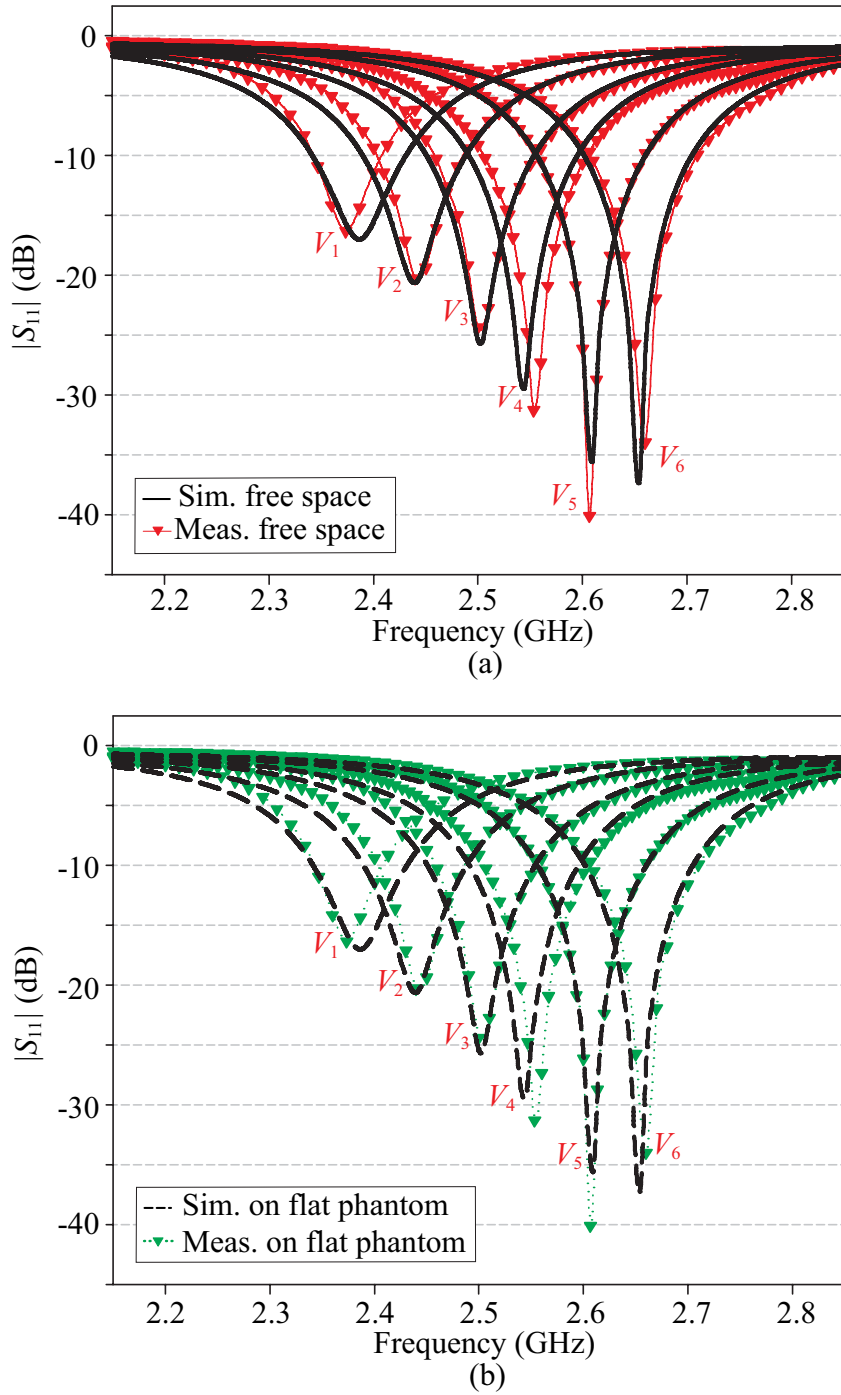


**Figure 5.9:** Simulated and measured  $|S_{11}|$  of RFPA 2 with various reverse-bias voltages. (a) In free space. (b) On the flat phantom.

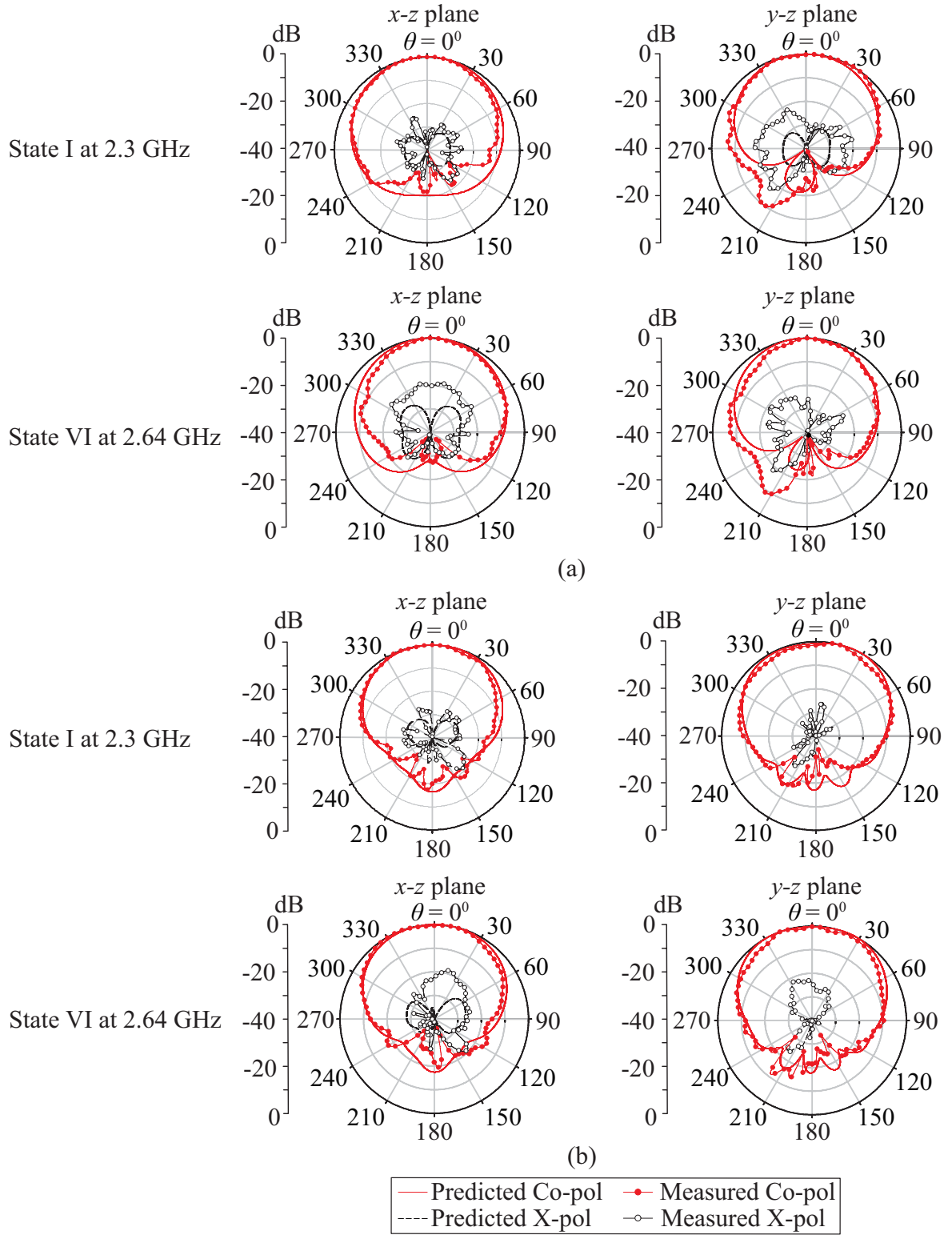
dB return-loss bandwidth of 3.7%, both validating the proposed continuous frequency reconfigurability. When in close proximity to the flat phantom, the changes in the  $|S_{11}|$  of both antennas are generally insignificant (see Figs 5.8(b) and 5.9(b)), which suggests low coupling to the body when the antennas are worn, due to the full ground plane. The tuning range of the proposed antennas can be extended further if varactors with a wider variation of  $C_j$  are used. Another alternative is to utilise a slot type antenna, which although suffers from backside radiation, generally has a wider resonance tuning capability than a microstrip patch antenna [101]. The enhancement of the antenna reconfiguration ratio, however, is out of the scope of this work, which mainly focuses on applying the proposed PDMS-embedded conductive fabric method for the realisation of flexible reconfigurable antennas with robust performance.

### 5.3.2 Far-Field Characteristics

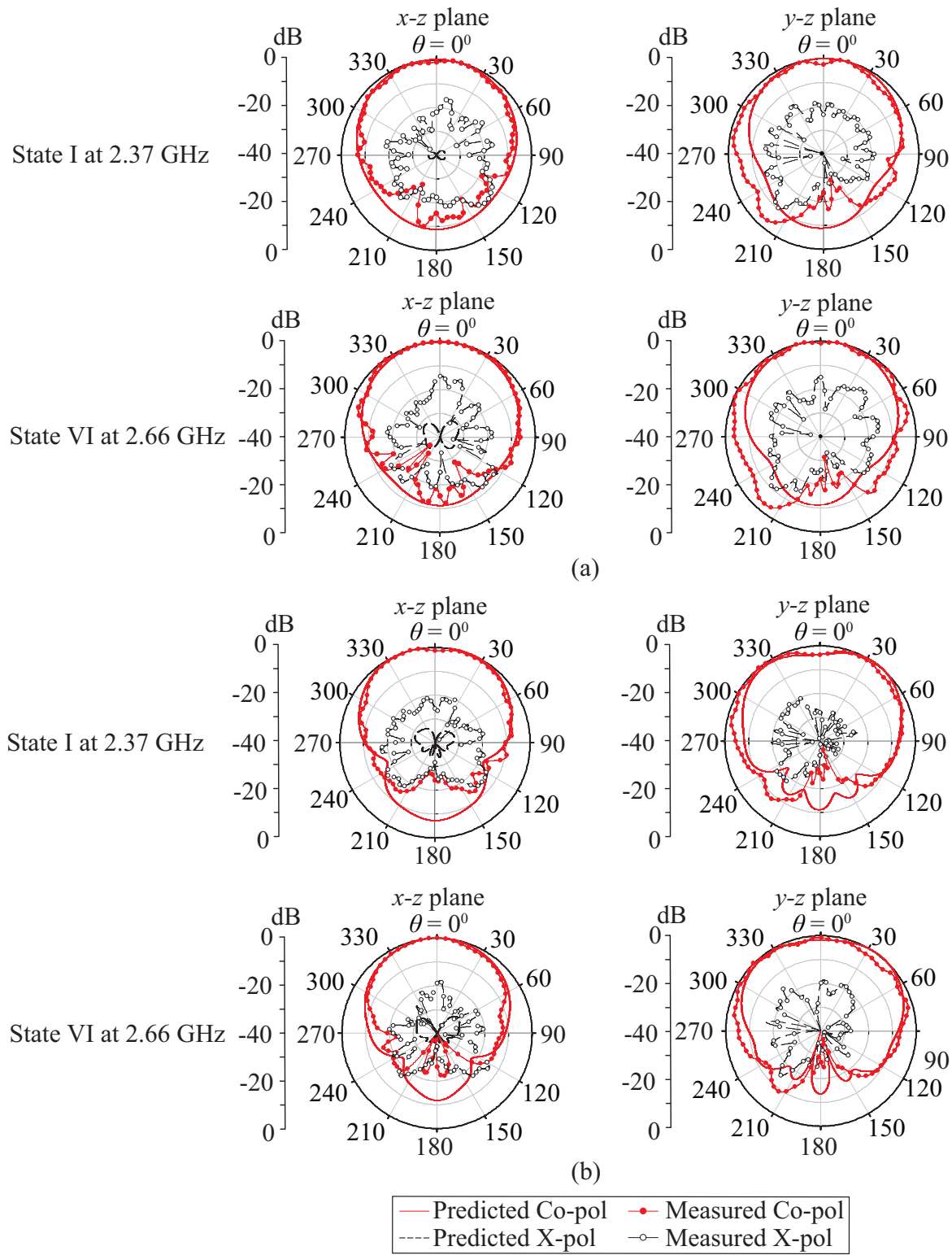
The measured far-field patterns of RFPA 1 in free space and with the flat phantom are depicted in Fig. 5.10, and for RFPA 2 are given in Fig. 5.11, all compared with their simulated results. All the patterns are shown at the free-space resonance frequency of each state and are in good agreement. For brevity, only the results at States I and VI are given. Due to the operation in the fundamental mode, both antennas produce broadside radiation, which makes them suitable for off-body communications. The patterns are quite stable over the entire tuning range, with cross-polarisation levels remaining below -15 dB in both  $x$ - $z$  and  $y$ - $z$  planes.

Table 5.3 summarises the peak gains and total efficiencies of both antennas. A good agreement is shown between the simulated and measured results in free space as well as with the flat phantom. In general, the gains and efficiencies of RFPA 2 are lower than those of RFPA 1 as the consequence of the conductive-fabric selection and the inclusion of the PDMS-ceramic composite. When the antennas were placed near the flat phantom,

the decrease in the gains and efficiencies were found to be more in RFPA 2 which is to be expected due to the smaller ground plane compared to that of RFPA 1. Nevertheless, in addition to the significantly smaller size, a better physical robustness can be expected from RFPA 2, thanks to the right conductive-fabric combination.



**Figure 5.10:** Normalised radiation patterns for RFPA 1 at states I and VI. (a) In free space. (b) On the flat phantom.



**Figure 5.11:** Normalised radiation patterns RFPA 2 at states I and VI. (a) In free space. (b) On the flat phantom.



**Table 5.3:** Summary of the Peak Gains and Total Efficiencies of the Fabricated Prototypes over the Entire Tuning Range (0 to 20 V Reverse-Bias Voltages)

Result	RFPA 1		RFPA 2	
	Gain (dBi)	Tot. Eff. (%)	Gain (dBi)	Tot. Eff. (%)
Sim. free space	2.9 to 3.4	40 to 47	0.6 to 1.4	29 to 40
Meas. free space	2.9 to 3.3	40 to 46	0.4 to 1.3	28 to 39
Sim. on flat phantom	2.4 to 3	36 to 39	-1.0 to -0.3	18 to 19
Meas. on flat phantom	2.3 to 2.9	34 to 38	-1.1 to -0.3	16 to 19

### 5.3.3 SAR

An investigation of the RF exposure of the antennas on the body was also conducted experimentally using an APREL ALSAS-10U System at the City University of Hong Kong. That is to ensure compliance to the safety guidelines on human exposure to radio-frequency (RF) fields (IEEE C95.1-2005) [70]. The setup is illustrated in Fig. 5.12. The antenna was placed 5 mm from the liquid-based phantom, made out of water, glycol, and triton X-100, which emulates the dielectric properties of the human body at 2.45 GHz ( $\epsilon_r = 51.62$  and  $\sigma = 1.91$  S/m). Due to the limited selection of phantom liquids available, the measurements were only conducted for the cases where both antennas resonated at 2.45 GHz. Those were when the DC bias voltages of 3.5 and 2 V were applied to RFPA 1 and 2, respectively. From the measurements with 20 dBm input power, maximum SAR values of 0.053 and 0.151 W/kg (averaged over 10 g of tissue) were obtained from RFPA 1 and 2, respectively. The SAR of RFPA 2 was found to be higher than RFPA 1 as the consequence of having smaller size of ground plane. Moreover, the ground plane of RFPA 2 was realised with CF III which is less conductive than CF I used in RFPA 1.

These measured SAR values were confirmed with the results in Figs 5.13(a) and (b), obtained by simulating each antenna 5 mm above a muscle-equivalent phantom having the same dimensions with the container of the liquid-based phantom used in the measurement, 320 mm  $\times$  250 mm  $\times$  50 mm. The input power was set to 100 mW (20 dBm) and the values of  $C_j$  were adjusted to 0.5 and 0.72 pF for RFPA 1 and 2, respectively, to get the resonance of both antennas at 2.45 GHz. As can be observed, the simulated peak SAR values (0.037 and 0.142 W/kg for RFPA 1 and 2, respectively) are quite close to the measured results and both are well below the 2 W/kg limit [70], demonstrating the antenna's suitability for operation close to the body.

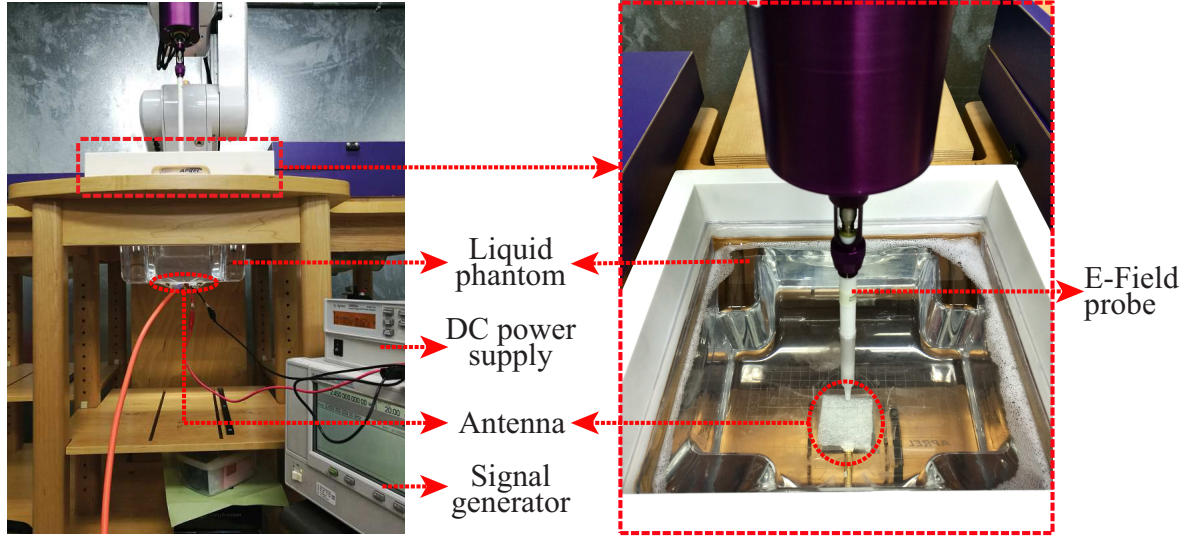


**Figure 5.12:** SAR measurement setup with APREL ALSAS-10U system.

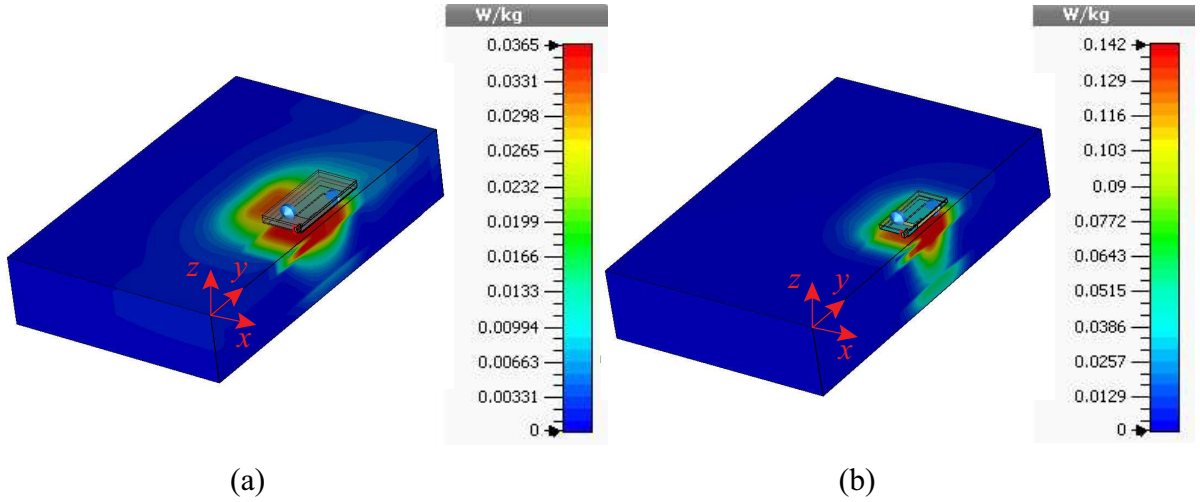


**Figure 5.13:** Simulated 10-g averaged SAR distribution of the antenna at 2.45 GHz when operating 5 mm above the human phantom with an input power of 100 mW. (a) RFPA 1. (b) RFPA 2.

## 5.4 Tests of Physical Robustness

### 5.4.1 Effect of Bending

To highlight the robustness of the proposed method for realisation of conformal reconfigurable antennas, the antenna on-body performance under different bending scenarios was investigated experimentally. This was done by wrapping each antenna around the wrist of the human-shaped phantom, representing an extreme scenario of deformation with a bending radius of 28 mm. The bending was done sequentially in two ways, i.e., along the  $E$ -plane and along the  $H$ -plane of the antenna, as shown in Fig. 5.14.

The measured  $|S_{11}|$  results for each placement are compared in Figs 5.15(a) and (b). For brevity, only the results for three different states are shown. As expected, due to the significant alteration in the main current path of the antennas, the bending in their  $E$ -

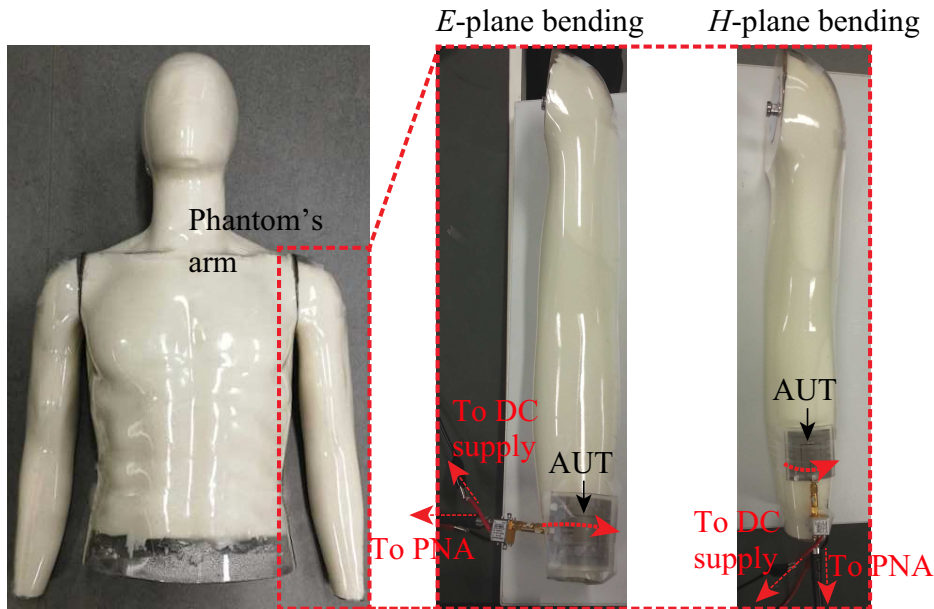


**Figure 5.14:** The antenna wrapped around the wrist of the UWB phantom in two different bending configurations.

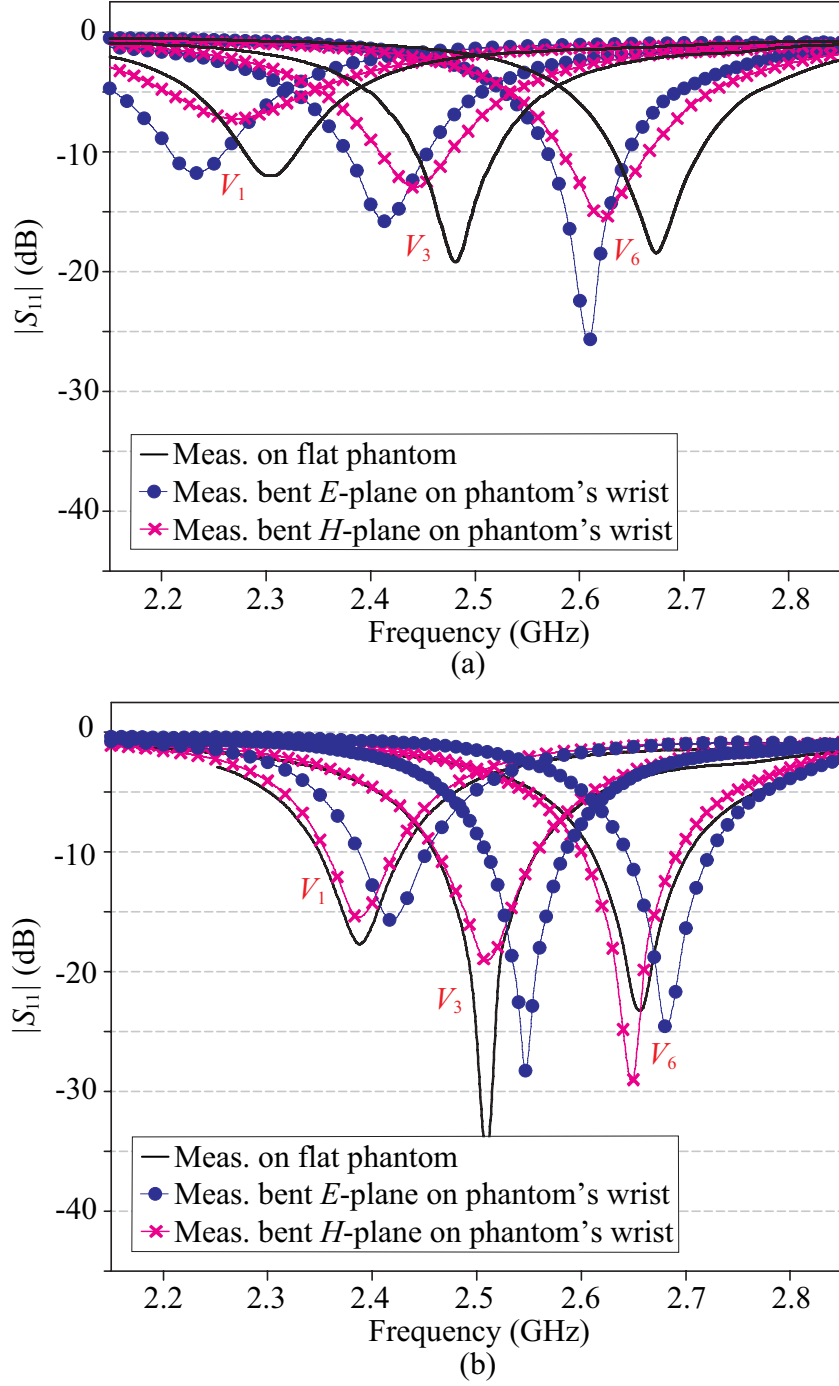


**Figure 5.15:** Measured  $|S_{11}|$  of the antenna with various reverse-bias voltages under bending on the phantom's wrist. (a) RFPA 1. (b) RFPA 2.

plane has a major effect to the resonance frequency, whereas bending in the  $H$ -plane has a negligible effect on the antennas' input impedance and resonance frequency. Therefore, it is normally suggested to avoid bending the antenna in its  $E$ -plane [68]. However, this should not be a problem here, as the resonance frequency can always be returned to the desired frequency by slightly changing the bias voltage.

Interestingly, it is noted that the trends of the frequency shifts in RFPA 1 and 2 under bending are different. In RFPA 1, the resonances generally shift down in frequency, while in RFPA 2, the shift is in the opposite direction. It is then concluded that the irregularity of the PDMS adhesive spread during fabrication, the strength of the conductive fabric-PDMS integration, and the compressible nature of the PDMS layer might lead to unpredictable behaviour when the antenna is deformed. In relation to the latter issue, bending the antenna creates some zones with reduced substrate thickness and some zones with increased substrate thickness. However, most importantly due to the flexibility of the combined PDMS or PDMS composite and conductive fabric, the antennas can be bent easily to a radius of less than 28 mm, and still return to their original shape. Moreover, the reconfigurability of the antenna still functions well even under severe bending, thanks to the PDMS encapsulation that firmly seals the electronic tuning components on the conductive fabric. These results prove the robustness provided by the proposed method against physical deformation.

### 5.4.2 Effect of Washing

The robustness provided by the proposed method was further verified through a washability test. Both the antennas were washed in a household washing machine together with other laundry using detergent, bleach, and 40°C water in one complete cycle for around 45 minutes (see Fig. 5.16). Each connector of the antennas was sealed with a plastic cap and tape to minimise the water exposure and to protect it against turbulence inside the



**Figure 5.16:** The antenna inside the washing machine.

machine. Once dry, the  $|S_{11}|$  parameters of both antennas were re-measured.

The measured  $|S_{11}|$  results of the antennas, before and after washing, are compared in Figs 5.17(a) and (b). Note that the antenna has very well retained its frequency reconfigurability after washing, showing almost identical performance before and after washing. The minor changes in the resonance frequencies and matching levels after washing are likely caused by the SMA-to-antenna connection that was flexed slightly due to the turbulence in the washing machine. These results validate the superiority of the proposed method. The PDMS encapsulation keeps the conductive parts of the antenna as well as the lumped tuning elements from being detached during washing and also protects them from water or any other chemical exposure. Consequently, a well-preserved antenna efficiency can be expected, since PDMS prevents the dissolution of the fabric's conductive materials [102].

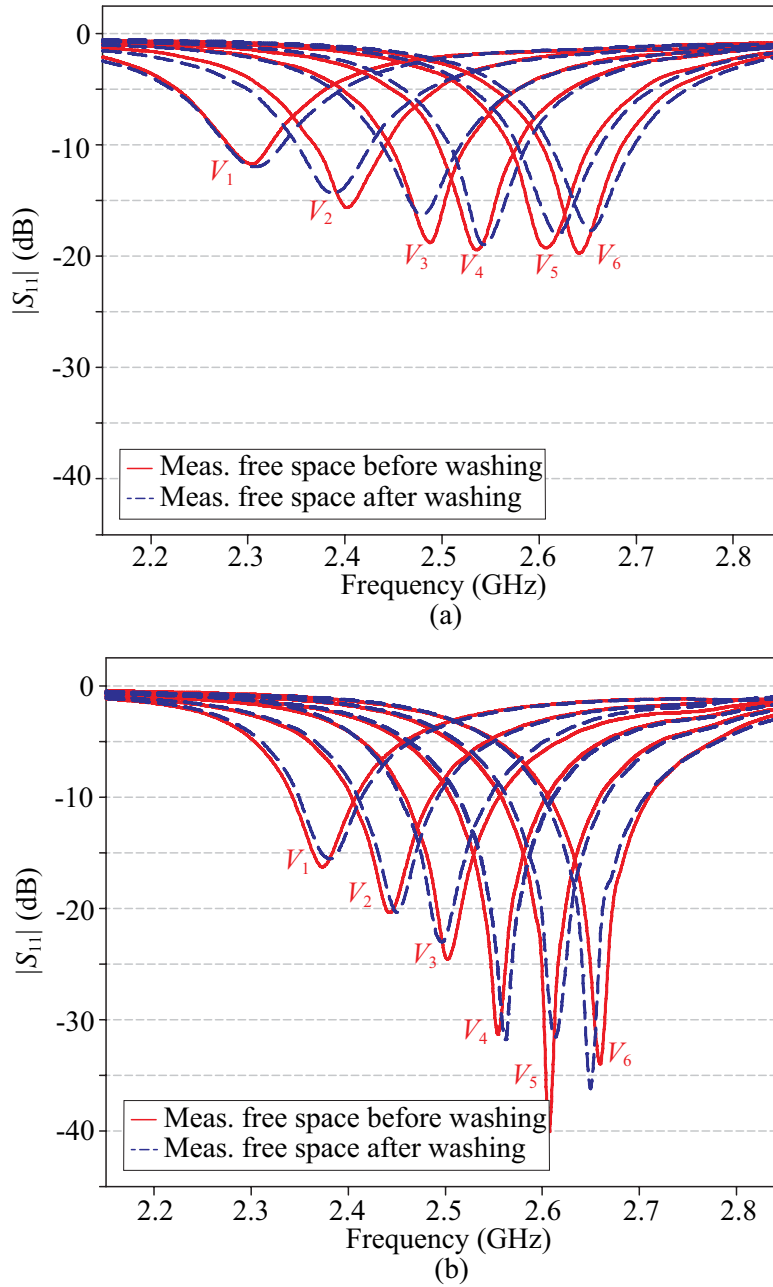


**Figure 5.17:** Measured  $|S_{11}|$  of the antennas with different reverse-bias voltages before and after machine washing. (a) RFPA 1. (b) RFPA 2.



## 5.5 Summary

It has been successfully demonstrated how the proposed PDMS-embedded conductive-fabric technology can be used to realise a robust, flexible, frequency-reconfigurable and wearable antenna. The measured results (in free space and on a UWB phantom) of the two antennas fabricated with the proposed method are in good agreement with the predicted results, thus validating the concept. Through several mechanical tests, it was confirmed that a reconfigurable antenna fabricated using this method can endure physical deformation and machine washing while preserving its reconfigurability. When measured in close proximity to the phantom, RFPA 1 provides continuous frequency tuning from 2.3 to 2.65 GHz with an average peak gain of 2.6 dBi. On the other hand, its miniaturised version, RFPA 2, provides continuous frequency tuning from 2.37 to 2.66 GHz with an average peak gain of -0.7 dBi. These results verify the applicability of the proposed approach for realisation of robust flexible electronically tunable antennas with various types of reconfigurability, including pattern and polarisation reconfigurability, suitable for modern wearable wireless systems.



---

# 6 Conclusions and Future Work

## 6.1 Summary and Findings

In this thesis, a new practical approach to achieve robustness with flexibility in wearable antennas has been demonstrated. The proposed approach, namely PDMS-embedded conductive fabric, combines the use of woven conductive fabric acting as the radiator and the ground plane of the antenna, with PDMS polymer used as the antenna substrate and encapsulation layer. Thorough investigations on the mechanical and electrical characteristics of such combinations of materials have been conducted, the results of which provide an insight into the mechanical robustness of this combination, the constraints associated with the selection of fabric for various parts of the antenna, and the effective modelling of the antenna. The results showed that, by embedding the conductive fabric inside the PDMS, a strong integration between them can be achieved, due to the PDMS-PDMS bonding created through the pores of the fabric. In relation to the porous nature of the fabric, it was also shown that there is always a trade-off between the antenna's mechanical stability and total efficiency when selecting the conductive fabric. A higher-porosity conductive fabric leads to a wearable antenna more resilient against harsh physical deformation. However, it suffers from a lower total efficiency due to the low effective conductivity. The characterisation process also provides the material electrical properties required for

accurate antenna modelling in simulators, which include the effective conductivity of the conductive fabric after penetration of the PDMS.

Several new flexible wearable antennas were designed and fabricated using this approach as concept demonstrations. Among them are a dual-band dual-mode antenna, an UWB antenna, and a frequency-reconfigurable patch antenna together with its miniaturised version. All designs are equipped with a full ground plane, which makes them highly desirable for wearable applications for two main reasons. Firstly, the use of a full ground plane makes the antenna highly isolated from the high-permittivity and lossy biological tissue, which allows for a robust performance even in close proximity to the body. Secondly, those antenna designs are associated with low radiation in their lower hemisphere, which in turn decreases the SAR inside the human body.

The dual-band dual-mode characteristic of the first design was achieved by utilising the inherently generated  $TM_{11}$  and  $TM_{02}$  modes of a single circular patch, of which the resonances were tuned to the target 2.4 and 5.8 GHz frequencies using a shorting pin and arc-shaped slots. The main advantage is that only a single radiator and feed are used to achieve the dual-band dual-mode characteristic. On the other hand, previously reported designs generally combine two radiators, fed by single-/two-port systems, with each radiator operating at a different frequency with different radiation mode, and hence are more complex. Moreover, the previous antennas had a lack of the structural flexibility required for wearable applications due to their realisation upon the rigid PCB technology. The antenna proposed in this thesis produces a patch-like radiation (off-body mode) at 2.45 GHz, whereas at 5.8 GHz it produces a monopole-like radiation (on-body mode). In close proximity to the phantom, the measured bandwidths at both modes are 87 and 339 MHz, respectively, with corresponding peak gains of 3.14 and 4.41 dBi, which all are close to those in free space.

In the second design, an innovative patch topology has been successfully developed to

achieve the UWB feature in an inherently narrowband microstrip antenna technology. The design combines multiple resonators and slot-loading techniques to achieve the ultra-wide bandwidth while maintaining a full ground plane on the opposite side of the radiator. This has set the design apart from previously reported flexible planar UWB antennas, which commonly have a partial/modified ground plane or coplanar waveguide topologies for bandwidth enhancement purposes and hence are not suitable for wearable applications. When measured upon the phantom, a bandwidth from 3.68 to 10.1 GHz was achieved with a VSWR of less than 2.2, an average peak gain of 4.53 dBi, and an average total efficiency of 27%, which are quite close to the performance in free space. The antenna also demonstrates the capability for a pulse-based transmission, evaluated through a system fidelity analysis in both free-space and on-body environments.

The highlight of the frequency-reconfigurable antennas (RFPA 1 and its miniaturised version, RFPA 2) developed in this thesis is the robust integration of the lumped tuning elements on top of the flexible materials, thanks to the complete encapsulation of PDMS. RFPA 1 and 2 demonstrated a capability to retain their reconfigurability even in harsh operating environments. To the best of the author's knowledge, no other flexible electronically tunable antenna designs with this feature that have ever been reported. The miniaturisation process of a PDMS-embedded conductive-fabric-based antenna through the inclusion of a PDMS-ceramic composite substrate has also been successfully demonstrated. With only 20% volume of ceramic powder ( $\text{SrTiO}_3$ ) loaded into PDMS, this process results in RFPA 2 having 52% smaller dimensions than its counterpart RFPA 1. More miniaturisation could be achieved through addition of more ceramic powder, but at the expense of having more dielectric losses and lower fringing fields due to the high permittivity. Moreover, a larger amount of ceramic loading affects the flexibility of the PDMS and complicates its fabrication. From the measurements on the phantom, continuous frequency tuning from 2.3 to 2.65 GHz with an average peak gain of 2.6 dBi was

achieved by RFPA 1. On the other hand, a continuous frequency tuning from 2.37 to 2.66 GHz with an average peak gain of -0.7 dBi was achieved by RFPA 2.

The RF performance of each design was also studied by exposing the antennas to various harsh environmental tests, such as repetitive severe bending, bending around the fabricated human phantoms, and machine washing. The tests demonstrated that all the antenna parts including the electronic tuning components remained intact and in working order, thus maintaining the overall antenna performance including good reconfigurability. All these results verify the applicability of the proposed PDMS-embedded conductive fabric for realisation of robust flexible antennas or other RF electronic components for wearable applications.

## 6.2 Future Work

This thesis work opens up number of possibilities for further exploration which may include the following.

### 6.2.1 Flexible Metasurface-Enabled Wideband Circularly Polarised Antenna

The human body is a dynamic operating environment. When worn, the orientation of a wearable antenna is subject to change, which results in not only a resonance frequency shift but also a polarisation mismatch loss if linear polarisation is used in the system. Considering this, an antenna with a circular polarisation in a wide operating band will be advantageous due to its independence of orientation. Some techniques such as providing 90° out-of-phase feedings at orthogonal edges or perturbing the patch at appropriate locations with respect to the feed [103] are well known to successfully generate circular polarisation in a patch-type antenna. However, those methods are only able to produce

circular polarisation at a very limited bandwidth and such a feeding system will increase the complexity of the design, which is not desirable in wearable applications.

It is therefore proposed as a future work to apply the technique of using a metasurface initially proposed in [104] and implement the design fully using PDMS-embedded conductive fabric (see Fig. 6.1). The role of the metasurface is to transform the linearly polarised E-field produced by the main patch radiator into a circularly polarised E-field. With this technique, wideband circular polarisation can be achieved without having to increase the complexity of the feeding system. Moreover, a full ground plane can still be maintained for the required antenna-body isolation. The future work may involve studying the sensitivity of the antenna's 3-dB axial ratio bandwidth to fabrication errors and physical deformation such as bending.

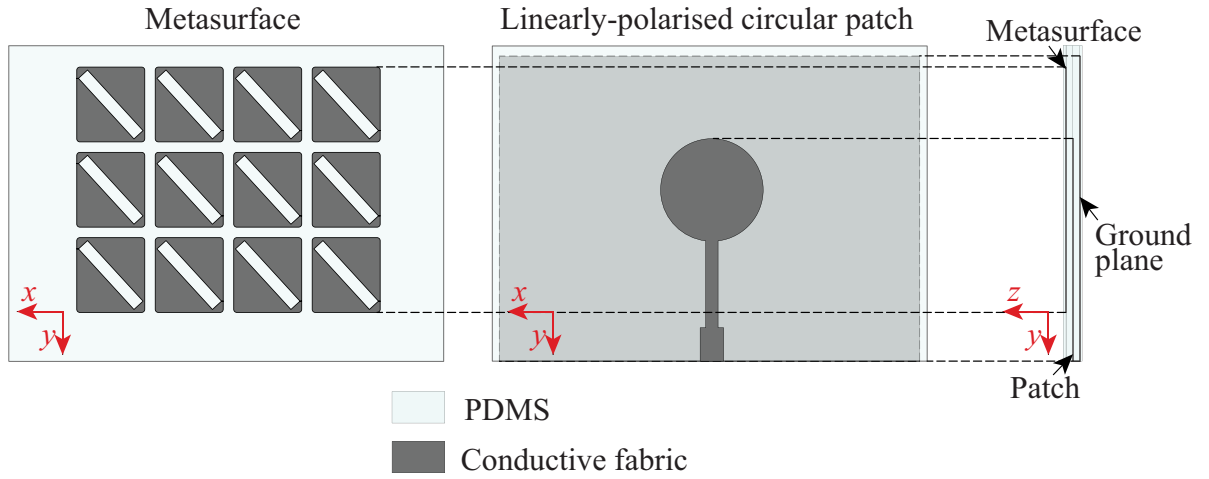


**Figure 6.1:** Illustration of metasurface-enabled wideband circularly polarised antenna on PDMS-embedded conductive fabric

### 6.2.2 Flexible Semi-Transparent Antennas for Unobtrusive Wearable Applications

In recent times, there has also been a considerable advancement in ways of enhancing the aesthetics of wireless wearable devices. One of them is by disguising the electronic components, including antennas, making them unobtrusive. Deploying a thin, transparent or semi-transparent, flexible antenna has been one of the most adapted solutions for this purpose. This type of antenna will also find applications where the surface area is of critical importance. There are two distinct methodologies which have been widely used for realising transparent flexible antennas. The first is by using so-called conductive wire grids which consist of nanoscale to mesoscale metal wires [105, 106] and the second is by using transparent conducting oxide (TCO) electrodes [107]. Both function to create the transparent conductive parts of the antenna, deposited on specific flexible substrates. The major drawback of these methods is, however, their complex and costly fabrication process.

To address this issue, it is proposed to apply the PDMS-embedded conductive-fabric approach to realise a flexible semi-transparent antenna by using semi-transparent conductive fabric. An example of semi-transparent conductive fabric possible to use is shown in Fig. 6.2. This work will include the characterisation of the semi-transparent conductive fabric after embedding in PDMS, followed by development of various semi-transparent wearable antenna designs.

### 6.2.3 Flexible Pattern Reconfigurable Antenna

With potential to avoid noise source, to save energy by directing the signals toward the desired position, and to provide a large coverage by redirecting the main beam [108, 109], pattern-reconfigurable antennas are of interest in the area of wearable wireless communi-



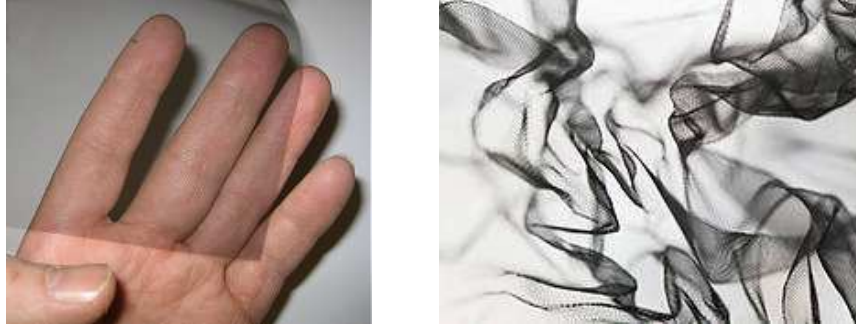


**Figure 6.2:** Veilshield from Less EMF Inc.: woven-mesh polyester fibre coated with nickel/zinc blackened copper (thickness = 0.057 mm, sheet resistance =  $0.1 \Omega/\text{sq}$ ).

cations. Therefore, as the next step, the work presented in Chapter 5 can be extended to investigate the possibility of realising flexible electronically tunable antennas with pattern reconfigurability. The focus of this work will be on the development of a new design that is simple enough for wearable applications and to be realised with the proposed PDMS-embedded conductive fabric. Experimental characterisations of the antenna performance under physical deformation is also worth of doing.

#### 6.2.4 Improving the Efficiency of PDMS-Embedded Conductive Fabric based Antennas

It is also promising to investigate a way to decrease the loss of PDMS-embedded conductive fabric and hence enhances the efficiency of fabricated antennas. A direct consequence of doing this is a broader range of application of PDMS-embedded conductive fabric. One of them would be a possibility to apply the proposed method for realisation of antennas operating in higher frequencies such as 5G band and beyond, where high efficiency is such a crucial need.

One possible solution is by improving the effective conductivity of the conductive fabric. This could be done through repetitive coating of the fabric with suitable conductive

materials as shown in [25]. Another possibility would be through reducing the dielectric loss of PDMS by mixing it with micro/nanoparticle powders such as alumina or polytetrafluoroethylene (PTFE) as demonstrated in [110,111]. It would also be interesting to investigate whether these methods affect the mechanical properties of both materials and thus the mechanical robustness of the PDMS-embedded conductive fabric.

### 6.2.5 Feeding Connection for Testing of PDMS-Embedded Conductive-Fabric Wearable Antennas

As shown in previous chapters, for measurement purposes, all antennas developed in this thesis were fed by coaxial cable interfaced through an SMA connector. By means of silver epoxy, the conductive pin of the SMA connector was connected to the microstrip feeding line, whereas the outer conductor of the connector was connected to the ground plane of the antenna. This technique unfortunately has shown some drawbacks. Firstly, unlike the antenna, the SMA connector is obviously not flexible. This implies that its connection to the antenna may potentially break under mechanical deformations. Secondly, to connect the SMA to the feeding point, the PDMS encapsulation layers have to be cut slightly,

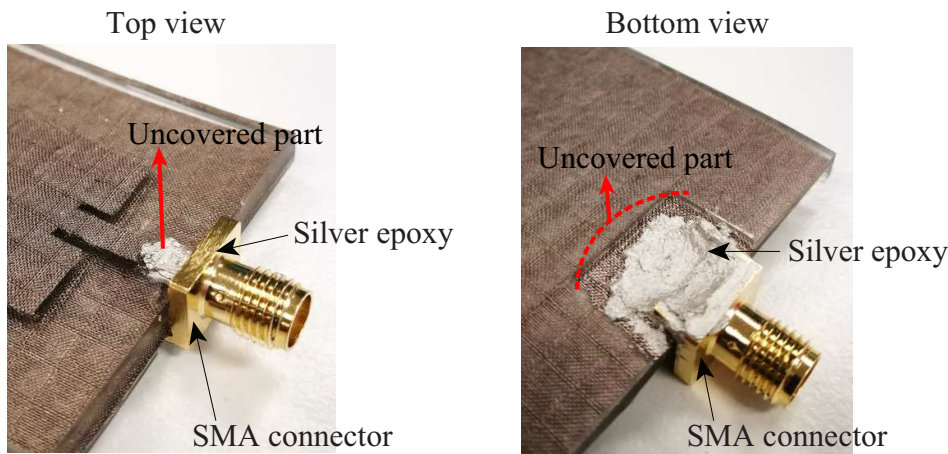


**Figure 6.3:** Feeding point on PDMS-embedded conductive-fabric patch antenna.

for instance at the edges of the transmission line and ground plane of the antenna (see Fig. 6.3). Consequently, those parts are no longer protected from exposure to harsh environmental conditions.

In this thesis, some actions have been taken to prevent or mitigate the disadvantages of this feeding approach, for instance by maintaining the feeding point straight while bending the antennas or by covering the feeding points with plastic tape during the washing test. However, for a more realistic measurement setup, it is promising to explore in the future novel techniques to exclude the use of rigid connector and to effectively connect PDMS-embedded conductive-fabric based wearable antennas to the feeding system. In the past, some solutions to the flexible antenna interconnection issue have been proposed, which have the potential to be applied to the PDMS-embedded conductive-fabric based antennas. Among them, there are the utilisation of commercial metallic snap-on buttons [112, 113], combination of conductive hook and loop fastener [114], the concept of complementary overlap (CO) connection [115], and the most recent one, the use of broadside-couple microstrip line technique [116].



---

# Bibliography

- [1] S. Movassaghi, M. Abolhasan, J. Lipman, D. Smith, and A. Jamalipour, “Wireless body area networks: a survey,” *IEEE Commun. Surveys Tut.*, vol. 16, no. 3, pp. 1658–1686, 2014.
- [2] R. Negra, I. Jemili, and A. Belghith, “Wireless body area networks: applications and technologies,” *Procedia Computer Science*, vol. 83, pp. 1274–1281, 2016.
- [3] D. B. Arbia, M. M. Alam, R. Attia, and E. B. Hamida, “Behavior of wireless body-to-body networks routing strategies for public protection and disaster relief,” in *Proc. 11<sup>th</sup> Int. Conf. on Wirel. and Mobile Comput., Networking and Comm. (WiMob)*, Oct 2015, pp. 117–124.
- [4] G. A. Conway and W. G. Scanlon, “Antennas for over-body-surface communication at 2.45 GHz,” *IEEE Trans. Antennas Propag.*, vol. 57, no. 4, pp. 844–855, April 2009.
- [5] R. Salvado, C. Loss, R. Gonçalves, and P. Pinho, “Textile materials for the design of wearable antennas: a survey,” *Sensors*, vol. 12, no. 11, pp. 15 841–15 857, 2012.

- 
- [6] Y. Ouyang and W. J. Chappell, "High frequency properties of electro-textiles for wearable antenna applications," *IEEE Trans. Antennas Propag.*, vol. 56, no. 2, pp. 381–389, Feb 2008.
  - [7] M. L. Scarpello, I. Kazani, C. Hertleer, H. Rogier, and D. V. Ginste, "Stability and efficiency of screen-printed wearable and washable antennas," *IEEE Antennas Wireless Propag. Lett.*, vol. 11, pp. 838–841, 2012.
  - [8] S. Kang and C. W. Jung, "Wearable fabric antenna on upper arm for MedRadio band applications with reconfigurable beam capability," *Electronics Letters*, vol. 51, no. 17, pp. 1314–1316, 2015.
  - [9] J. Tak, S. Lee, and J. Choi, "All-textile higher order mode circular patch antenna for on-body to on-body communications," *IET Microw., Ant. and Propag.*, vol. 9, no. 6, pp. 576–584, 2015.
  - [10] C. Loss, R. Gonçalves, C. Lopes, P. Pinho, and R. Salvado, "Smart coat with a fully-embedded textile antenna for iot applications," *Sensors*, vol. 16, no. 6, p. 938, 2016.
  - [11] S. Zhu and R. Langley, "Dual-band wearable textile antenna on an EBG substrate," *IEEE Trans. Antennas Propag.*, vol. 57, no. 4, pp. 926–935, April 2009.
  - [12] P. J. Soh, G. A. E. Vandenbosch, S. L. Ooi, and N. H. M. Rais, "Design of a broadband all-textile slotted PIFA," *IEEE Trans. Antennas Propag.*, vol. 60, no. 1, pp. 379–384, Jan 2012.
  - [13] K. Koski, A. Vena, L. Sydanheimo, L. Ukkonen, and Y. Rahmat-Samii, "Design and implementation of electro-textile ground planes for wearable UHF RFID patch tag antennas," *IEEE Antennas Wireless Propag. Lett.*, vol. 12, pp. 964–967, 2013.

- 
- [14] T. Kaufmann and C. Fumeaux, "Wearable textile half-mode substrate-integrated cavity antenna using embroidered vias," *IEEE Antennas Wireless Propag. Lett.*, vol. 12, pp. 805–808, 2013.
- [15] K. W. Lui, O. H. Murphy, and C. Toumazou, "A wearable wideband circularly polarized textile antenna for effective power transmission on a wirelessly-powered sensor platform," *IEEE Trans. Antennas Propag.*, vol. 61, no. 7, pp. 3873–3876, July 2013.
- [16] E. Moradi, T. Bjorninen, L. Ukkonen, and Y. Rahmat-Samii, "Effects of sewing pattern on the performance of embroidered dipole-type RFID tag antennas," *IEEE Antennas Wireless Propag. Lett.*, vol. 11, pp. 1482–1485, 2012.
- [17] Z. Wang, L. Z. Lee, D. Psychoudakis, and J. L. Volakis, "Embroidered multiband body-worn antenna for GSM/PCS/WLAN communications," *IEEE Trans. Antennas Propag.*, vol. 62, no. 6, pp. 3321–3329, June 2014.
- [18] A. Kiourti and J. L. Volakis, "High-geometrical-accuracy embroidery process for textile antennas with fine details," *IEEE Antennas Wireless Propag. Lett.*, vol. 14, pp. 1474–1477, 2015.
- [19] A. Kiourti, C. Lee, and J. L. Volakis, "Fabrication of textile antennas and circuits with 0.1 mm precision," *IEEE Antennas Wireless Propag. Lett.*, vol. 15, pp. 151–153, 2016.
- [20] T. C. Baum, R. W. Ziolkowski, K. Ghorbani, and K. J. Nicholson, "Embroidered active microwave composite preimpregnated electronics-pregtronics," *IEEE Trans. Microw. Theory Tech.*, vol. 64, no. 10, pp. 3175–3186, Oct 2016.

- [21] J. Trajkovikj, J. F. Zürcher, and A. K. Skrivervik, “PDMS, a robust casing for flexible W-BAN antennas,” *IEEE Antennas Propag. Mag.*, vol. 55, no. 5, pp. 287–297, Oct 2013.
- [22] A. S. M. Alqadami, M. F. Jamlos, P. J. Soh, and G. A. E. Vandenbosch, “Assessment of PDMS technology in a MIMO antenna array,” *IEEE Antennas Wireless Propag. Lett.*, vol. 15, pp. 1939–1942, 2016.
- [23] S. Pacchini, M. Cometto, J. J. Chok, G. Dufour, N. Tiercelin, P. Pernod, T. B. Kang, and P. Coquet, “Inkjet-printing of hybrid Ag/conductive polymer towards stretchable microwave devices,” in *Proc. European Microwave Conference (EuMC)*, Sept 2015, pp. 865–868.
- [24] K. Shin, J. S. Lee, J. Hong, and J. Jang, “One-step fabrication of a highly conductive and durable copper paste and its flexible dipole tag-antenna application,” *Chem. Commun.*, vol. 50, no. 3093, 2014.
- [25] Y. Bayram, Y. Zhou, B. S. Shim, S. Xu, J. Zhu, N. A. Kotov, and J. L. Volakis, “E-textile conductors and polymer composites for conformal lightweight antennas,” *IEEE Trans. Antennas Propag.*, vol. 58, no. 8, pp. 2732–2736, Aug 2010.
- [26] R. B. V. B. Simorangkir, Y. Yang, L. Matekovits, and K. P. Esselle, “Dual-band dual-mode textile antenna on PDMS substrate for body-centric communications,” *IEEE Antennas Wireless Propag. Lett.*, vol. 16, pp. 677–680, 2017.
- [27] H. A. E. Elobaid, S. K. A. Rahim, M. Himdi, X. Castel, and M. A. Kasgari, “A transparent and flexible polymer-fabric tissue UWB antenna for future wireless networks,” *IEEE Antennas Wireless Propag. Lett.*, vol. 16, pp. 1333–1336, 2017.



- 
- [28] Z. Wang, L. Zhang, Y. Bayram, and J. L. Volakis, "Multilayer printing of embroidered RF circuits on polymer composites," in *Proc. IEEE Int. Symp. on Ant. and Propag. (APSURSI)*, July 2011, pp. 278–281.
- [29] —, "Embroidered conductive fibers on polymer composite for conformal antennas," *IEEE Trans. Antennas Propag.*, vol. 60, no. 9, pp. 4141–4147, Sept 2012.
- [30] S. Cheng, Z. Wu, P. Hallbjorner, K. Hjort, and A. Rydberg, "Foldable and stretchable liquid metal planar inverted cone antenna," *IEEE Trans. Antennas Propag.*, vol. 57, no. 12, pp. 3765–3771, Dec 2009.
- [31] S. J. Mazlouman, X. J. Jiang, A. Mahanfar, C. Menon, and R. G. Vaughan, "A reconfigurable patch antenna using liquid metal embedded in a silicone substrate," *IEEE Trans. Antennas Propag.*, vol. 59, no. 12, pp. 4406–4412, Dec 2011.
- [32] G. J. Hayes, J. H. So, A. Qusba, M. D. Dickey, and G. Lazzi, "Flexible liquid metal alloy (EGaIn) microstrip patch antenna," *IEEE Trans. Antennas Propag.*, vol. 60, no. 5, pp. 2151–2156, May 2012.
- [33] A. Vorobyov, C. Henemann, and P. Dallemagne, "Liquid metal based antenna for wearable electronic," in *Proc. 10<sup>th</sup> Eur. Conf. on Ant. and Propag. (EuCAP)*, April 2016, pp. 1–3.
- [34] Y. Zhou, Y. Bayram, F. Du, L. Dai, and J. L. Volakis, "Polymer-carbon nanotube sheets for conformal load bearing antennas," *IEEE Trans. Antennas Propag.*, vol. 58, no. 7, pp. 2169–2175, July 2010.
- [35] X. Li, M. M. Honari, Y. Fu, A. Kumar, H. Saghlatoon, P. Mousavi, and H. Chung, "Self-reinforcing graphene coatings on 3D printed elastomers for flexible radio frequency antennas and strain sensors," *Flex. Print. Electron*, vol. 2, no. 035001, 2017.

- [36] Y. Tao, Y. Tao, L. Wang, B. Wang, Z. Yang, and Y. Tai, “High-reproducibility, flexible conductive patterns fabricated with silver nanowire by drop or fit-to-flow method,” *Nanoscale Res. Lett.*, vol. 8, no. 1, p. 147, 2013.
- [37] L. Song, A. C. Myers, J. J. Adams, and Y. Zhu, “Stretchable and reversibly deformable radio frequency antennas based on silver nanowires,” *ACS Appl. Mater. Interfaces*, vol. 6, no. 6, pp. 4248–4253, 2014.
- [38] G.-W. Huang, H.-M. Xiao, and S.-Y. Fu, “Wearable electronics of silver-nanowire/poly(dimethylsiloxane) nanocomposite for smart clothing,” *Scientific Reports*, vol. 5, no. 2, p. 13971, 2015.
- [39] D. C. Thompson, O. Tantot, H. Jallageas, G. E. Ponchak, M. M. Tentzeris, and J. Papapolymerou, “Characterization of liquid crystal polymer (LCP) material and transmission lines on LCP substrates from 30 to 110 GHz,” *IEEE Trans. Microw. Theory Techn.*, vol. 52, no. 4, pp. 1343–1352, April 2004.
- [40] A. C. Durgun, C. A. Balanis, C. R. Birtcher, and D. R. Allee, “Design, simulation, fabrication and testing of flexible bow-tie antennas,” *IEEE Trans. Antennas Propag.*, vol. 59, no. 12, pp. 4425–4435, Dec 2011.
- [41] S. Ahmed, F. A. Tahir, A. Shamim, and H. M. Cheema, “A compact kapton-based inkjet-printed multiband antenna for flexible wireless devices,” *IEEE Antennas Wireless Propag. Lett.*, vol. 14, pp. 1802–1805, 2015.
- [42] S. M. Saeed, C. A. Balanis, and C. R. Birtcher, “Inkjet-printed flexible reconfigurable antenna for conformal WLAN/WiMAX wireless devices,” *IEEE Antennas Wireless Propag. Lett.*, vol. 15, pp. 1979–1982, 2016.

- [43] P. Bodo and J.-E. Sundgren, "Titanium deposition onto ion-bombarded and plasma-treated polydimethylsiloxane: Surface modification, interface and adhesion," *Thin Solid Films*, vol. 136, no. 1, pp. 147–159, 1986.
- [44] A. Kamyshny and S. Magdassi, "Conductive nanomaterials for printed electronics," *Small*, vol. 10, no. 17, pp. 3515–3535, 2014.
- [45] X. Huang, T. Leng, M. Zhu, X. Zhang, J. Chen, K. Chang, M. Aqeeli, A. K. Geim, K. S. Novoselov, and Z. Hu, "Highly flexible and conductive printed graphene for wireless wearable communications applications," *Scientific Reports*, vol. 5, no. 1, p. 18298, 2016.
- [46] A. Kiourti and J. L. Volakis, "Stretchable and flexible e-fiber wire antennas embedded in polymer," *IEEE Antennas Wireless Propag. Lett.*, vol. 13, pp. 1381–1384, 2014.
- [47] S. Shao, A. Kiourti, R. J. Burkholder, and J. L. Volakis, "Broadband textile-based passive UHF RFID tag antenna for elastic material," *IEEE Antennas Wireless Propag. Lett.*, vol. 14, pp. 1385–1388, 2015.
- [48] I. D. Johnston, D. K. McCluskey, C. K. L. Tan, and M. C. Tracey, "Mechanical characterization of bulk Sylgard 184 for microfluidics and microengineering," *J. Micromechanics and Microengineering*, vol. 24, no. 3, p. 035017, 2014.
- [49] S. Koulouridis, G. Kiziltas, Y. Zhou, D. J. Hansford, and J. L. Volakis, "Polymer-ceramic composites for microwave applications: Fabrication and performance assessment," *IEEE Trans. Microw. Theory Tech.*, vol. 54, no. 12, pp. 4202–4208, Dec 2006.
- [50] A. R. Colas, "Silicones: preparation, properties and performances," *Chimie Nouvelle, The Journal of the "Societe Royale de Chimie"*, pp. 847–852, 1990.

- [51] M. Sebastian and L. Namitha, "Rubber–ceramic composites," in *Microwave Materials and Applications 2V Set*. John Wiley & Sons, Ltd, 2017, pp. 537–574.
- [52] B. Ivsic, D. Bonefacic, and J. Bartolic, "Considerations on embroidered textile antennas for wearable applications," *IEEE Antennas Wireless Propag. Lett.*, vol. 12, pp. 1708–1711, 2013.
- [53] P. L. Wise, I. M. Reaney, W. E. Lee, T. J. Price, D. M. Iddles, and D. S. Cannell, "Structure-microwave property relations of Ca and Sr titanates," *J. of the European Ceramic Soc.*, vol. 21, no. 15, pp. 2629–2632, 2001.
- [54] S. Rajesh, K. P. Murali, K. V. Rajani, and R. Ratheesh, "SrTiO<sub>3</sub>-filled PTFE composite laminates for microwave substrate applications," *Int. Journal of Appl. Ceramic Tech.*, vol. 6, no. 5, pp. 553–561, 2009.
- [55] W.-Y. Zhou, S.-H. Qi, H.-Z. Zhao, and N.-L. Liu, "Thermally conductive silicone rubber reinforced with boron nitride particle," *Polymer Composites*, vol. 28, no. 1, pp. 23–28, 2007.
- [56] M. A. Eddings, M. A. Johnson, and B. K. Gale, "Determining the optimal PDMS–PDMS bonding technique for microfluidic devices," *J. Micromechanics and Micro-engineering*, vol. 18, no. 6, p. 067001, 2008.
- [57] Z. Xu, T. Kaufmann, and C. Fumeaux, "Wearable textile shielded stripline for broadband operation," *IEEE Microw. Compon. Lett.*, vol. 24, no. 8, pp. 566–568, 2014.
- [58] K. P. Latti, M. Kettunen, J. P. Strom, and P. Silventoinen, "A review of microstrip T-resonator method in determining the dielectric properties of printed circuit board materials," *IEEE Trans. Instrum. Meas.*, vol. 56, no. 5, pp. 1845–1850, Oct 2007.

- [59] A. Skrivervik, J.-F. Zurcher, O. Staub, and J. Mosig, "PCS antenna design: the challenge of miniaturization," *IEEE Antennas Propag. Mag.*, vol. 43, no. 4, pp. 12–27, 2001.
- [60] Z. G. Liu and Y. X. Guo, "Dual band low profile antenna for body centric communications," *IEEE Trans. Antennas Propag.*, vol. 61, no. 4, pp. 2282–2285, April 2013.
- [61] —, "Compact low-profile dual band metamaterial antenna for body centric communications," *IEEE Antennas Wireless Propag. Lett.*, vol. 14, pp. 863–866, Dec 2015.
- [62] Y. Hong, J. Tak, and J. Choi, "Dual-band dual-mode patch antenna for on-on-off wban applications," *Electronics Letters*, vol. 50, no. 25, pp. 1895–1896, 2014.
- [63] J. Tak, S. Woo, J. Kwon, and J. Choi, "Dual-band dual-mode patch antenna for on-/off-body WBAN communications," *IEEE Antennas Wireless Propag. Lett.*, vol. 15, pp. 348–351, 2016.
- [64] R. Garg, R. Bhartia, I. Bahl, and A. Ittipiboon, "Circular disk and ring antennas," in *Microstrip Antenna Design Handbook*. Boston: Artech House, Inc., 2001, ch. 5, pp. 346–347.
- [65] B. Wang and Y. Lo, "Microstrip antennas for dual-frequency operation," *IEEE Trans. Antennas Propag.*, vol. 32, no. 9, pp. 938–943, Sep 1984.
- [66] K. Ito, K. Furuya, Y. Okano, and L. Hamada, "Development and characteristics of a biological tissue-equivalent phantom for microwaves," *Electron. Commun. Japan Part I Commun.*, vol. 84, no. 4, pp. 67–77, 2001.

- [67] D. Andreuccetti, R. Fossi, and C. Petrucci, "An internet resource for the calculation of the dielectric properties of body tissues in the frequency range 10 Hz–100 GHz," IFAC-CNR, Florence, Italy, 1997. [Online]. Available: <http://niremf.ifac.cnr.it/tissprop/>
- [68] T. Kellomäki, "Analysis of circular polarization of cylindrically bent microstrip antennas," *Int. Journal of Ant. and Propag.*, vol. 2012, pp. 1–8, 2012.
- [69] H. B. Lim, D. Baumann, J. Cai, R. Koh, E. P. Li, and Y. Lu, "Antennae polarization for effective transmission of UWB signal around human body," in *Proc. IEEE Int. Conf. on Ultra-Wideband*, Sept. 2007, pp. 220–224.
- [70] "IEEE Standard for Safety Levels with Respect to Human Exposure to Radio Frequency Electromagnetic Fields, 3 kHz to 300 GHz," *IEEE Std C95.1-2005 (Revision of IEEE Std C95.1-1991)*, pp. 1–238, April 2006.
- [71] J. Foerster, E. Green, S. Somayazulu, D. Leeper, I. A. Labs, I. A. Labs, I. Corp, and I. Corp, "Ultra-wideband technology for short-or medium-range wireless communications," *Intel Tech. Journal*, vol. 2, pp. 1–11, 2011.
- [72] M. Klemm and G. Troester, "Textile UWB antennas for wireless body area networks," *IEEE Trans. Antennas Propag.*, vol. 54, no. 11, pp. 3192–3197, Nov 2006.
- [73] G. Shaker, S. Safavi-Naeini, N. Sangary, and M. M. Tentzeris, "Inkjet printing of ultrawideband (UWB) antennas on paper-based substrates," *IEEE Antennas Wireless Propag. Lett.*, vol. 10, pp. 111–114, 2011.
- [74] H. R. Khaleel, H. M. Al-Rizzo, D. G. Rucker, and S. Mohan, "A compact polyimide-based UWB antenna for flexible electronics," *IEEE Antennas Wireless Propag. Lett.*, vol. 11, pp. 564–567, 2012.

- [75] Q. H. Abbasi, M. U. Rehman, X. Yang, A. Alomainy, K. Qaraqe, and E. Serpedin, "Ultrawideband band-notched flexible antenna for wearable applications," *IEEE Antennas Wireless Propag. Lett.*, vol. 12, pp. 1606–1609, 2013.
- [76] T. I. Yuk, Y. Sun, and S. W. Cheung, "Design of a textile ultra-wideband antenna with stable performance for body-centric wireless communications," *IET Microw., Ant. and Propag.*, vol. 8, no. 15, pp. 1363–1375, dec 2014.
- [77] Y. Qiu, Y. H. Jung, S. Lee, T. Y. Shih, J. Lee, Y. H. Xu, R. Xu, W. Lin, N. Behdad, and Z. Ma, "Compact parylene-c-coated flexible antenna for WLAN and upper-band UWB applications," *Electronics Letters*, vol. 50, no. 24, pp. 1782–1784, 2014.
- [78] R. Yahya, M. R. Kamarudin, and N. Seman, "Effect of rainwater and seawater on the permittivity of denim jean substrate and performance of UWB eye-shaped antenna," *IEEE Antennas Wireless Propag. Lett.*, vol. 13, pp. 806–809, 2014.
- [79] P. B. Samal, P. J. Soh, and G. A. E. Vandenbosch, "UWB all-textile antenna with full ground plane for off-body WBAN communications," *IEEE Trans. Antennas Propag.*, vol. 62, no. 1, pp. 102–108, Jan 2014.
- [80] L. A. Y. Poffelie, P. J. Soh, S. Yan, and G. A. E. Vandenbosch, "A high-fidelity all-textile UWB antenna with low back radiation for off-body WBAN applications," *IEEE Trans. Antennas Propag.*, vol. 64, no. 2, pp. 757–760, Feb 2016.
- [81] A. da Conceicao Andrade, I. P. Fonseca, S. F. Jilani, and A. Alomainy, "Reconfigurable textile-based ultra-wideband antenna for wearable applications," in *Proc. 10<sup>th</sup> Eur. Conf. on Ant. and Propag. (EuCAP)*, April 2016, pp. 1–4.
- [82] A. Kiourti, J. L. Volakis, R. B. V. B. Simorangkir, S. M. Abbas, and K. P. Esselle, "UWB antennas on conductive textiles," in *Proc. IEEE Int. Symp. on Ant. and Propag. (APSURSI)*, June 2016, pp. 1941–1942.

- 
- [83] K. L. Wong, "Broadband microstrip antennas," in *Compact and Broadband Microstrip Antenna*. New York: John Wiley & Sons, Inc., 2002, ch. 7, pp. 232–278.
- [84] N. Chahat, M. Zhadobov, R. Sauleau, and K. Ito, "A compact UWB antenna for on-body applications," *IEEE Trans. Antennas Propag.*, vol. 59, no. 4, pp. 1123–1131, April 2011.
- [85] M. Sharma, A. Alomainy, and C. Parini, "Fidelity pattern analysis of a CPW-fed miniature UWB antenna using different excitation pulses," *IEEE Antennas Wireless Propag. Lett.*, vol. 14, pp. 494–498, 2015.
- [86] G. Quintero, J. F. Zurcher, and A. K. Skrivervik, "System fidelity factor: a new method for comparing UWB antennas," *IEEE Trans. Antennas Propag.*, vol. 59, no. 7, pp. 2502–2512, July 2011.
- [87] M. Koohestani, N. Pires, A. K. Skrivervik, and A. A. Moreira, "Performance study of a UWB antenna in proximity to a human arm," *IEEE Antennas Wireless Propag. Lett.*, vol. 12, pp. 555–558, 2013.
- [88] A. R. Weily, T. S. Bird, and Y. J. Guo, "A reconfigurable high-gain partially reflecting surface antenna," *IEEE Trans. Antennas Propag.*, vol. 56, no. 11, pp. 3382–3390, Nov 2008.
- [89] L. Ge and K. M. Luk, "Frequency-reconfigurable low-profile circular monopolar patch antenna," *IEEE Trans. Antennas Propag.*, vol. 62, no. 7, pp. 3443–3449, July 2014.
- [90] S. L. S. Yang and K. M. Luk, "Design of a wide-band L-probe patch antenna for pattern reconfiguration or diversity applications," *IEEE Trans. Antennas Propag.*, vol. 54, no. 2, pp. 433–438, Feb 2006.



- [91] P. Y. Qin, A. R. Weily, Y. J. Guo, and C. H. Liang, "Polarization reconfigurable U-slot patch antenna," *IEEE Trans. Antennas Propag.*, vol. 58, no. 10, pp. 3383–3388, Oct 2010.
- [92] N. Nguyen-Trong, T. Kaufmann, L. Hall, and C. Fumeaux, "Analysis and design of a reconfigurable antenna based on half-mode substrate-integrated cavity," *IEEE Trans. Antennas Propag.*, vol. 63, no. 8, pp. 3345–3353, Aug 2015.
- [93] K. Esselle and B. Majumdar, "Fixed frequency broadside–endfire beam steerable antennas," *Electronics Letters*, vol. 52, no. 15, pp. 1282–1284, 2016.
- [94] Y. Yang, R. B. V. B. Simorangkir, X. Zhu, K. Esselle, and Q. Xue, "A novel boresight and conical pattern reconfigurable antenna with the diversity of 360-degree polarization scanning," *IEEE Trans. Antennas Propag.*, vol. 65, no. 11, pp. 5747–5756, Nov 2017.
- [95] M. I. Jais, M. F. Jamlos, M. Jusoh, T. Sabapathy, M. R. Kamarudin, R. B. Ahmad, A. A. A. H. Azremi, E. I. Azmi, P. J. Soh, G. A. E. Vandenbosch, and N. L. K. Ishak, "A novel 2.45 GHz switchable beam textile antenna (SBTA) for outdoor wireless body area network (WBAN) applications," *Prog. In Electromagnetics Research*, vol. 138, pp. 613–627, 2013.
- [96] F. A. Tahir and A. Javed, "A compact dual-band frequency-reconfigurable textile antenna for wearable applications," *Micro and Opt. Tech. Letters*, vol. 57, no. 10, pp. 2251–2257, oct 2015.
- [97] S. Kang and C. W. Jung, "Wearable fabric reconfigurable beam-steering antenna for on/off-body communication system," *Int. Journal of Ant. and Propag.*, vol. 2015, no. 539843, 2015.

- [98] S. Yan and G. A. E. Vandenbosch, "Radiation pattern-reconfigurable wearable antenna based on metamaterial structure," *IEEE Antennas Wireless Propag. Lett.*, vol. 15, pp. 1715–1718, 2016.
- [99] R. Garg, R. Bhartia, I. Bahl, and A. Ittipiboon, "Rectangular microstrip antennas," in *Microstrip Antenna Design Handbook*. Boston: Artech House, Inc., 2001, ch. 4, p. 265.
- [100] Aeroflex Microelectronic Solutions, "GaAs hyperabrupt varactor diodes MGVS series," A17041 datasheet, 2005. [Online]. Available: <http://www.aeroflex-metelics.com>
- [101] H. Li, J. Xiong, Y. Yu, and S. He, "A simple compact reconfigurable slot antenna with a very wide tuning range," *IEEE Trans. Antennas Propag.*, vol. 58, no. 11, pp. 3725–3728, Nov 2010.
- [102] Y. Y. Fu, Y. L. Chan, M. H. Yang, Y. C. Chan, J. Virkki, T. Bjorninen, L. Sydanheimo, and L. Ukkonen, "Experimental study on the washing durability of electro-textile UHF RFID tags," *IEEE Antennas Wireless Propag. Lett.*, vol. 14, pp. 466–469, 2015.
- [103] R. Garg, R. Bhartia, I. Bahl, and A. Ittipiboon, "Circularly polarized microstrip antennas and techniques," in *Microstrip Antenna Design Handbook*. Boston: Artech House, Inc., 2001, ch. 8, pp. 494–497.
- [104] H. L. Zhu, S. W. Cheung, X. H. Liu, and T. I. Yuk, "Design of polarization reconfigurable antenna using metasurface," *IEEE Trans. Antennas Propag.*, vol. 62, no. 6, pp. 2891–2898, June 2014.

- [105] W. Hong, S. Lim, S. Ko, and Y. G. Kim, "Optically invisible antenna integrated within an OLED touch display panel for IoT applications," *IEEE Trans. Antennas Propag.*, vol. 65, no. 7, pp. 3750–3755, July 2017.
- [106] Q. L. Li, S. W. Cheung, D. Wu, and T. I. Yuk, "Optically transparent dual-band MIMO antenna using micro-metal mesh conductive film for WLAN system," *IEEE Antennas Wireless Propag. Lett.*, vol. 16, pp. 920–923, 2017.
- [107] S. Hong, S. H. Kang, Y. Kim, and C. W. Jung, "Transparent and flexible antenna for wearable glasses applications," *IEEE Trans. Antennas Propag.*, vol. 64, no. 7, pp. 2797–2804, July 2016.
- [108] S. Zhang, G. H. Huff, J. Feng, and J. T. Bernhard, "A pattern reconfigurable microstrip parasitic array," *IEEE Trans. Antennas Propag.*, vol. 52, no. 10, pp. 2773–2776, Oct 2004.
- [109] S. H. Chen, J. S. Row, and K. L. Wong, "Reconfigurable square-ring patch antenna with pattern diversity," *IEEE Trans. Antennas Propag.*, vol. 55, no. 2, pp. 472–475, Feb 2007.
- [110] D. Headland, P. Thurgood, D. Stavrevski, W. Withayachumnankul, D. Abbott, M. Bhaskaran, and S. Sriram, "Modified elastomeric polymers for loss reduction in the terahertz range," in *Proc. 40<sup>th</sup> Int. Conf. on Infrared, Millimeter, and Terahertz waves (IRMMW-THz)*, Aug 2015, pp. 1–2.
- [111] —, "Doped polymer for low-loss dielectric material in the terahertz range," *Opt. Mater. Express*, vol. 5, no. 6, pp. 1373–1380, Jun 2015.
- [112] T. Kellomäki, "Snaps to connect coaxial and microstrip lines in wearable systems," *Int. Journal of Ant. and Propag.*, pp. 1–10, 2012.

- 
- [113] S. J. Chen, C. Fumeaux, D. C. Ranasinghe, and T. Kaufmann, "Paired snap-on buttons connections for balanced antennas in wearable systems," *IEEE Antennas Wireless Propag. Lett.*, vol. 14, pp. 1498–1501, 2015.
  - [114] R. D. Seager, A. Chauraya, S. Zhang, W. Whittow, and Y. Vardaxoglou, "Flexible radio frequency connectors for textile electronics," *Electronics Letters*, vol. 49, no. 22, pp. 1371–1373, Oct 2013.
  - [115] A. Tsolis, A. A. Alexandridis, W. G. Whittow, and J. C. Vardaxoglou, "Connecting wearable textile transmission lines: all-textile fabrication solutions and design techniques," *Electronics Letters*, vol. 51, no. 15, pp. 1136–1138, 2015.
  - [116] S. E. Adami, P. Proynov, G. S. Hilton, G. Yang, C. Zhang, D. Zhu, Y. Li, S. P. Beeby, I. J. Craddock, and B. H. Stark, "A flexible 2.45-GHz power harvesting wristband with net system output from -24.3 dBm of RF power," *IEEE Trans. Microw. Theory Techn.*, vol. 66, no. 1, pp. 380–395, Jan 2018.